Contents

Introduction

With non-classical light, one generally means states of radiation that can't be described by classical electromagnetic theory. Into this definition are included Fock states, i.e. states with a well defined number of photons, whose most common examples are represented by single photons or entangled photon pairs. Such kind of states can be considered as suitable objects to implement quantum technologies, including application fields such as quantum computing, quantum imaging, quantum metrology and quantum secure communication [1, 2, 3]. In the last decades, in fact, quantum technologies experienced a strong demand, in particular for quantum information processing (QIP) applications [4]. The motivations can be found in the fact that we are living in the era of *big data*, where a tremendous growth in the amount of data to be processed and transmitted every day requires the development of new strategies, among which quantum technologies seem to constitute a leading approach. It has been theoretically and experimentally shown that quantum mechanical effects, such as superposition and entanglement, can be exploited to significantly increase the computational capability with respect to that of classical machines [5, 6, 2, 7]. From another point of view, qubit-based communication involving cryptographic protocols could allow for total secure transmission of information [8, 9, 10].

The fundamental building block of quantum technologies is the *qubit*, i.e. the quantum analogous of the classical bit, which can assume a value given by any linear combination of two states constituting the basis, instead of only two possible values, as in the classic case [11]. Many objects can be used to realize qubits, like trapped atoms and ions, nuclear spins, quantum dots, superconducting materials. However, there are many reasons for which photons are considered as a very promising road, and in some cases perhaps the best candidate, for the implementation of quantum technologies. Among the multiplicity of advantages associated with photons, one can identify speed, low noise, low losses in optical fibers, and ease of manipulation for the implementation of quantum gates. For instance, if we consider the case of secure communication, photons can be used for the transmission of totally secure qubit-encoded information travelling via a public channel, exploiting the al-

ready existing fiber optics infrastructure, allowing for high-speed secure data transfer all over the world. On the other hand, the development of devices based on hybrid photonic-electronic circuits, enabling the implementation of optical interconnections between internal components of a computing machine, could be indeed a solution to the problem of slow electrical interconnections, which at the moment is considered to be a bottleneck for the increase of computational speed. Most importantly, single photons offer many different degrees of freedom for qubit encoding, such as polarization, phase and path [11].

As demonstrated by the crucial work by Knill et al. in 2001, the implementation of quantum technologies requires the development of three types of components, that are necessary for a complete integrated quantum photonic platform: photon sources, linear optical elements (such as beam splitters, filters and modulators) and detectors [12].

For instance, one would need efficient single-photon sources, that must generate photons on-demand: this can be obtained from deterministic atomic-like sources, or alternatively exploiting probabilistic emission of photon pairs, where an almost deterministic behaviour can be achieved with the practice of heralding, i.e. using one photon of the pair to announce the presence of the other one [13]. The category of deterministic sources mainly includes single atoms or molecules [14], semiconductor-based quantum dots [15, 16, 17, 18, 19], and various kinds of optically-active defects in diamond [20, 21, 22, 23]. The category of heralded sources was historically realized by means of photon pairs emitted by nonlinear crystals, subjected to optical pumping with intense lasers [24]. More recently, integrated sources of heralded single photons have been achieved both in periodically poled waveguides and in semiconductor-based devices [25].

Another kind of non-classical states of light that finds many applications for quantum technologies is that of entangled photon pairs, where the degree of correlation among photons constituting the couple cannot be described by any deterministic theory. Integrated sources of entangled photons have been demonstrated, exploiting the photon pair emission from bi-exciton cascade emission in quantum dots [26, 27] or by parametric processes in nonlinear waveguides [28, 29, 30, 31, 32].

In order to bring quantum technologies from laboratories to real applications, they need to be characterized by compactness, scalability, robustness, and the potential for integration with electronics components. Silicon photonics constitutes a promising way to satisfy all the above mentioned requirements, associated to complementary metal-oxide-semiconductor (CMOS)-compatibility, meaning that photonic devices could be realized exploiting an already well established technology [33, 34]. In this perspective, there is the need to develop integrated photonic devices where photons can be generated, manipulated, processed, and in the end detected, in the philosophy of the so called *lab-on-a-chip*. Fabs are playing a crucial role in the development of silicon photonics integrated devices, since they give access to their users to already

existing infrastructures to realize CMOS compatible devices at a relatively low cost. Some of the experiments that will be reported in this thesis (in chapters 4 and 5) have been realized by OpSIS, a fab arisen from a collaboration between the University of Delaware and Institute of Microelectronics (IME) A-STAR in Singapore [35, 36]. This thesis finds its motivations and applications in this environment, focusing in the branch of integrated photon sources and on linear optical elements that can be used to manipulate light on-chip.

Silicon integrated waveguides can be realized out of silicon-on-insulator (SOI) platform, constituted by a silicon 220-nm thick guiding layer on top of a silica insulating layer, by means of litography and etching techniques that allow to pattern the top silicon guiding layer. In this way, light at telecom wavelengths can be guided in silicon wire waveguides having cross-sections below 1 μm^2, exploiting total internal refraction (TIR) mechanism thanks to the high refractive index contrast between silicon and silica. The SOI platform can be used as a basis to realize many linear and nonlinear optical components, such as beam splitters, filters, modulators. In particular, in this thesis we will explore the capabilities of silicon integrated microrings, which are constituted by a channel waveguide closed back onto itself to form a circular resonator, where light propagates always in the same direction [37]. According to their configuration, microrings can be used as modulators, filters, sensors or even photon sources [38, 39]. In fact, the field enhancement that can be achieved in microring resonators, thanks to high quality factors (typically on the order of some 10^4 [40, 41]) nonlinear parametric processes can be amplified and efficiently exploited to generate photon pairs. Since silicon, being a centrosymmetric material, has a vanishing second order nonlinear optical susceptibility, the third-order nonlinearity can be exploited to generate photon pairs, through the effect of four-wave mixing [42, 43]. While this effect has already been observed in optical fibers [44] and wire waveguides [28, 45], the small footprint (tens of μm^2) and field enhancement achieved in microrings make them an efficient and compact source of photon pairs [46, 47, 41]. Recently, they have been also demonstrated to efficiently generate correlated and time-energy entangled photon pairs [48, 49].

More generally, in the works that will be reported in this thesis we will explore some properties and possible uses of silicon microring resonators exploiting the enhancement of four-wave mixing for low power generation of photon pairs.

The first chapter will be dedicated to the contextualization of te thesis and to an overview of the technological needs that constitute the basis of its motivation. An introduction to quantum information technologies will be given, explaining the reasons for which non-classical states of light, represented by photons, are a suitable tool for their implementation. Different kind of sources of non-classical states of light will be described, focusing on different strategies to generate single photons, or pairs of photons that can be entangled

in different degrees of freedom, starting from more traditional kind of sources to the most recent ones based on integrated devices.

In the second chapter we will enter more in the core of the thesis, approaching the field of silicon photonics. After an introduction to some of the optical components that can be integrated on silicon chip, the attention will be focused on silicon microring resonators, that can be considered as a conducting wire through the all thesis. Their working principle will be described, as well as their figures of merit and main applications, ranging from biosensing and filtering to active modulation of optical signals. In the final section of second chapter it will be explained how effects based on third-order nonlinear susceptibility, and in particular four-wave mixing, can be enhanced in silicon microring resonators, making them a suitable instrument for the generation of non-classical states of light.

Then, in the third chapter we will report on measurements of four-wave mixing on porous silicon integrated microring resonators. Such devices, in fact, have been recently demonstrated to reach high Q factors that could allow to enhance and thus to observe the nonlinear effect at low pump power. The reported experiment is the first case in literature of four-wave mixing enhancement in a porous silicon integrated microresonators.

In chapter 4 we will illustrate two experiments involving silicon chips based on SOI architecture, with the purpose to demonstrate that correlated photon pairs, generated by four-wave mixing in silicon microrings, can be completely filtered on-chip, and that they can be separated and routed to different outputs of the device. To suppress the pump laser, which is much more intense of the generated signals, an extinction of more than 100 dB [41] is needed, in a narrow bandwidth and with low insertion losses. To achieve it, we employed integrated distributed Bragg reflectors and tunable add-drop filters. To this purpose, in a first experiment it will be demonstrated that in principle it is possible to completely reject the pump laser on a single chip. In a second experiment, we will report about time-correlation measurement between photon pairs which are generated on-chip, and that are sent to a second identical chip where they can be completely filtered and routed to different outputs by means of add-drop filters, without the need of any off-chip filtering.

Microrings can be used to generate also non-correlated photons: in fact it has been theoretically predicted [50] that spontaneous FWM in microrings can be used to generate correlated photons whose energy correlation can be controlled by changing the coherence time of the pump. This will be experimentally demonstrated in chapter 5, where we report the development of a method to determine the joint spectral density, to gain information about the quantum state of the generated photon pairs, with unprecedented resolution and much faster measurements than with state-of-the-art techniques.

Chapters 3, 4 and 5 will be structured in the following way: after a more detailed introduction, a description of the samples and their fabrication techniques will be given, followed by the characterization of the samples. Then,

the experiment will be described and the results of the measurements will be reported and discussed.

The works reported in this thesis have been already published by peer reviewed papers of which the author of this thesis is a co-author, thus the references to the considered papers could be sometimes omitted. For this reason, we specify now that the results of joint spectral density measurements on photon pairs generated in silicon microring resonators (chapter 5) have been reported in a paper published by Scientific Reports in 2016 [51]. The four wave-mixing measurement in porous silicon microrings, reported in chapter 3, has been published by Applied Physics Letters in 2016 [52]. Finally, all the results reported in chapter 4 about the on-chip filtering and routing of correlated photons can be found on a paper published by Physical Review X in 2014 [53].

The author took part in the development of the experimental set-ups, the characterization of the samples and all the measurements that are reported in this thesis. The author has been also involved in the fabrication and characterization of porous silicon waveguides, reported in chapter 3, which has been carried out in the laboratories of Electrical Engineering and Computer Science at Vanderbilt University (Nashville, TN, USA).

Chapter 1

Sources of non-classical states of light

This introductory chapter intends to frame this thesis into the dynamic and prolific context of sources of nonclassical states of light, and in particular the ones realized with integrated silicon photonics. To do this, we will give the motivations for our work, starting from the technological need of quantum technologies, in particular for quantum computation and quantum communication. We will define the properties of ideal sources of non-classical state of light, focusing on single photons and entangled photon pairs. In these sections we will also give an overview of the main results that have been achieved up to now, trying to underline the strength and the weakness of different kinds of sources.

Before starting, we specify what we mean by non-classical light, that can be defined as light with nonclassical noise. It includes for instance Fock states with a definite photon number, entangled states, squeezed states. We refer to [11] for an overall more detailed treatment, while here we focus on single photons and photon pairs, explaing why they are so appealing for quantum technologies, in particular in the field of quantum communication and quantum computation.

1.1 Need of photonic quantum technologies

During the last decades, the research of single photons sources has experienced a rapid growth due to the pressing technological demand of quantum information science. In fact, quantum technology is promising to bring improvements in disparate fields, such as quantum metrology, that allows to measure quantities with unprecedented precision, or quantum litography, a tool necessary to realize microscopic devices beyond the diffraction limit. Some interesting applications, that we will analyse more in detail, are quantum cryptography, allowing perfectly secure communication, and quantum computing,

identified as a promising route to reduce the required computational resources to achieve certain tasks, as well as to solve problems that would be impossible for a classical machine. In order to efficiently implement information science, we need the development of scalable, reliable and relatively cheap quantum-based circuits that could be mass-producted. The use of photons as qubits is considered to be a leading approach to implement quantum information, because of their high-speed transmission and compatibility with classical photonic technology, together with other reasons, as will be discussed later. A whole optical quantum circuit would need as basic components: photon sources, photon manipulators, i.e. some objects that are able to perform operations among photons, and single-photon detectors. A complete analysis of all the parts of an integrated quantum circuit goes beyond the purposes of this thesis, so we won't enter into all the details of the components, while we intend to focus more on the integrated sources.

1.1.1 Quantum computation

Until 2001 it was a common belief that in order to process quantum information one needs to face with non-linear interactions among single photons, that happen with very low probabilities. The seminal work by Knill, Laflamme and Milburn (KLM) proposed a model to implement quantum computation with linear optic components[12], needing just single photon sources, linear optical circuits and photon detectors. Their scheme, also known as KLM, allowed to deal with interaction among photons exploiting the intrinsic nonlinearity of the detectors, and triggered several experimental demonstrations of quantum processing, starting from the first basic operations to some more complex ones. (cit)

To explain the importance of quantum information science, we start from its basic features. While in classical information the *bit* is a variable that can assume two distinct logic values, (0 and 1) the quantum bit of information, known as *qubit*, can assume an infinity of values. It typically consists of the state of a two-level quantum system, that can be described by the superposition of two states $|0\rangle$ and $|1\rangle$, as represented by

$$\alpha|0\rangle + \beta|1\rangle. \tag{1.1}$$

The states $|0\rangle$ and $|1\rangle$ are orthogonal and constitute a basis that can be used to build a two-dimensional Hilbert space, also known in this field as *computational basis*. If one measures the quantum system, $|\alpha|^2$ and $|\beta|^2$ are the probabilities of finding it in the state $|0\rangle$ or $|1\rangle$, respectively. The probabilities are normalized, thus relation $|\alpha|^2 + |\beta|^2$ holds, allowing one to rewrite the two-level qubit state in the form:

$$|\psi\rangle = cos\frac{\theta}{2}|0\rangle + e^{i\phi}sin\frac{\theta}{2}|1\rangle \tag{1.2}$$

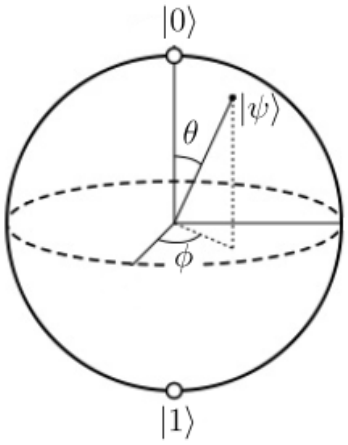

Figure 1.1: Bloch sphere: the two qubits states are the poles of the sphere, the point ψ on its surface represents a pure state as the one defined in eq. (1.2).

where θ and ϕ can assume values $0 < \theta < \pi$ and $0 < \phi < 2\pi$. The state shown in (1.1) or (1.2) is called a *pure* state and can be represented by a single vector in the Hilbert space. However, not all the states are pure and the system can be found in a *mixed state*, that can be described introducing the density matrix

$$\rho = \sum_i P_i |\psi_i\rangle\langle\psi_i|. \tag{1.3}$$

The pure state can be found in the particular case of $P_i = 1$, where $\rho = \rho^2$ and $Tr(\rho^2) = 1$. More generally, for a mixed state the trace will be $Tr(\rho^2) < 1$. To give a more intuitive picture of this system we introduce the Bloch sphere, represented in Fig.1.1. Here the two states constituting the computational basis are the two poles of the sphere. When the involved states are photon states, one usually refers to it as Poincaré sphere. A pure state, as the one shown in equation (1.2), lies on the surface of the sphere, while a mixed state will be a point inside the sphere. A more complete treatment of pure and mixed quantum states can be found in [11, 5].

Once we have the quantum analogous of a classical bit, we need also logic gates that can perform operations among the qubits. In particular, the C-NOT (or controlled-not) gate, which is the quantum counterpart of the classical XOR gate, takes on a great importance in this field. In fact, while other quantum gates, as Hadamard and Pauli gates, involve single qubits, C-NOT is a highly-entangling two-qubits gate, that where the interaction between qubits [54] is needed. To explain the operation performed by C-NOT gate, let's consider two qubits T and C, where T is the target and C is the controlling qubit. When C is in the $|0\rangle$ state, the state of T is conserved, while if C is in the $|1\rangle$ state, the state of T flips, regardless of its initial state. This behaviour can be described

with the following matrix:

$$\text{C-NOT} : \begin{bmatrix} 1 & 0 & 0 & 0 \\ 0 & 1 & 0 & 0 \\ 0 & 0 & 0 & 1 \\ 0 & 0 & 1 & 0 \end{bmatrix} \tag{1.4}$$

While single-qubit gates are relatively simple to realize, since they only need to manipulate a single qubit, the interaction required by C-NOT gate is nontrivial, and in the meanwhile essential to build a complete quantum computing machine [54]. The first all-optical C-NOT gate was experimentally demonstrated in 2003 by O'Brien et al. [55]. It is worthwhile to mention the realization of a C-NOT gate in integrated quantum circuit by Politi et al. in 2008 [56], using a silica-on-silicon chip with waveguides and directional couplers.

Another example of quantum computation is represented by boson sampling. It can be considered as an intermediate quantum computation system, where it is estimated that with about 20 single photons one could solve complicated tasks that are hardly solvable for classical computers [54]. Sampling became a hot topic in quantum computation as soon as Aaronson and Arkhipov in 2010 showed that the operation of a passive linear optics interferometer, with single photons as inputs, cannot be simulated by a classical computer [7]. In fact, if one wanted to sample the output distribution of such a circuit utilizing photon-counting detectors, the prediction of the output would require to a classical machine exponentially growing resources and time. This problem, known as the boson-sampling problem, is exhaustively treated in a review by Gard et al. [54], while we refer to [57, 58, 59] for some recent examples of integrated circuits performing boson sampling.

An efficient implementation of quantum computation, in which quantum objects are used for logic operations, would bring to a drastic increase of computational capability and would also allow to solve certain problems that could not be solved easily with classical computation. Gard et al. in reference [54] clearly identified three types of problems in which quantum computation overcomes the classical one:

- **Shor's algorithm** can be considered as the first algorithm exploiting the potential of quantum computing. It makes use of the quantum Fourier transform to factorize the product of two prime numbers with a speed that is exponentially higher than any method based on classical computation. In fact, given 2^n numbers, a classical fast Fourier transform would require a number of operations that increases as $n2^n$, while in a quantum machine it would increase as n^2, thus polynomially instead of exponentially [5, 4].

- **quantum search algorithms**, among which Grover algorithm [6] is probably the most famous, exploits superposition principle to speed up

search. If one wants to find a specific element into an unstructured database of n elements, with a classical machine the computational complexity increases with n, involving $O(n)$ operations, while a quantum search would require instead $O(\sqrt{n})$ operations!

- **quantum simulation**: the use of qubits could allow to perform accurate simulations of quantum system. While the computational time required by a simulation of N quantum elements would increase exponentially for a classical machine, it would increase linearly using a quantum machine! One interesting example is represented by quantum walk: for instance, classical machines are not able to solve a quantum walk for more than one indistinguishable particle. In 2010 the quantum walk of two entangled photons was demonstrated by [60] in a quantum SiO_xN_y (silicon oxynitride) waveguides, providing a potentially new prototype of quantum simulator. A more detailed overview on quantum simulations can be found in [61].

As can be found in literature, a lot of different physical systems are being studied for the implementation of quantum computing, among which photons are particularly promising for some reasons that will be summarized in section 1.1.3. Whether one wants to use a full linear optical quantum computer (LOQC) or an intermediate quantum system like boson sampling, the use of photons in order to realize optical quantum computing needs the development of integrated quantum circuits, for which elements to generate, manipulate and detect photons are necessary [2].

1.1.2 Secure communication with quantum key distribution

While for quantum computing different strategies are being explored, photons already seem to be the best solution for quantum communication and cryptography.

The ability to generate qubits with a precise quantum state is essential for cryptography, i.e. for having the ability to share an information in a secure way. One of the basis of quantum cryptography consists of the *no-cloning* theorem, according to which a quantum state cannot be identically reproduced [8]: exploiting this property a qubit-encoded information can enable totally secure communication protocols.

Typically, the simplest example of secure communication involves two parties, named Alice and Bob, that want to share a secret message via a public channel, and an eavesdropper, referred to as Eve, that does its best to intercept the message without being noticed. One speaks about *encryption*, in particular, when the information is encrypted and sent together with a cryptographic key, which can be used to crypt and decrypt the message. In quantum communication systems, the quantum properties of the qubit are exploited for

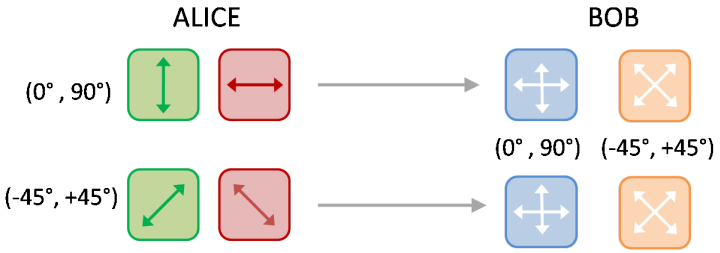

Figure 1.2: Schematic representation of the possible cases for Alice and Bob to send and detect the polarized photons that will be used to share the key in the BB84 protocol, as explained in the main text.

transmitting only the key, which is much easier than doing it for the whole message. One usually refers more precisely to this method as *quantum key distribution* (QKD), instead of the more generic term *quantum cryptography*.

BB84 protocol

The BB84 protocol, from Bennett and Brassard [9] is the first QKD protocol, and probably the most famous. The original idea was to exploit quantum discrete variables, like polarization of photons, so we will refer to this example for simplicity, keeping in mind that it could be implemented with any pair of conjugate properties of a quantum object. In this protocol, when Alice wants to send a bit to Bob, she can choose at random one out of two bases: one with horizontal $|0°\rangle$ or vertical $|90°\rangle$ polarization and the other one with diagonal ($|-45°\rangle$ or$|+45°\rangle$) polarization, resulting in four possible states in total, as represented in Fig. 1.2. When Bob gets the message, he has to choose (randomly also in this case) one of the two bases to measure it, but every time that its basis is different from the one used by Alice, their results will be uncorrelated. Therefore, they have to perform an error correction via a public channel, where Alice declares which basis she used to send each qubit, while Bob declares the basis used to measure it so that they can discard the qubits for which they used different bases. Finally, they keep the bits for which they used the same basis to build the so called *sifted key*. Alice and Bob already know that with this method they have to discard about 50% of the key.

The security of QKD relies in the impossibility to measure a quantum state without perturbing it, and to the mentioned no-cloning theorem. This is one of the most exclusive features of quantum information, since it gives to Alice and Bob the ability to find any eavesdropper trying to detect the key. Let's consider for example a simple eavesdropping strategy, called *intercept-resend*, in which Eve tries to intercept the message from Alice and to resend it to Bob. Eve can measure the polarization state of the photon in one of the two basis, in the same way that Bob would do, and sends a new one in the same state obtained in her measurement. The probability that Eve, when resending

the photon, uses the same basis of Alice, is about 50%, thus she is able to successfully get half of the information. In this case, when Alice and Bob are comparing the key and discarding the bits for which they used a different basis, they will notice that for more than 50% of the states measured by Bob are not compatible with the basis declared by Alice. In this way, with the assumption that Eve is intercepting and resending all the bits, there will still be a 25% of error in the sifted key, in the sense that Bob measures a polarization state that is not compatible with the basis declared by Alice, and so they can know that the channel is not secure.

While the described protocol needs single photon sources, a variation of the BB84 scheme developed by Ekert in 1991, entanglement-based QKD source [10]. This makes not only single photons, but also entangled photon pairs, suitable objects for the implementation of secure quantum communication. Moreover, the use of entangled photons could provide several advantages: in fact, it could prevent unintended information leakage, and using one photon of the pair to enable the detector to reveal the other photon, could lead to a reduction of the noise [1].

QKD sysyems are already commercially available, but in order to include them in a large-scale secure communication network, one needs them to be cheap, scalable and integrated [62]. Current systems make use of attenuated lasers as sources, whose main drawback consists of limited working distance [3]. Amplifiers and repeaters constitute just a faulty solution, since the impossibility to clone a quantum state translates into intrinsic high losses from the repeaters.

1.1.3 The reasons for integrated photon sources

There are several reasons for which photons are probably the most promising candidates to implement quantum information processing.

While for quantum computing also other routes are being widely investigated, as trapped atoms or ions, nuclear spins, quantum dots, superconducting systems or electron spins in semiconductors [63], photons appear to be the most promising choice in the field of quantum communication. First of all, they are characterized by long coherence time at room temperature, which makes them optimal vectors for long-distance quantum communication. From a more utilitarian point of view, photons could travel through an already existing infrastructure, exploiting the worldwide optical fiber network for high-speed transmission of data. An advantage both for quantum communication and computation, consists of the possibility to manipulate photons with complementary metal-oxide-semiconductor (CMOS) compatible photonic devices. This is essential if one wants scalability, low cost, fast manufacturing and possibility of mass production, as will be discussed in more detail in chapter 2. However, one of the strongest motivation to use photons for the implementation of qubits is that they allow relatively easy access to quantum superposition and entanglement. They can be used to encode qubits in many different de-

grees of freedom deriving from different entangled properties of photons such as polarization, time-energy, time bin, orbital angular momentum.

1.2 Single-photon sources

When we refer to "source of non-classical state of light" we can mean a huge variety of states. This includes, for instance, Fock states, i.e. states with a precise number of photons, like single photons or photon pairs, or squeezed states [11]. This thesis is intended to discuss in more detail the generation of single photons and photon pairs that can be used for different applications, but in particular for computing and communication. We will begin this section giving a definition of single photon sources, together with some relevant practical examples. Then, an important distinction between deterministic and probabilistic single-photon sources will be discussed. Deterministic sources are based on single emitters, that usually require the excitation and controlled de-excitation of a system. Probabilistic sources are based on parametric processes in nonlinear materials, where the emission of a pair of photons is not directly controllable, and one must exploit the so called *heralding* to employ them as single photon sources. We will also see that photon pairs can have different degrees of correlation: if they are indistinguishable they are considered as good candidates for heralding, while if they are entangled one can exploit the advantages brought by their correlation, for example in QKD application.

A single-photon source should be in principle deterministic, i.e. it must emit a single photon every time that is requested. In particular, one wants a high probability of emitting one photon $P(n = 1) = 1$, while the probability of multiple emission should be as low as possible, ideally equal to zero $P(n > 1) = 0$: this feature is commonly known as *anti-bunching*. Moreover, the repetition rate should be high and controllable, and subsequently emitted photons should be indistinguishable.

A key parameter to quantify how much single photons are anti-bunched is the second order correlation function. It basically consists in the probability of detecting two photons emitted with a relative time delay τ, as can be inferred by its definition:

$$g^{(2)}(\tau) = \frac{\langle \hat{a}^\dagger(t)\hat{a}^\dagger(t+\tau)\hat{a}(t+\tau)\hat{a}(t)\rangle}{\langle \hat{a}^\dagger(t)\hat{a}(t)\rangle^2}. \tag{1.5}$$

where $\hat{a}$ and $\hat{a}^\dagger$ are the annihilation and creation operators. For an object that can't emit more than one photon at a time, the correlation function at zero time delay will be $g^{(2)}(0) = 0$, as in the case of single atoms. For anti-bunched photons the inequality $g^{(2)}(\tau) < g^{(2)}(0)$ must hold, meaning that the probability of detecting two photon at a time delay τ is always larger than the probability of detecting them at the same time [11, 13]. For simplicity, we can say that $g^{(2)}(0)$ is a good estimate of the single-photon purity of a source.

From an operative point of view, $g^{(2)}$ can be determined with an Hanbury-Brown and Twiss (HBT) experiment. Here, the photons emitted by the source to be studied are sent to one input of a 50:50 beam splitter, whose outputs are directed to two distinct photo-detectors, with a certain delay in each path that can be electronically controlled [64]. What one expects from an ideal single photon source is $g^{(2)}(0) = 0$, however, the minimum value that can be measured is always limited by the time response of the detectors.

Another distinctive property of ideal single-photons is the *indistiguishability*. In fact, this property is required in order to achieve two-photon interference, which is at the heart of QIP implementation. In order to determine the degree of undistinguishability among two photons, the Hong-Ou-Mandel (HOM) measurement can be carried out. In this fundamental experiment, two single photons are interfered on a 50:50 non-polarizing beam splitter, whose two outputs are recorded by distinct single-photon detectors. HOM interferometer can be seen as a variation of the already mentioned HBT, with the difference that here the fields are incident on both inputs of the beam splitter as opposed to just one. The working principle is based on the Hong-Ou-Mandel effect: when two photons are sent to two inputs of a 50:50 beam splitter, as a consequence of bosonic statistics for indistinguishable particles, they will always leave through the same output port [65]. Thus, when counting the coincidences between the two detectors, if the photons are fully indistinguishable, there will be a dip in the coincidences at zero time delay, also known as Hong-Ou-Mandel dip, due to the fact that both photons exited from one arm and none of them from the other arm. The degree of indistinguishability that can be extracted with a HOM interferometer is equal to the peak area of coincidence events detected when two photons that were emitted consecutively meet on the beam splitter [66]. Finally, an ideal source must have a strong *brightness*, but it is not easy to be achieved both in deterministic and probabilistic source. Extraction efficiency becomes a strategic property, in fact when it is too low it can reduce the intrinsic brightness of the source.

A very simple solution to approximate single-photon states is that of coherent states with an extremely low mean photon number. It can be easily realized with modulated and attenuated semiconductor lasers, as explained in reference [1]. However, besides the practical issue of integrating a laser source, they are also typically characterized by a low generation rate.

1.2.1 "Single-emitter" deterministic sources

A deterministic source can be described as a two-levels system in which, starting from a prepared excited state, the de-excitation with emission of a single photon *on-demand* happens after an external stimulus.

On the other hand, heralded single-photons can be obtained from probabilistic sources, separating two photons of a couple, and using one of them as an announcement for the other one. As a matter of fact, the difference between deterministic and probabilistic sources is not so strict. In fact, even in a de-

terministic source, losses have a probabilistic behaviour and cannot be totally avoided: as a consequence, from a more operative point of view, deterministic sources have a probabilistic-like behaviour due to losses [13].

An issue with single emitters consists of the difficulty in fabricating identical emitters. For this reason, they are not considered the best option to generate indistinguishable photons. Moreover, single emitters typically suffer from dephasing, and also of the emission at random spatial directions. These issues can be drastically reduced confining the sources into resonant cavities, as will be better explained in the next sections.

Trapped atoms

The most basic example of on-demand single-photon source is constituted by trapped single atoms, but also trapped ions or molecules. The idea of exciting an atom with a consequent de-excitation and emission of a single photon seems straightforward, but its realization is not trivial. In fact, an individual atom must be captured, for example with a magneto-optical trap, prepared in an initial state and kept in a cavity where is excition and de-excition can be controlled. With this method, qubits can be created exploiting atomic transitions, and logical operations can be performed with attenuated laser pulses. This system is characterized by low noise level and by HOM interference with high visibility, but its practical realization takes lot of efforts. In fact, capturing the atom and preparing it in the initial state needs sophisticated experimental set-ups, making it not suitable for integration, and coherence length drops down when increasing the size of the system. We refer to [14] for more details on single atoms.

Quantum dots

Semiconductor quantum dots are being intensely studied as single photon sources. They are interesting because of the possibility of fabrication with self-assembling processes, of tunability in many degrees of freedom, and deterministic single-photon emission obtained through transitions among atomic-like discrete levels. In fact, a quantum dot is a nanometer-sized semiconductor that behaves like an artificial atom: due to the quantum confinement effect, it has discrete energy levels, with an energy gap higher than that of the bulk semiconductor. In the simplest picture, when the dot is optically excited with a radiation having sufficient energy, it can be absorbed by an electron and an exciton, i.e. an atom-like electron-hole pair, is created. When the exciton recombines radiatively, a single photon can be emitted. In particular, in *core-shell* QD, an outer shell of a material with a wide bandgap is surrounding an inner core semiconductor with a narrower band gap. In this way, the external shell works like an *antenna* that absorbs a photon, while the core emits a photon at lower energy.

In order to avoid multiple emissions one must have only one exciton at a

time, which can be obtained maintaining a weak-excitation regime. However, the processes in quantum dots are complicated by the possibility of other radiative and non-radiative de-excitation processes that could deteriorate the emission efficiency. In order to avoid that, when dealing with quantum dots, much efforts are spent for the selective excitation of a single exciton, together with a subsequent spectral filtering, in order to suppress any multiphoton contributions. The emission rate can instead be stimulated by means of a resonant excitation [67, 16, 20].

Since the first pioneering works, quantum dots for single-photons generation are usually enclosed in resonators to better exploit their emission properties. This is motivated with the well known Purcell effect, that consists in the enhancement of the spontaneous emission from a quasi-monochromatic dipole inside a cavity. In fact, the presence of the cavity selects the number of the electromagnetic modes to which the dipole can couple [68]. The work by Gérard et al. in 1998 is one of the pioneering works where this effect is exploited in semiconductor-based optical microresonators [69].

A milestone in this field is represented by the demonstration of Hong-Ou-Mandel interference from single photons emitted with quantum dots in pillar microcavities, reported by Santori et al. in 2002 [67]. Single photon emission from disparate kind of microcavities have been reported, among whih we mention nanowires [17], micropillars [18], planar microcavities [70], and photonic crystal cavities [19], struggling to reach better directionality and enhance the extraction efficiency.

Matching a high brightness and high indistinguishability in QD single-photon emitters is particularly challenging. In fact, in order to obtain a high brightness the system needs a strong optical excitation, to which the creation of carriers is associated. This leads to a dephasing with a consequrent reduction of the indistinguishability. Very recently, it was possible to generate single photons on-demand with high indistinguishability and extraction efficiency [71]. In this promising work, Ding et al. reported an extraction efficiency of 66%, single-photon purity of 99.1%, and photon indistinguishability of 98.5%.

Another breakthrough consists of the recent measurement of a fully on-chip interference between photons emitted by distinct single quantum dots. This result was achieved using single self-assembled InGaAs quantum dots on suspended waveguides stimulated with an external laser. [72]

Very recently, also Somaschi et al. reported a near-optimal single photon source, able to generate on-demand ultra-pure indistinguishable photons. [73] This was achieved with resonantly excited InGaAs quantum dots in electrically controlled cavities. One of the most noticeable points in this work consists in the capability to combine strong indistinguishability with high brightness, which is fact overcoming other sources of the same quality by more than one order of magnitude. In fact, an HOM visibility of 99% comes together with a brightness of 16%. However, it was pointed pointed out that even in the best available solid state photon source, such reported brightness is referred to

the collection at first lenses, while the absolute emission efficiency is actually below 1% [74].

Another critical point about quantum dots is the dephasing, which has been deeply analysed in reference [75], where time- and temperature-dependent HOM experiments were used to gain information about the effects of dephasing in the indistinguishability.

What is commonly considered to be the main drawback in this kind of sources, however, is the need to work at low temperatures. In fact, in most of the mentioned references the measurements were performed around 4K, therefore needing liquid helium to cool down the system [72, 73]. Low temperatures in solid state sources are necessary to prevent thermal depopulation, and to contrast Coulomb and phonon-induced scattering, in order to guarantee the coherence that is required to generate single photons [66]. This is for sure a limiting factor in the perspective of scalability and mass production.

Colour centres

A common strategy to try achieve room temperature operation involves colour centres in diamonds as single-photon sources. Their energy structure can generally be represented with a three-level system with a ground level $|g\rangle$, an excited level $|e\rangle$ and one metastable state $|s\rangle$, also called *shelving* state, that is thermally coupled to the excited state. The emission happens when the system relaxes from state $|e\rangle$ to state $|g\rangle$, while it stops when the system is in state $|s\rangle$. A shorter lifetime of the excited state reflects in a higher emission rate of single photons, while a longer lifetime of the shelving state decreases the emission rate, and can affect the statistic properties of emission, even translating into bunched emission [13].

Here will be mentioned just a few examples among a huge variety of colour centers, realized with different materials, that are able to provide photons with tailorable wavelengths and linewidths. For a more complete view on diamond nanophotonics we refer to [23].

One leading kind of colour center is constituted by nitrogen vacancies (NV), formed by a nitrogen atom and a vacancy situated in adjacent lattice sites of a diamond. Thanks to the coherence of the electron spin in the defect, the emission from NV can provide highly-indistinguishable single photons. The polarization of the emitted photon can also bring information about the electronic spin of the defect. In fact, the spin of the electron in the vacancy and the polarization of the emitted photons were demonstrated to be entangled quantities [76].

Using NV as single photon sources requires the collection of indistinguishable photons that are simultaneously emitted by different colour centers, thus the indistinguishability can be greatly affected by collection efficiency. A solution to this is given by nanophotonic devices, that allow one to tailor the emission bandwidth and the lifetime, as well as to increase the collection efficiency. Babinec et al. in 2010 showed that the use of nanopillars could

enhance the collection efficiency by one order of magnitude with respect to bulk diamond. [20] A noticeable result that was achieved with NV centers as single-photon sources is the recent loophole-free violation of Bell inequalities over a distance of 1.3 kilometers [77] (for which we refer to section 1.3.1).

Another kind of colour centers worthwhile to be mentioned consists of silicon vacancies (SiV). Their emission is characterized by a narrower linewidth and shorter lifetime (around 1ns) with respect to NV at room temperature [23], making them more suitable for applications in quantum communications. They have high single-photon emission rate, as 6 million of counts/second have been reported in [22].

One of the main disadvantages of colour centers is that they are not identical and not easily tunable [13]. Interference between two photons emitted by remote NV in diamond have been measured: in such experiments, electric fields were employed to induce Stark effect, in order to tune the optical transitions [21, 78]. Another huge disadvantage is given by the low coupling with photonic structures [3], which indeed constitutes an obstacle to the realization of integrated sources.

1.2.2 Probabilistic sources

A different approach is that of *heralded* single photons exploiting probabilistic sources, where single photons are obtained from the separation of photon pairs. The great interest in heralded photon sources finds its basis in the seminal paper by Knill, Laflamme and Milburn, in which the realization of a non-deterministic C-NOT gate was purposed. [12] In their scheme, in fact, the required nonlinearity could be achieved using the extra herald photons, that don't take part in the computation, combined with the intrinsic nonlinearities of the detectors.

The process of heralding involves one herald (or *conditioning*) photon, that is the first to be revealed, and is used to announce the presence of the other photon, namely the *heralded*. In principle, the heralded photon should be deterministically in the nonclassical Fock state with one photon [79]. In order to experimentally proof that the heralded photon is in the Fock state with n=1, a triple coincidence measurement has to performed. In fact, let's consider an experimental setup in which the photons are separated, and one of them is sent to a detector, while the other one is sent to a Hanbury-Brown Twiss (HBT) interferometer. Assuming that there are not multiple emissions, when the conditioning photon has been detected, the probability of detecting a coincidence event of the heralded photon on the two detectors at the outputs of the HBT interferometer, is expected to be zero. In particular, the heralded photon is said to be in a non-classical single-photon state if the normalized triple coincidence rate is less than one [11].

Together with high single-photon purity, a heralded photon source needs also a good preparation efficiency η_P (also known as heralding fidelity), that can be defined as the probability that a heralded photon is output after be-

ing previously announced. It can be extracted from experimental data of a cohincidence measurement using the following equation:

$$\eta_P = \frac{C - C_A}{N\eta_D} \tag{1.6}$$

where C is the peak coincidence count rate, C_A is the accidentals count rate, N is the conditioning-photon count rate, and η_D is the detection efficiency [80].

Heralding requires that the photons constituting the pair are emitted simultaneously, or with a known delay. For this reason, they are usually generated exploiting parametric processes in nonlinear materials.

Parametric nonlinear effects: PDC an FWM

Two processes that are commonly used to generate heralded single photons are Parametric Down-Conversion (PDC) and Four-Wave Mixing (FWM), that take place in materials with nonlinear optical susceptibility of second- and third-order respectively. While we refer to paragraph 2.3 for a more detailed treatment of nonlinear susceptibility, here we intend to give a brief explanation, necessary to introduce heralded single photon sources:

- **PDC** can happen in media with a non-vanishing second order nonlinearity, and can be described as the "splitting" of a pump photon at energy ω_p into two photons at energies ω_i and ω_s, namely idler and signal. The process requires the conservation of energy and momentum, thus the relations $\omega_p = \omega_i + \omega_s$ and $\mathbf{k_p} = \mathbf{k_i} + \mathbf{k_s}$ must hold.

- **FWM** process instead is due to the third-order nonlinearity of the material. It consists of the interaction between four fields, and where two incoming photons are converted into two photons at different energies. If we consider the degenerate case, two pump photons at energy ω_p are annihilated and two signal and idler photons at energy ω_i and ω_s are created. In this case, the conservation of energy and momentum are $2\omega_p = \omega_i + \omega_s$ and $2\mathbf{k_p} = \mathbf{k_i} + \mathbf{k_s}$. This process is usually exploited in materials with a vanishing second-order nonlinearity, as in the case of silicon.

Spontaneous parametric down-conversion (SPDC) and spontaneous four-wave mixing (SFWM) are both quantum effects, that find their classical counterparts in the stimulated processes, PDC and FWM respectively, which exploit an additional signal field used to initiate the process. The presence of a stimulus enhances the probability of emission with respect to the spontaneous process, but at the same time results in unbalancing between signal and idler intensities, thus making it not optimal for the generation of photon pairs. That is the reason for which spontaneous processes will be considered from now on.

Furthermore, SPDC and SFWM can be used either as sources of heralded single-photon or of entangled photon pairs, thanks to the high entanglement

in energy and momentum that usually characterizes the generated photons, resulting from the energy and momentum conservation constraints [81]. If the detection of the conditioning photon doesn't allow, for instance, to resolve the spectral mode, the heralded photon will be left in a mixed state of all the possible energies. The heralded photon however can be put in a highly-pure state by properly filtering the conditioning photon and adjusting the length of the nonlinear material, as suggested by Grice, U'Ren and Walmsley [24], so that the detector responds only to a single mode. The price to be paid for this filtering is the reduction of the rate at which heralded photons are emitted [25].

Finally, before giving a review on the latest performances achieved with parametric sources, we point out that one critical point resides in the probabilistic nature itself, that can give rise to multiple emissions. In fact, the output of a SPDC source can be described as

$$|\psi\rangle = \sqrt{a - |\lambda|^2} \sum_{n=0}^{\infty} \lambda^n |n, n\rangle \tag{1.7}$$

where $|n\rangle$ is the Fock state with n photons and λ is the amount of down-conversion [2]. The probability of creating n photon pairs is given by

$$p(n) = (1 - |\lambda|^2)|\lambda|^{2n} \tag{1.8}$$

that can lead to pair bunching, resulting in multiple emission. In order to realize a probabilistic single photon source the parameter λ must be low, otherwise multiple emission would affect the quality of the source. Indeed, one of the main challenges in these sources consists of balancing a good generation rate while keeping a low probability of multiphoton emission. It is estimated that this can be achieved with a probability of generating a single pair around 10% [13]. To solve this problem there are some possible strategies, for instance using photon-number-resolving detectors, or photon multiplexing in order to increase only the single pair emission [82].

Bulk crystalline sources

The early heralded single photon source was obtained exploiting radiative cascade from single atoms. The first realization was reported by Grangier, Aspect and Roger in reference [83], where they exploited double radiative cascade in calcium atoms, pushed by the will to demonstrate the violation of Bell inequalities. Soon, several groups started to exploit parametric processes, in particular SPDC in nonlinear birefringent crystals with strong second-order susceptibility. Kwiat et al. in 1995 in fact could obtain SPDC from BBO (beta-barium borate) crystal, pumped with a single mode Argon laser in the ultraviolet range, with a power around 150 mW [84].

There is a huge variety of nonlinear crystals reported in literature, like KDP and KTP (potassium di- and tri-phosphate), $RbTiPO_4$, $LiNbPO_3$, $LiTaO_3$. We

can cite as an example a work of 2009 in which a KDP 5mm-long crystal was pumped with frequency doubled pulses deriving from a Ti:Sapphire laser at 600 mW [85]. Thus, it seems clear that the main disadvantages associated with these sources is the large footprint and the need of high external pump powers.

Another non-integrated source consists of photonic crystal fibers (PCF) [80], where the fiber was pumped with a pulsed laser to generate photon pairs by SFWM. They were able to reach a relatively good heralding fidelity with respect to contemporary works, on the order of 52%, with a generation rate of about $9 \cdot 10^4$ counts per second.

Integrated sources

The to-date most efficient parametric emitters are periodically-poled lithium niobate (PPLN) waveguides, where the second order nonlinear susceptibility of the material is exploited to get SPDC. The periodical poling in this kind of waveguides is used to guarantee the conservation of momentum, as required by PDC process. One of the seminal works exploiting this kind of source reported a conversion efficiency of about 10^{-6}, thus increasing by 4 orders of magnitude with respect to bulk crystals, where photon-pair interference visibilities of 97% for energy-time entanglement and of 84% for time-bin entanglement were demonstrated [86].

One example of integrated source of heralded photons exploited SFWM in silica photonic chip, in order to take advantage of the low losses characterizing the material. A record heralding efficiency of 80% (considering also the detector performance) was achieved, with a single photon purity of 0.86 and a generation rate of $3.1 \cdot 10^5$ photons per second [58].

A different interesting source, reported by Davanço et al., consists of coupled resonator optical waveguides (CROW) where an array of microrings it used to enhance the SFWM effect by exploiting slow-light in silicon [25]. A modulated diode laser was used to inject a power of 1.7mW in the CROW, allowing to measure a $g^{(2)}(0) = 0.19$ with a generation rate of 220kHz and a CAR above 20.

An important improvement was triggered by Takesue et al. in 2010, when they illustrated how the multi-photon emission could affect the measurement of interference between heralded photons from different sources. In fact, the probability of generating multiple pairs with a single pulse is proportional to μ^2, being μ is the mean pair-generation rate per pump pulse [87]. Thus the probability of detecting interference between the heralded photons with collection efficiencies η, becomes $\mu^2\eta_D^4$. However, η_D that for an integrated device is very low, typically around $10^{-2} \div 10^{-3}$ [82]. A solution to this issue was purposed by Collins et al., exploiting spatial multiplexing of photons in silicon photonic crystal waveguides (PhCW). In fact, they were able to increase the single photon yield without affecting multiphoton generation, demonstrating an overall increase in the heralded single-photon output up to 62.4% from

an integrated C-MOS compatible device [82]. Taking advantage of the low losses achieved with high quality laser-written components in hybrid photonic integrated circuits, it was possible to produce a device exploiting SPDC in PPLN waveguides [88], resulting in the generation of four heralded photons that could be actively routed to the desired output thanks to fast fibre-based switches.

1.3 Sources of entangled photons

This section will focus about entangled photon source, and we intend to begin with a brief clarification. Many of the entangled sources that we could refer to in this section have already been mentioned in section 1.2.2, talking about heralded photon sources. In fact, as already stated, heralded single-photons can be obtained from entangled photon pairs by properly setting some experimental parameters to obtain indistinguishable photons. Photon pairs generated with parametric processes can be used not only as pseudo-single-photon source, on the contrary one could exploit the strong correlations due to entanglement.

Since we still didn't give a proper definition of entanglement, we dedicate the first paragraph to that, introducing also Bell inequalities. At this point in fact we need a definition of entanglement as a basic property of nonclassical states of light, but at the same time we want to address the attention the demonstrations of Bell inequalities, that constitutes one of the strongest stimuli to the development of entangled photon sources. We start by saying that we don't intend to give an exhaustive treatment of Bell inequalities and loopholes, while our purpose is to underline the importance of entangled photon source in fundamental research, even for a better understanding of nature and of quantum mechanics.

One of the features that make photons a suitable tool to implement QIP consists in the possibility of encoding qubits with photon pairs that are entangled in different degrees of freedom. For this reason, the section will be dedicated to a description of different ways in which photons can be used for qubit encoding: polarization, phase, including the case of time bin and energy-time, and path. Finally, we will report on some significant result in the field of integrated sources of entangled photons.

1.3.1 Bell inequalities

When we refer to entangled photons pairs, we indicate a bipartite system in a pure state, where each individual particle is in an indefinite state quantum correlated to the other one. If we consider two distinct systems A and B, belonging to Hilbert spaces H_A and H_B respectively, the pure state of the system can be expressed as:

$$|\psi\rangle_{AB} = \sum_{ij} a_{ij}|i\rangle_A|j\rangle_B \tag{1.9}$$

where $|i\rangle$ and $|j\rangle$ are complete basis for Hilbert spaces A and B, and the coefficients must fulfill $\sum_{ij}|a_{ij}|^2$. Here, a distinction has to be made between separable states and entangled states. In a separable state the two sub-systems are independent and can be expressed as the inner product of their individual wavefunctions, as the state

$$|\psi\rangle_{AB} = |\psi\rangle_A \otimes |\psi\rangle_B \tag{1.10}$$

belonging to the Hilbert space $H_A \otimes H_B$. If the bi-partite system can't be described by such a separable state, it is entangled. One of the most common basis used to describe two entangled qubits that can assume states $|0\rangle$ or $|1\rangle$ is represented by the following Bell states:

$$|\phi^+\rangle = \frac{1}{\sqrt{2}}(|00\rangle + |11\rangle) \tag{1.11}$$

$$|\phi^-\rangle = \frac{1}{\sqrt{2}}(|00\rangle - |11\rangle) \tag{1.12}$$

$$|\psi^+\rangle = \frac{1}{\sqrt{2}}(|01\rangle + |10\rangle) \tag{1.13}$$

$$|\psi^-\rangle = \frac{1}{\sqrt{2}}(|01\rangle - |10\rangle). \tag{1.14}$$

Entangled systems were at the heart of the famous paradox described by Einstein, Podolsky and Rosen in 1935 [89], in which they intended to prove the incompleteness of quantum mechanics as an instrument to describe physical reality. In fact, they argued that quantum mechanics, denying the possibility to predict events by assigning values for properties of individual particles, could not be used to describe our reality. In their historical work, they considered two conjugated variables A and B of two distinct entangled particles. The fact that they are conjugated implies that they are bound by Heisenberg's uncertainty principle. However, since they are entangled, a measurement of quantity A implies the conjugated quantity B to become instantaneously undetermined, regardless of the distance between the particles, which could be ideally put at an infinite distance. This is in contrast with the definition of local theory, where two events that are spatially-separated and influencing each other, they will be separated by a time interval longer than the time it takes for light to go from one point to the other. The described situation would have violated special relativity constraints, thus they proposed an alternative solution: the existence of hypothetical *hidden variables*, constrained by special relativity, that should have granted the locality. According to their conclusion, this was

the only solution compatible with reality as we know it, while a description of reality given by quantum mechanics could not be complete.

In 1963, a turning point was established by J.S. Bell, with his mathematical demonstration that a local hidden variable theory (LHV), as the one supported by Einstein Podolski and Rosen, was actually not compatible with quantum mechanics [90]. His formulation of LHV led to the so called *Bell inequalities*, that are violated by the predictions of quantum mechanics. A simpler reformulation of these inequalities was given by Clauser, Horne, Shimony and Holt (CHSH)[91].

The first experimental work that demonstrated a violation of Bell inequalities was carried out by Alain Aspect in 1981 [92], paving the way to a lot of other research groups. However, such experiments require to make some assumptions that open the so called *loopholes*. In fact, from a practical point of view, a measurement of the violation of Bell inequalities implies that either local realism is false, or that the assumptions made about the experiment are not correct. Let's consider our quantum communication characters Alice and Bob to define the main loopholes, each one bounded to a requirement of Bell's test:

- **locality**: Alice and Bob must have the so called spacelike separation, meaning that their distance must be large enough that an hypothetical local hidden variable can't cause the choice made by Alice to influence Bob's measurement.

- **detection**, or fair sampling, loophole, which consists in the assumption that detectors efficiencies are 100%, which is never the case in experiment. Actually, the heralding efficiency that is required to close the detector loophole in presence of background noise is above 2/3 [93].

- **freedom of choice** loophole, derives from the need of random generators used by Alice and Bob to choose the basis. If the randomness was not guaranteed, a hidden variable could "understand" a dependence between the choices and produce a result that violates Bell's inequalities.

While the demonstration of Bell inequalities closing one loophole at a time has been achieved in several works, scientists have been struggling to perform experiments in which all the loopholes were closed simultaneously. Even if it's impossible to perfectly close all the loopholes, one can set some limit in order to define what is experimentally *loophole free*, as indicated in reference [94]. The development of efficient sources of entangled photons very recently gave the possibility to perform loopholes-free experiments, as reported in [93].

1.3.2 Polarization encoding

Polarization entanglement can be considered as a natural choice for encoding qubits, with a computational basis composed by the horizontal $|H\rangle$ and

vertical $|V\rangle$ polarization states, resulting in a state that can be stated in the form

$$\alpha|H\rangle + \beta|V\rangle. \tag{1.15}$$

The implementation of single-qubit gates can be done by means of waveplates, i.e. birefringent optical devices that can introduce a phase delay between two components of light with orthogonal polarizations. If we consider a linearly polarized photon, putting a *half* waveplate in its optical path will change the polarization direction, while a *quarter* waveplate will change it to a circular polarization. Polarizing beam splitters can also be used to separate photons with different polarization direction into different spatial paths. Polarization entangled photons were first obtained from atomic cascades [92], or from nonlinear effects in birefringent crystals [84]. For sure, polarization entanglement brings some advantages:in fact, it requires simple and efficient analysers, and does not impose severe constraints on the coherence time of the lasers. On the other hand, the drawback in polarization encoding consists of the decoherence in optical fibers, that can be caused even by very small defects in the birefringence, translating into a difficult transmission over long distances [1].

1.3.3 Phase encoding

Also the phase of photons, analogously to polarization, is a variable in which single qubits can be encoded. From a practical point of view, photon phase can be revealed by means of interferometric techniques. In fact, if two photons enter in a balanced interferometer, i.e. an interferometer where the path difference between the arms is shorter than the coherence length of photon, they behaves as coherent light. The two outputs ports of the interferometer can be seen as the computational basis to implement the qubit: in this scheme, all the possible two-level quantum systems can be represented by varying the unbalancing between the arms, i.e. varying their phase difference ϕ. If we indicate the two output ports as $|p_1\rangle$ and $|p_2\rangle$, the general state of a photon exiting the interferometer can thus be described as

$$|\psi_{1,2}\rangle = \frac{1}{\sqrt{2}}(c_1|p_1\rangle + e^{i\phi}c_2|p_2\rangle) \tag{1.16}$$

where c_1 and c_2 depend on the splitting ratio of the first beam splitter in the interferometer. For example, if we restate the BB84 protocol described in section 1.1.2 in terms of phase coding instead of polarization encoding, the basis among which Alice and Bob can choose to send and detect photons are $\phi = 0, \pi$ or $\phi = \pi/2, 3\pi/2$. The two methods in which phase encoding can be implemented are time bin and energy-time, as will be described in the following paragraphs. Both methods exploit the generation of photons with a strong time correlation, as in the case of atomic radiative cascade or parametric processes in nonlinear materials.

Time bin entanglement

A time bin qubit is formed by a coherent superposition of photons in two time intervals that are separated by a time difference much larger than the coherence time of the photons. They can be generated by short laser pulses passing through an unbalanced interferometer, where the length difference between the arms, that must be greater than the pulse coherence length, translates into a phase difference. At the output of the interferometer there will be two time bins, that are two time intervals as long as the duration of the pulse, with a time separation equal to the time unbalance between the two arms. The state after the interferometer becomes

$$|\psi\rangle = \frac{1}{\sqrt{2}}(|1,0\rangle - e^{i\phi}|0,1\rangle), \tag{1.17}$$

where state $|1,0\rangle$ is associated with the photon in the first time bin, thus passing in the shorter arm of the interferometer, while the photon that took the long path, described by the state $|0,1\rangle$, is in the second time bin.

The experimental set-up to create time bin entangled qubits is that of Franson's experiment [95], where the pump pulses after the interferometer pass through a nonlinear crystal, where twin photons, characterized by very strong time correlation, can be obtained through parametric downconversion [96]. Each pump pulse can thus generate a down-converted photon pair in the first or in the second time bin. Provided that the pair-emission probability is low, that is the case of low pump power, one can in principle neglect the probability of generating a pair with both pulses, or two pairs with one pulse. The output of the crystal is then divided with a beam splitter and sent to two distinct interferometers, named Alice and Bob, where they will be detected. If their interferometers are matched to the pump interferometer within the coherence length of the lasers, Alice an Bob will find three time bins when looking at the arrival times of the photons. The first time bin $|0\rangle$ will be that with pump and generated photons that both took the short path of the interferometer, while the third and last one $|1\rangle$ will contain pump and generated photons that both took the long arm. The central time bin contains both the case in which a pump photon took the short path and the generated photons the long path, and vice versa, and can be expressed as

$$\frac{1}{\sqrt{2}}(|0\rangle + e^{i\theta}|1\rangle) \tag{1.18}$$

where $\theta = \phi_p, \phi_i$. Let's introduce the notation $|n_1, n_2, n_3\rangle_i$, where n_j is the number of photons in the j-th time bin, measured in the detector i that can be Alice's (A) or Bob's (B) [96]. Then, considering the difference of arrival times at the two detectors, there will be a central peak given by the sum of three different coincident events. Two of them, that are $|1,0,0\rangle_A|1,0,0\rangle_B$ and $|0,0,1\rangle_A|0,0,1\rangle_B$, can be distinguished knowing the emission time of the laser. The coincident event $|0,1,0\rangle_A|0,1,0\rangle_B$ can be due to two cases: pump photons

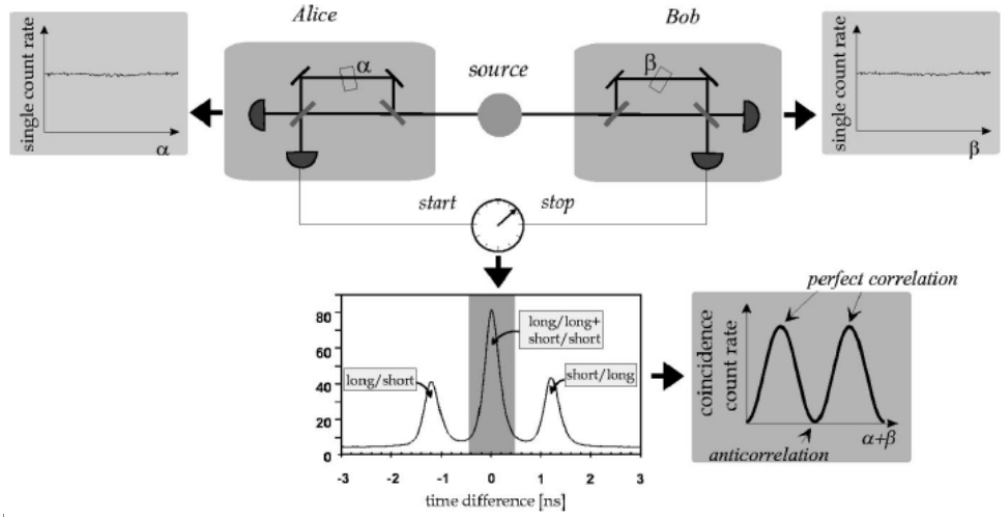

Figure 1.3: Scheme of the set-up for Franson's original experiment. The source can consist of a nonlinear crystal pumped with a cw laser, emitting photon pairs from SPDC. [1].

taking the short path and downconverted photons, generated in the first time bin, both taking the long arms, acquiring phase ϕ_A and ϕ_B, or pump photon taking the long path, and downconverted photons, generated in the second time bin, both take the short path, coming out with phase ϕ_p deriving from the first interferometer. The impossibility to distinguish which of the two paths was actually taken by photons will result in an interference pattern, that in the end is a consequence of the entanglement between the generated photons.

Energy-time entanglement

Energy-time entanglement can be seen as a generalization of time bin entanglement from discrete to continuum time intervals. As in the case of time bin, also in this case photon pairs with strong time correlations are generated. In this case, generated photons are also characterized by strong energy correlation due to the conservation of energy of the process in which the photons are generated. This can be achieved using, instead of a pulsed laser, a continuous wave laser, with a long coherence time, as proposed in the original work by Franson [95], schematically represented in Fig. 1.3. Here, the considered source is a three-level atomic-like system, with levels 1, 2 and 3, where emission results from transitions $1 \rightarrow 2$ and $2 \rightarrow 3$, with the lifetime of level 2 negligible with respect to level 1, while the lowest level 3 is a state with long lifetime, or the ground state of the system. In such system, photons are emitted quasi-simultaneously, and energy correlation is provided by the conservation of energy. First practical realizations exploited SPDC in $\chi^{(2)}$ nonlinear crystals [95, 84], where the signal and idler photons are created in coincidence, and

with energy correlation provided by the long coherence time of the pump. The photon pairs generated in the nonlinear crystal are then separated and sent to two identical unbalanced interferometers, namely Alice and Bob, as shown in Fig. 1.3. The time difference Δt between the two arms of each interferometer must be much higher than the coherence time of the generated photons, in order to avoid single photon interference. In the experiment, the outputs of the two interferometers are detected in coincidence, i.e. the difference in time arrivals between Alice's (A) and Bob's (B) interferometers are measured. As in the case of time bin, there are four possible cases: both photons taking the short path $|s_A s_B\rangle$, both photons taking the long path $|l_A l_B\rangle$ and two cases in which one of them takes the short path and the other one the long path $|l_A s_B\rangle$,$|s_A l_B\rangle$. This results in three coincidence peaks as shown in the graph of the detected coincidences in Fig. 1.3. Here, the central peak results from the cases in which both photons take the long or the short path, represented by the state

$$\Psi = \frac{1}{\sqrt{2}}(|s_A s_B\rangle + e^{i\psi}|l_A l_B\rangle), \tag{1.19}$$

where $\psi = \phi_A + \phi_B$ is the phase difference resulting from the sum of the optical phase difference between the two paths in each interferometer. Since the two cases $|s_A s_B\rangle$ and $|l_A l_B\rangle$ are indistinguishable, the rules of quantum mechanics state that the probability of detecting this state is given by the squared modulus of the sum of the individual amplitudes. Varying the unbalancements, thus varying ψ_A and psi_B, there will be an interference in the detected coincidences described as

$$R_c = \frac{1}{4} V \cos^2\psi, \tag{1.20}$$

where V is the visibility of the two photon interference. A value of V greater than $1/\sqrt{2}$ implies a violation of Bell inequalities and confirms that the measured state is entangled [97].

1.3.4 Path encoding

Another kind of qubit encoding consists of path encoding, where a photon has the possibility to take one path or another one, and the value of the qubit is directly determined by which path was taken. A polarization-encoded qubit can be converted to a path-encoded qubit through a polarizing beam splitter [55], as schematically represented in Fig. 1.4. While polarization encoding is more used in free-space experiments, the development of integrated waveguides allowed to implement *path encoding* in integrated structures. The system can consists of two input channel waveguides A and B, where the value assumed by the qubit is $|0\rangle$, if the photon goes through waveguide A, or $|1\rangle$ if it goes through waveguide B.

The qubit state $\alpha|0\rangle + \beta|1\rangle$, that is an arbitrary superposition of the two optical paths, can be implemented in integrated circuits by means of directional couplers, that can be considered the integrated analogous to beam splitter.

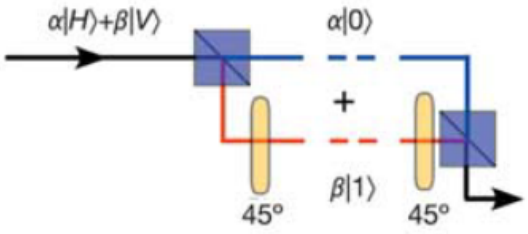

Figure 1.4: A polarization encoded qubit can be converted into a spatially encoded qubit using polarizing beam splitters (blue squares) and half-wave plates (yellow bars) [55].

Another necessary element is a phase shifter, that allows to control the relative phase between the two optical paths[56, 98]. This way of encoding qubits allows to avoid the problems bound to polarization control [99] and to produce reconfigurable systems, as reported also in [100].

1.3.5 Integrated sources of entangled photons

The first polarization-entangled photon pair sources were based on atomic radiative cascade [92, 83]. A further option was provided by quantum dots, that could be used to generate entangled photon pairs exploiting the *biexciton cascade* [26]. Very recently, InAs/GaAs quantum dots embedded in silicon were used as sources of wavelength-tunable polarization-entangled photons [27]. Another remarkable result is represented by the realization of integrated C-NOT gate based on polarization-encoded qubits [101].

While we refer to section 1.2.2 for parametric bulk sources, we will focus here in the generation of entangled photon pairs from integrated devices operating at room temperature.

In 2006, Sharping et al. performed the first demonstration of generation of quantum-correlated photons in a silicon integrated device, in particular exploiting SFWM in silicon waveguides [28]. Although they were able to achieve a good CAR and generation rate (CAR=25 for a photon production rate of about 0.05 per pulse) the footprint was not optimal, since the involved waveguides were up to 1 cm-long. Several other groups studied the generation of correlated photon pairs in silicon waveguides, as reported in [29]. Few years later, time bin entangled photons generated with silicon waveguides reached a CAR=200 with an average number of photon pair per pulse equal to 0.04 and an interference visibility higher than 95% [30]. Silicon wire waveguides were also used to produce polarization-entangled photon pairs [31].

Path-entangled photons were generated with integrated spiral-shaped silicon waveguides, exploiting SFWM effect, where a quantum interference visibility of $100 \pm 0.4\%$ is reported [32].

Structure	Material	Size (μm^2)	Spectral brightness ($s^{-1}nm^{-1}$)	SNR	Ref.
waveguide	Silicon	5000	$4 \cdot 10^5$	30	[30]
CROW	Silicon	8000	$3 \cdot 10^6$	8	[103]
microrings	Silicon	300	$6 \cdot 10^7$	64	[49]
waveguides	PPLN	180000	$7.5 \cdot 10^7$	6	[104]
waveguides	AlGaAs	10000	$6 \cdot 10^5$	7	[105]

Table 1.1: Comparison between room temperature integrated sources of entangled photons. The spectral brightness refer to a coupled pump power of 1 mW and to the internal generation rate. [49]

A slightly different approach exploits the enhancement of SFWM with slow light effect in photonic crystal coupled-resonator optical waveguides (PhC CROW) for the generation of correlated photons [102]. The time bin entanglement with this kind of source was soon demonstrated in reference [103], where a visibility of the interference peak above 70% is reported in a device with a very small footprint, around 400μm. However, to reach a rate of $2 \cdot 10^{-3}$ pairs per pulse, a sample 1 mm-long had to be used, and with a CAR$= 8.7 \pm 1.0$.

In this thesis, we will deal with generation of correlated photons from integrated silicon microring resonators. This kind of device in fact has been recently demonstrated as a bright source of time-energy entangled photons [49]. Table 1.1 compares integrated C-MOS compatible sources of entangled photon-pairs working at room-temperature. As can be inferred from the table, silicon microrings combine a high spectral brightness, comparable to that of the best available sources (PPLN waveguides), with a smaller footprint and best signal-to-noise ratio.

We refer to chapter 2 for a more detailed introduction on silicon photonics and to integrated resonant structures, such as microrings, that allow to enhance the nonlinear process of FWM that can be exploited to generate correlated photon pairs. The following chapters will then describe the experimental works and results that we achieved in this field. Chapter 3 will report the first case of enhancement of FWM in microrings made of porous silicon, showing that this kind of structure can be successfully employed to enhance nonlinear effects even in a medium with a high porosity. In chapter 4 we will face some practical issues bound to the filtering of generated photons: in fact, one of the obstacles to the development of integrated sources of photon pairs is the lack of integrated components to filter the intense pump laser used to excite the system, and to separate the generated photons. Here, we will demonstrate how a device constituted by integrated microrings and distributed Bragg reflectors allows to fully filter the generated photons, that can furthermore be separated and sent to different outputs of the device, where they are ready-to-use without the need of external filters. Finally, in chapter 5 we will show an innovative technique

to measure the joint spectral density (JSD) of photon pairs generated with microring resonators, in order to characterize their energy correlation with fast measurements and unprecedented resolution.

Chapter 2

Silicon Photonics

As thoroughly explained in the first chapter, there is an urgent need to develop electronic devices with integrated optic components. Indeed, it would represent one fundamental road to the implementation of QIP, but it is just one of the applications that may be enabled by an advanced photonic platform, and it is necessary even without invoking quantum technologies. In fact, the intervention of photonic-based technologies is requested by the growing demand of high-speed communication and computational capability. In particular, a bottleneck that is urgent to be faced consists in the slow interconnection among internal components of a computing machine. The development of fast optical interconnections between memory and processor in fact would bring to a huge increase in the computation capability. Moreover, optical connections would help to solve another major issue, consisting in the huge power consumption in electrical connections at high frequencies.

Silicon is a material of enormous interest to solve the above mentioned challenges, because it is already the dominant material in microelectronic industry, and is characterized by very good linear and nonlinear optical properties at telecommunication wavelengths. One remarkable advantage can be found in its compatibility with complementary metal-oxide semiconductor (CMOS) technology, allowing to realize silicon-based optical devices in traditional semiconductor industries, with standard fabrication processes and circuit designs, allowing a substantial elimination of the risks bound to a process development. However, at a small scale, there is a drawback bound to CMOS technology which consist in the high cost of the development of a silicon photonics process. To overcome this issues, institutes like Imec, CEA-Leti, or A*STAR Institute of Microelectronics (IME) played a crucial role, allowing to a wide community to obtain devices realized by an industrial process without the need to run a dedicated process, which would cost hundreds of thousands of dollars. The recent advent of fabs, like Optoelectronic Systems Integration in Silicon (OpSIS) or ePIXfab, gave the possibility to external customers to buy multi-project photonics wafers with high complexity and high integration density, with a significant reduction of the total cost.

We will start this chapter giving an introduction to the basic building blocks of photonic integrated circuits, giving particular attention to wire waveguides and microrings resonators, since they constitute a common subject through all this thesis. In the last section of this chapter nonlinear optical properties of silicon will be discussed. Four-wave mixing in silicon waveguides and microrings will be analysed, making an important distinction between the classical and spontaneous effect. We refer finally to next chapters for more details on the fabrication techniques of silicon photonic devices that have been studied in this thesis.

2.1 Silicon integrated waveguides and devices

The possibility of integrating silicon optical components on a chip became available with the development of silicon-on-insulator (SOI) platform. It consists of a silicon crystalline wafer, with a silicon oxide layer about 2 μm thick and a 220-nm thick silicon guiding layer on top of it. All the elements constituting the photonic integrated circuits can be realized on the top guiding layer by means of litography and etching techniques. SOI is a CMOS compatible material, and allows to obtain photonic circuits with high integration density thanks to the high refractive-index contrast between silicon, which is the guiding material, and air or oxides, which usually constitute the cladding. In fact, a refractive index contrast of 40%, as in the case of silicon and oxide, allows a total internal reflection with a very large incident angle, estimated to be around 60° [106].

Silicon wire waveguides

The simplest structure that can be realized in SOI consists of a channel waveguide, or wire waveguide, where light can be strongly confined thanks to the high refractive index contrast between Si core (n=3.48) and SiO_2 cladding (n=1.46). The current SOI technology allows to fabricate channel waveguides where light is confined into a region of below 1 μm^2. Sub-micrometric confinement is necessary to work in single-mode condition for one polarization, at 1.55 μm wavelength, where silicon has good transmission properties, while absorption is the dominant process at visible wavelengths. In the most common geometry, the width of the channel is about twice the height, leading to a ground mode with TE polarization, which is characterized by strong discontinuity of the field on the sidewall surfaces [39].

The confinement of light in two directions, if one looks for analytical solutions of the wave equations, is a very challenging problem. One of the reasons is due to the evanescent tails of the mode profile out of the waveguide, for which the field experiences an actual refractive index that is lower than the index of silicon. Accurate solutions to this problem can be found with numerical methods, among which effective index method (EIM) is one of the more

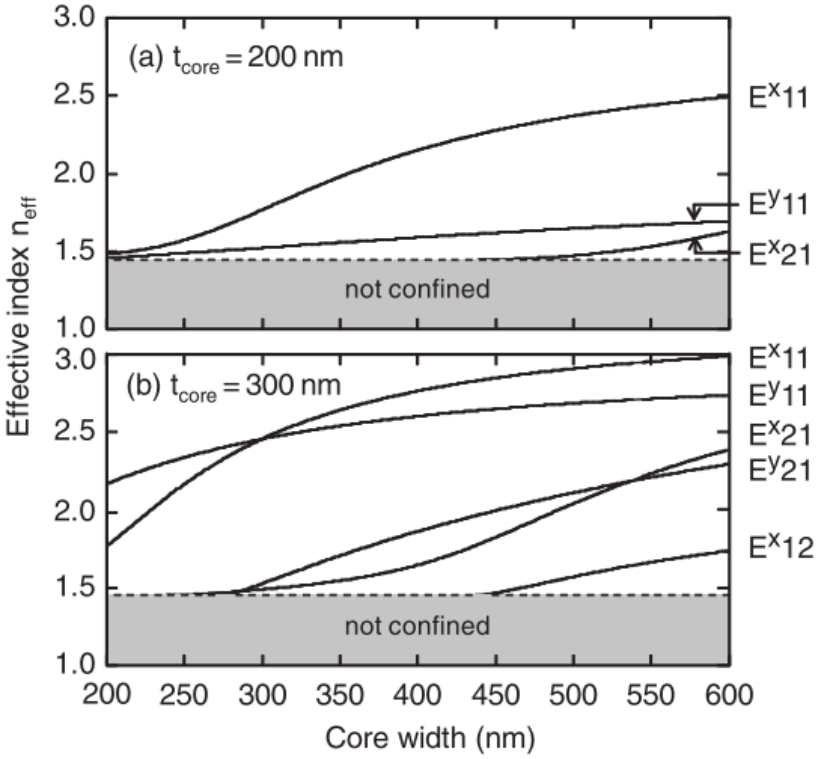

Figure 2.1: Dependence of the effective indices of silicon photonic wire waveguides from their width, for a fixed thickess of 200 nm (a) and 300 nm (b). In both graphs, E^x and E^y represent the TE-like and TM-like modes. [106]

efficient. The method consists of decomposing the rib (or ridge) waveguide into three vertical slices: the central one including the channel waveguide, and the two side regions out of the channel. Each part is treated as an individual slab waveguide, and the TE eigenvalues obtained from their individual solution are used to calculate the effective index of each region. The resulting refracting indices are used to construct an equivalent three-layer vertical slab waveguide, that is finally solved in order to obtained the mode effective index n_{eff}. It is to be noticed that the cross section of the waveguide must be chosen in order to satisfy single-mode condition. The layer thickness is typically fixed at 220nm, which coincides with the thickness of the silicon guiding layer in the SOI platform. The waveguide width can vary between 400 nm and 500 nm: the reasons for these values can be easily understood from Fig. 2.1 (a) [106], where it is shown that for waveguides of 200-nm thickness, the condition of single-mode is achieved when the core width is less than 460nm for TE-like guided modes.

An illustration of a typical cross-section for a silicon wire waveguide with 220 nm thickness, and with 450 nm width, is represented in Fig. 2.2 (c), together with the mode profile obtained from simulation, which allowed also

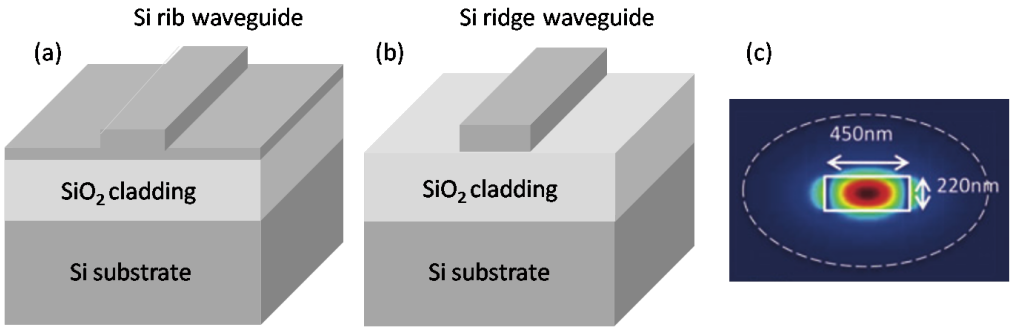

Figure 2.2: Schematic picture of a (a) rib and a (b) ridge waveguide on SOI platform. The dark-grey regions are made of crystalline silicon while the light-grey layer is the silicon oxide cladding, with refractive indices n=3.48 and n=1.46 respectively. In some cases, the top layer can be further covered with silicon oxide in order to reduce losses. (c) Representation of the cross section of an SOI ridge waveguide of thickness 220 nm and width 450 nm, designed to work in TE polarization at telecom wavelengths. Simulations allowed to determine an effective index of $n_{eff} = 2.43$ and the mode profile, here superimposed to the cross section of the waveguide [39].

to determine a mode effective index of $n_{eff} = 2.43$.

Due to the high refractive index contrast, silicon waveguides are characterized by a strong dispersion leading to a wavelength-dependence of the effective index of the propagating mode. In practice, light at different wavelengths will travel through the waveguide with different velocities. One speaks about normal dispersion when the effective index decreases for increasing wavelengths, i.e. $\partial n_{eff}/\partial\lambda < 0$.

The intrinsic absorption in silicon is very low below the band gap (photons with energy below 1.1 eV), therefore the propagation loss of photonic wire waveguides are mainly due to scattering form surface roughness. Typical values for propagation losses in silicon ridge wires are around $2 - 3$ dB/cm in the case of upper air cladding, while they can go be below 2 dB/cm when the upper cladding is made of oxide [39]. Propagation losses depend also on the morphology of the waveguide. For instance, one can have rib or ridge waveguides, as shown in Fig. 2.2 (a) and Fig. 2.2 (b), respectively. As a consequence of the small size of ridge waveguides, imperfections due to the fabrication process are more significant in size, if compared to larger devices, resulting in a substantial contribution to losses. In rib waveguides, the lower refractive effective index contrast between the guiding region and the side regions allows to achieve single-mode guiding even with a larger width. It has been demonstrated that in rib waveguides propagation losses can be strongly reduced, as they can be lower than 0.1 dB/cm [107, 108]. However a lower refractive index contrast leads to a lower total internal refraction, resulting in higher bending losses. In fact, while the bending radius in ridge waveguides can go below 10

μm, the typical value for rib waveguides is one order of magnitude higher [38].

Starting from silicon wire waveguides, various kinds of optical circuit elements can be realized, including directional couplers that can be used as beam splitters, Y branches, distributed-Bragg reflectors, and devices to couple light from an external fiber, as will be reported below. We don't intend to give an exhaustive description to components of silicon circuits, we will instead give a rapid overview, focusing on the components that will be mentioned in the experimental works reported in the following chapters.

Directional couplers

Directional couplers constitute a versatile integrated component, consisting of two parallel optical channels that, within a certain length interval, are brought close to each other. The effect of coupling is possible thanks to the small distance, that allows to the evanescent tails of the modes out of the waveguides to overlap, leading to energy transfer from one waveguide to another [109, 37]. For this reason it can be also referred to as evanescent coupler. The amount of power coupled from a waveguide to the other one depends on the spatial overlap of the mode of one waveguide to the other one, which is determined by the relative distance between the waveguides, from the penetration of the mode into the substrate, and from the interaction length. Thus, a directional coupler can be used as an integrated beam splitter, whose coupling ratio depends on the geometrical parameters of the splitter.

Fiber-to-waveguide couplers

The capability to efficiently couple light into and out of the chip is extremely important for all practical applications, for instance in nonlinear optics, when one deals with weak signals and needs low insertion losses to perform measurements. Providing an efficient coupling between silica fibers off-chip and silicon waveguides on-chip is definitely a demanding issue. In fact, it requires to match the mode profile of a very narrow waveguide, with a cross section below 1 μm^2, and high refractive index contrast, with the mode profile of a silica fiber, whose core has a typical width of $\approx 10\mu$m and a much lower effective index contrast [110]. Coupling structures have to be designed in order to minimize the coupling losses due to this mismatch. Edge couplers and grating couplers can be considered the two main strategies for fiber-to-waveguide coupling, as will be described below.

Edge couplers can be employed to gradually transform a highly confined mode into a wider mode, so that it could be supported by an optical fiber with lower index contrast. Typically, the mode diameter in the waveguide is less than 1 μm, while it is about 10 μm into a standard single-mode optical fiber. In order to match the mode profile, lensed optical fibers can be used on one side, reducing the size of the spot down

to 3μm [110], while on the other side an adiabatic *inverse taper* can be used. This kind of taper is realized by an adiabatic reduction of the cross-section of the waveguide, in order to reduce its effective index and match it with that of the mode of the lensed fiber. With such coupling system, the fiber-to-waveguide insertion loss can go below 1 dB over a broad range at telecom wavelength [110]. The main drawback is that the fiber must be aligned at the edge of the sample: such coupling between a narrow waveguide and a lensed fiber requires a careful polishing of the edge of the chip to reduce losses, and the alignment would suffer from mechanical solicitations, thus requiring a robust packaging.

Grating couplers can be used for vertical (or quasi-vertical) optical coupling between a fiber and an silicon wire waveguide. With respect to edge coupling, gratings can be located anywhere on the chip, not only at the edge, they would not need polishing of the edges of the samples and they could be enclosed in a packaging easier to manage. Grating couplers are diffractive structures, that are usually placed at the end of a lateral adiabatic taper, that can couple light out-of-plane into the waveguide. They produce an exiting mode which can be designed to match that of a single mode optical fiber (around 10 μm), allowing for a direct coupling between the fiber and the chip, with insertion losses that can be as low as 2.5 dB [111, 112].

Distributed-Bragg-Reflectors

Another integrated device that can be obtained out of a channel waveguide is a distributed Bragg reflector (DBR), which can be obtained from a periodical sequence of layers with different effective refractive index. If we look at the graph in Fig. 2.1, it is clear that a periodic modulation of the effective index could be easily obtained by periodically shrinking the width of the waveguides. Mirror reflectivity increases linearly with the number of periods N, while the refractive index contrast affects both the reflectivity and the bandwidth. Recently, a narrow-band integrated DBR on SOI platform has been demonstrated [113].

2.2 Microring resonators

A ring resonator can be defined generally as a cavity in which light travels always in the same direction. A silicon microring in particular consists of a channel waveguide looped back onto itself, forming a circular shape. The typical values for radii are around 10 - 15 μm, but the high refractive index of silicon allows the waveguide to support guided modes even with very small radii, down to 5 μm, allowing to obtain devices with an extremely small footprint. The resonant modes of a microring are at wavelengths λ_0 that are

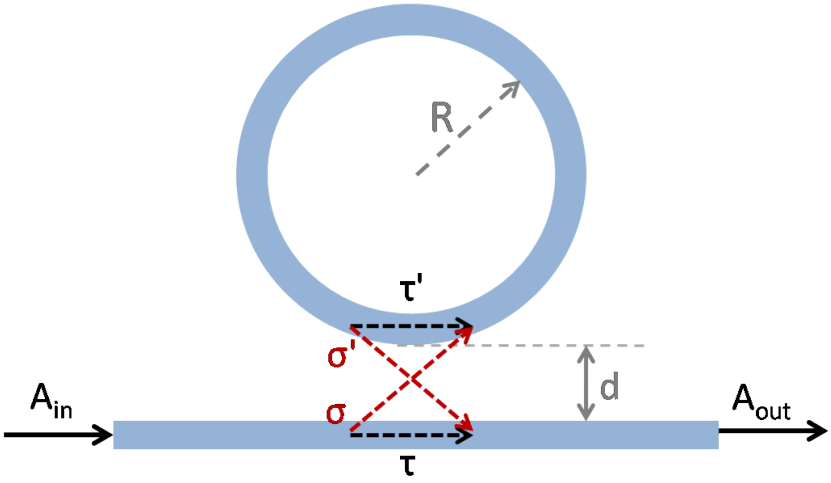

Figure 2.3: Schematic picture of a microring resonator coupled to a waveguide. The gap distance d, which is here exaggerated, can be optimized to get critical coupling. The A_{in} and A_{out} arrows represent the input and output amplitudes, τ and τ' are the transmission coefficients and σ and σ' are the cross-coupling coefficients.

exact multiples of the optical path length of the resonator, i.e. satisfying the following condition for constructive interference:

$$m\lambda_0 = 2\pi R n_{eff} \tag{2.1}$$

where m is an integer number indicating the order of the resonance, R is the radius of the microring and n_{eff} is the mode effective index [37]. The great importance of microrings can be attributed to several reasons. For instance, they allow easy coupling between different modes, and they support equally spaced multiple resonances, separated by an amount that is defined as free spectral range (FSR) of the resonator. In a first approximation, this quantity can be obtained as (2.1):

$$\mathrm{FSR} = \frac{\lambda_0^2}{n_g L} \tag{2.2}$$

where $L = 2\pi R$ is the circumference of the ring and n_g is the group velocity, defined as

$$n_g = n_{eff} - \lambda_0 \frac{\partial n_{eff}}{\partial \lambda} \tag{2.3}$$

which takes into account for the dispersion of the waveguide and is bound to the group velocity by relation $v_g = c/n_g$.

From the experimental measurement of the FSR of the resonator, one could easily obtain the group index n_g from equation (2.2), in fact it can be derived from a fit as the one shown in Fig. 2.4. In the reported graph, the dependence of FSR from round trip length for an all-pass microring resonator is shown, from which is evident the trend FSR $\propto$ 1/L.

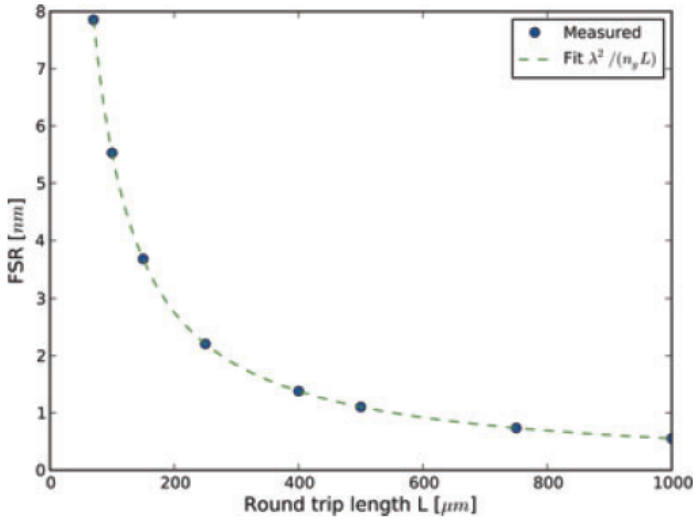

Figure 2.4: Dependence of the Free spectral range (FSR) from the round trip length for an all pass microring resonator [39].

Coupling to the ring

To all practical purposes, a mechanism to couple light into and out of the ring must be provided. The most common coupling mechanism consists of side-coupling with a straight channel waveguide nearby the ring, as in the case of directional couplers. In this way, the coupling is obtained by the overlap between the evanescent tails of the waveguide and guided modes of the ring. In principle, this allows for the complete extraction of the resonant wavelengths, beating the performances of standing-wave resonators, such as photonic crystal cavities, that when coupled to a waveguide can pick up just half of the signal power at resonance [114].

The simplest form to provide in-coupling and out-coupling to a ring resonator consists is the collection of the output in the same input waveguide, as in the all-pass filter (APF) configuration, as illustrated in Fig. 2.3 [39]. If we consider a ring resonator side-coupled to a waveguide, as the one shown in Fig. 2.3, the amplitude of the outgoing field A_{out} can be expressed as a function of the amplitude of the incoming field A_{in} by the following equation [115]

$$A_{out} = \tau A_{in} + \sigma\sigma' e^{-i\delta} \left[1 + \tau' e^{-i\delta} + (\tau' e^{-i\delta})^2 + ...\right] A_{in} \tag{2.4}$$

where

$$\delta = 2\pi n_{eff} L/\lambda_0 = kL \tag{2.5}$$

is the phase-shift induced by a round trip, τ and τ' are the transmission coefficients along the waveguide and the ring respectively, while σ and σ' are the cross-coupling coefficient from the waveguide to the ring and viceversa. It can be noticed that in equation (2.4) the first term on the right side is given by

the simple transmission through the waveguide, while the second term is due to components of light coupling into and out of the ring. If the ring and the waveguide have the same refractive index and cross-section, we can assume that $\sigma' = \sigma^*$ and $\tau' = -\tau^*$, and that $|\sigma|^2 + |\tau|^2 = 1$, meaning that there are no losses in the coupling section. It can be shown that by summing up all the terms of the series in equation (2.4) one gets

$$A_{out} = \frac{\tau + a^{-i\delta}}{1 - a\tau^* e^{-i\delta}} A_{in} \tag{2.6}$$

being a the round-trip loss coefficient in the microring, bound to the power attenuation coefficient of the waveguide α [cm^{-1}] by relation $a^2 = e^{-\alpha L}$. The attenuation takes into account for scattering due to roughness, bending losses, linear and nonlinear absorption.

The transmission of the ring, defined as the ratio between output and input intensity, can be written as [115]

$$T = \left| \frac{A_{out}}{A_{in}} \right|^2 = \frac{a^2 + \tau^2 - 2a\tau cos\delta}{1 + a^2\tau^2 - 2a\tau cos\delta}. \tag{2.7}$$

that when resonance condition is satisfied, i.e. when $\delta = m2\pi$, becomes:

$$T = \frac{(a - \tau)^2}{(1 - a\tau)^2}. \tag{2.8}$$

It can be noticed from equation (2.8) that the transmission at resonance drops to zero when $a = \tau$, i.e. when the cross-coupling transmission is equal to the propagation losses inside the microring. This is the condition for *critical coupling*, at which the maximum power is dissipated inside the ring, and the radiation-matter interaction is optimized [115]. The coupling can be controlled by adjusting the gap distance between the waveguide and the ring: if the gap is shorter with respect to critical coupling condition, the ring is said to be overcoupled ($\tau < a$), while if is larger the ring is in undercoupling ($\tau > a$). When using the microring as a source, one usually need to work in critical coupling condition, in order to optimize the extraction efficiency of signal and idler photons generated inside the microring.

2.2.1 Figures of merit

The typical transmission spectrum of a ring resonator coupled to a waveguide is shown in Fig. 2.5, consisting of a set of equally spaced dip resonances, from which the information about the resonator can be extracted. The full width at half-maximum (FWHM) of the resonances, for instance, is bound to the geometrical parameters of an all-pass ring by the following relation [39]:

$$\text{FWHM} = \frac{(1 - \tau a)\lambda_0^2}{\pi L n_g \sqrt{\tau a}}. \tag{2.9}$$

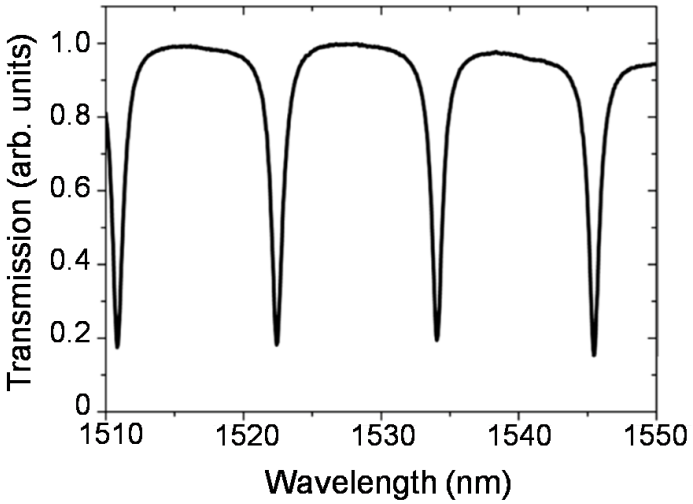

Figure 2.5: Typical transmission spectrum from a straight waveguide coupled to a ring resonator, where the equally spaced dips are the resonances of the microring.

From now on, we will refer to FWHM only when considering the frequency domain, in order to distinguish it from the linewidth in the wavelength domain, that will be referred to as $\Delta\lambda$.

An important figure of merit for a resonator is the finesse $\mathcal{F}$, which is a measure of the width of the resonances (FWHM) with respect to their separation, as results by its definition

$$\mathcal{F} = \frac{\text{FSR}}{\text{FWHM}}. \tag{2.10}$$

The physical meaning of finesse is represent by the number of round-trips covered by light in the resonator before its energy is reduced to $1/e$ of its initial value, within a factor of 2π.

Quality factor Q is another useful figure of merit, depending on the decay time of the energy stored in the microring, closely related to finesse through the FSR. In fact, the Q factor of a the resonator is given by the finesse times the optical frequency divided by the free spectral range. Q factor represents the number of oscillations of the field in the resonator before the circulating energy is depleted to 1/e of the initial energy. An alternative definition for Q is the ratio between time-averaged energy stored and power loss per optical cycle, that for a resonance at frequency ω_0 is:

$$Q = \omega_0 \langle \frac{\text{energy stored}}{\text{power loss}} \rangle. \tag{2.11}$$

In the end, finesse and Q factor are interchangeable, and both allow to estimate the lifetime of light *trapped* in the resonator and to measure the resulting field enhancement.

The intrinsic value of Q is limited by losses, that can be due to absorption, photon scattering from impurities and bending losses of the material [37] or to scattering due to its roughness. By definition, the intrinsic Q factor for an isolated ring is

$$Q_{int} = \frac{2\pi n_{eff}}{\lambda_0 \alpha} \tag{2.12}$$

where, as previously defined, n_{eff} is the mode effective index of the waveguide and α is the loss coefficient. Since the quality factor is affected by the coupling condition, when the ring is not isolated one refers to its *loaded* Q factor, which will always be smaller than the intrinsic one.When the gap distance is d_c, such to obtain the condition for critical coupling, the loaded Q will be $Q_{load} = Q_{int}/2$. If the ring is overcoupled ($d < d_c$) there is a degradation of the loaded Q, while in the case of undercoupling ($d > d_c$) the loaded Q factor will be higher than $Q_{int}/2$, but still lower than Q_{int}.

From a more operative point of view, Q factor can be extracted from the transmission spectrum of the ring, in fact the linewidth of the Lorentzian dips depends on the energy loss coefficient Γ, as described by:

$$T(\omega) \propto \frac{\Gamma}{(\omega - \omega_0)^2 + \Gamma^2}, \tag{2.13}$$

where Γ is bound to the propagation losses α by relation $\Gamma = \alpha c/n_{eff}$. If we consider the system with an initial energy U_0, the stored energy at a generic time t will be $U_S = U_0 e^{-\Gamma t}$ while the lost energy will be $U_L = U_0(1 - e^{-\Gamma t})$. Thus, if we recall equation (2.11), Q factor can be expressed in the form

$$Q = \frac{\omega_0}{\Gamma} \tag{2.14}$$

which, converted into wavelength, becomes

$$Q = \frac{\lambda_0}{\Delta\lambda}. \tag{2.15}$$

This means that, performing a fit of an experimental transmission dip with a Lorentzian function, one can extract its central wavelength λ_0 and full width half dip $\Delta\lambda$, and use them to calculate the Q factor of the resonance exploiting equation (2.15).

Quality factor can be increased by minimizing the losses inside the cavity. For instance, propagation losses can be reduced using materials with high quality, and bending losses can be limited by properly setting the radius of the microring. One must consider, though, that a change in the radius might also affect the coupling losses: in fact, the larger the radius, the longer the path where the fields of the ring and the waveguide are overlapping. The highest Q-factor that can be obtained from silicon microrings with a round-trip length of about 10 mm is calculated to be 1.42×10^5, considering propagation losses around 2.7 dB/cm, that is the typical value obtained from waveguides realized

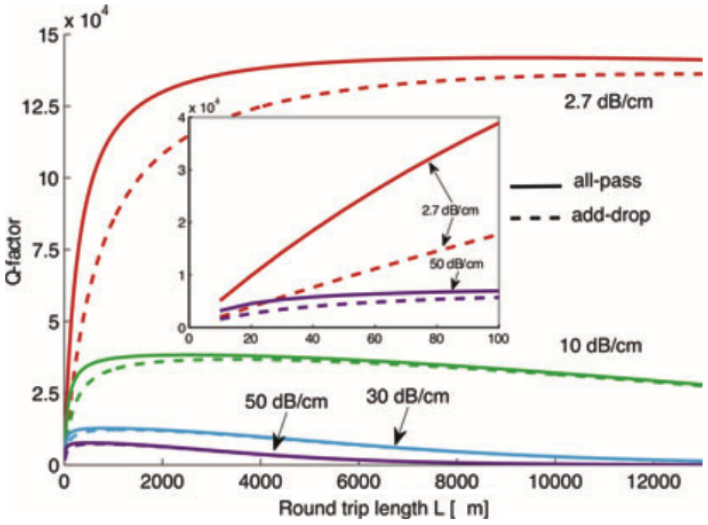

Figure 2.6: Dependence of measured Q factors from cavity length for different propagation losses, relative to microrings in all-pass (solid lines) and add-drop (dashed lines) configurations, both operating at critical coupling [39].

in a standard imec fabrication process [39]. This case is represented by the solid red line in Fig. 2.6. Although such value has been experimentally confirmed [116], it is to be considered a record, while a more realistic typical value is below 5×10^4 [46].

2.2.2 Add-drop configuration

A useful configuration for microring resonators is the so called add-drop, first reported in [114]. In such configuration, the ring is side-coupled to a couple of parallel waveguides on the opposite sides of the ring, as depicted in Fig. 2.7. When the ring is in this configuration, part of the input field that is in resonance with the ring is delivered to the *drop* port, propagating in the opposite direction, while the remaining out-of resonance light is regularly transmitted to the *through* port. It can be interpreted as if the power is transferred between the input and the drop ports via the resonances of the ring. In the case of negligible attenuation, ($a \approx 1$) critical coupling occurs with a symmetric cross-coupling ($\sigma_1 = \sigma_2$), while if one considers a lossy resonator, the gap distances d_1 and d_2 have to be adjusted in order to satisfy the requirement $\tau_2 a = \tau_1$, so that the losses match the coupling. For this reason, critical coupling for add-drops is easier to achieve than for all-pass microrings, since there is no need to compensate for the losses from the waveguides, and one just has to balance the cross coupling of the two directional couplers, as shown in Fig. 2.7.

The Q factor of an add-drop is intrinsically lower than that of an all-pass microring. The reason is intuitive if we think at the Q factor as a measure

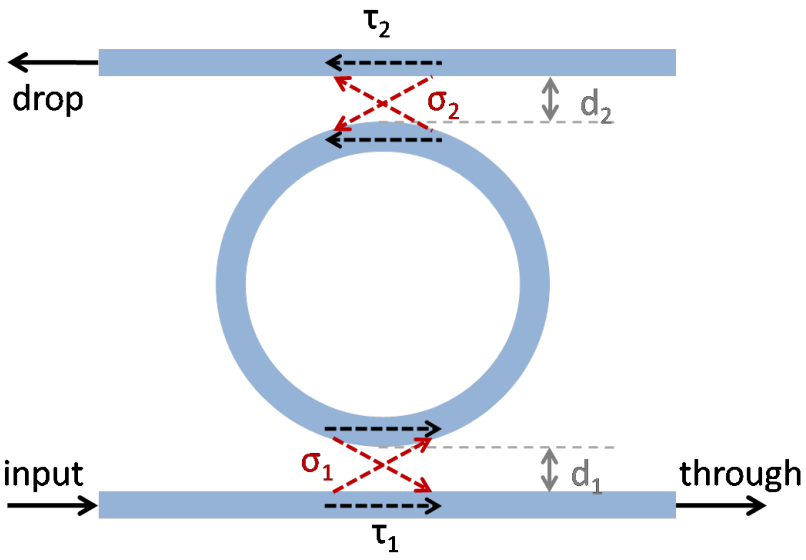

Figure 2.7: Microring in the add-drop configuration. The light injected in the input port can exit from the drop port (resonant with the ring) or from the through port (out-of-resonance). In the case of low attenuation, the critical coupling condition is that of balanced cross-coupling: $\sigma_1 = \sigma_2$.

of the decay rate of energy stored inside the resonator. In fact, contribution to losses are given by propagation losses along the round-trip and by coupling losses from the directional couplers. Thus, the reason for add-drops having an intrinsically lower Q factor is due to the fact that there are two side couplers per round-trip instead of just one. Indeed, the Q factor for add-drops resonators depends on the round-trip length, as represented by the dashed lines in Fig. 2.6 from [39]. The highest Q factor achievable from a ring in the add-drop configuration, assuming propagation losses of 2.7 dB/cm, is on the order of 1.36 $\times 10^4$ that, as in the case of the all-pass rings, represents an upper limit, while values obtained experimentally are lower, typically below 10^4 [117, 118].

2.2.3 Applications of microring resonators

Thanks to their simple geometry and behaviour, microring resonators are suitable for a variety of applications, ranging from spectral filtering, to energy storage, passing through optical sensing and multiplexing. An overview of some of the most important applications will be given just below. In the next section we will focus instead on the possibility to use them, thanks to the enhancement of nonlinear processes, as sources of correlated photon pairs.

Sensing and biosensing

The transmission spectrum of microrings is very sensitive to changes in the environment, which can reflect in changes of the refractive index of the core, where the field is confined, or of the cladding, where it extends. Applications of thermal tuning, based on thermo-optic effect, or of mechanical solicitations, have been reported [39]. However, perhaps the most appealing applications are based on the microrings capability of selectively detect compounds. This can be achieved by amplifying the response of the ring to a specific element thanks to a chemical modification and functionalization of its surface. They are very appealing in particular in the field of biosensing, where there is a strong demand of devices capable to specifically detect biological analytes in a solution. The development of biosensors is challenging for different reasons: particles to be detected are usually sized few nanometers, have very small concentration, and the solution typically contains many other substances at higher concentration. Microrings can easily have a large quality factor, large extinction and low insertion loss, that could enhance the sensitivity of a sensing device. On the other hand, their compactness gives the possibility of incorporating many of them on a single chip in order to perform simultaneous measurements [119, 120, 121]. The recent realization of microring resonators made of porous silicon with a record Q-factor [122] allowed to combine the good sensing properties of a material like porous silicon, with the enhancement of resonating structures. For more details on this, we refer on the work reported in chapter 3.

Filters and demultiplexers

Also spectral filtering, strongly requested for applications in the telecommunication field, can be implemented with microring resonators. In fact, microrings in the add-drop configuration have already been proven as optical filters and as multiplexers (MUX) [117]. They are suitable for wavelength division multiplexing (WDM), a technique that promises to increase the information capacity in an optical transmission system by exploiting distinct signals, at different wavelengths, travelling in the same channel. MUX are used to splice the different signals together, while DEMUX split apart the different signal wavelengths at the output of the system. Add-drop filters can be cascaded, for instance using rings with slightly different sizes, in order to realize multi-channel MUX and DEMUX [117, 123]. Ring resonators in the add-drop configuration could also be used as channel filters, however, their sensitivity to environmental changes requires an accurate tuning process in order to set the ring wavelength to the needed value. For more details about the use of add-drops as filters, we refer to our work reported in chapter 4.

Delay lines

Microrings are also suitable for the realization of optical delay lines or buffers in photonic integrated circuits [124, 125]. Close to resonance, they are

characterized by strong dispersion and consequent large group delay: it can be seen as if the optical signal is stored in the resonator before being released. This property, together with the possibility to choose a large bandwidth, makes them suitable for the realization of optical buffers. The delay generated by a single microring resonators is too short for practical applications, but this can be overcome by using cascaded microrings in order to increase group delay [126], reaching time delays on the order of hundreds of picoseconds. For more details on coupled resonators like CROWS we refer to [127].

Modulators

A famous application of microring resonators is that of electro-optic modulators. Generally, when a resonator is used as a modulator, the operating wavelength falls on the slope of the resonance peak and then a modulation of the length (or of the refractive index) leads to a shift of the resonance. In particular, when dealing with ring resonators, one usually uses all-pass filters close to critical coupling condition [40], so that a large modulation depth can be achieved even with a relatively small shift of the resonance frequency. The modulation turns out to be more efficient when the ring has a high Q, because of the steeper slope of the resonance peaks. The modulation of the effective index in the ring could be actuated by temperature changes, but it is not suitable because of relatively large time constants for thermo-optic response, that are on the order of μs. One could instead exploit the dependence of the refractive index of silicon from the concentration of carriers [33, 128].Ring resonators are very appealing for modulation thanks to their compactness and to the possibility to reach high modulation speeds (10-25 GHz) with low power consumption, as also reported by many works in literature [40, 38, 129, 128, 130].

2.3 Nonlinear effects in silicon devices

In this section we will discuss nonlinear optical susceptibility, devoting particular attention to the case of silicon, starting from the generic phenomenon and then analyzing the case of waveguides and microrings. For a more detailed treatment of nonlinear properties of materials we refer to [131, 42, 37].

2.3.1 Third-order nonlinear susceptibility in silicon

The propagation of an electromagnetic field at frequency ω in a generic medium is responsible for a polarization vector $P(\omega)$ that, in the linear regime, is linearly dependent on the electric field, as described by

$$P(\omega) = \varepsilon_0 \chi(\omega) E(\omega) \tag{2.16}$$

where ε_0 is the electric permittivity of vacuum and χ is the electric susceptibility. If one considers a high intensity field, a nonlinear response can arise,

due to polarization of electric charges proportional to higher order powers of the electric field. This behaviour can be interpreted as if photons propagating in the material could interact with each other through the nonlinearity of the medium. As a consequence of an exchange of energy, additional photons at new frequencies can be obtained. Typically, a field on the order of $1kV/cm$ is needed to observe nonlinearities in a bulky medium [131].

The simplest way to describe the polarization induced by an electric field E in the nonlinear regime is:

$$P_i = \varepsilon_0 \left(\sum_j \chi_{ij}^{(1)} E_j + \sum_{jk} \chi_{ijk}^{(2)} E_j E_k + \sum_{jkl} \chi_{ijkl}^{(3)} E_j E_k E_l + ... \right) \tag{2.17}$$

where ε_0 is the vacuum dielectric constant and the tensors $\chi_{ij}^{(1)}$, $\chi_{ijk}^{(2)}$ and $\chi_{ijkl}^{(3)}$ contain the first-, second- and third-order susceptibilities of the medium. The indices i, j, k, l, representing the components along a generic axis, can assume the value 1, 2 or 3, indicating the component respectively along axis x, y and z, and the first three terms of the susceptibility are:

$\chi^{(1)}$ is the linear susceptibility, that gives the behaviour of an harmonic oscillator: the polarization of the medium does not depend from intensity and is directly proportional to electric field.

$\chi^{(2)}$ is the second-order term, which gives a response in the polarization proportional to the square of the electric field. This term happens to be equal to zero in centrosymmetric materials, as in the case of silicon. It is responsible of effects such as parametric down-conversion (PDC), second-harmonic generation (SHG), sum- and difference-frequency generation (SFG and DFG), optical parametric amplification (OPA).

$\chi^{(3)}$ becomes the first relevant nonlinear term in centro-symmetric materials. It is responsible of third-harmonic generation (THG), two-photon absorption (TPA) Kerr effect and four-wave mixing (FWM).

Equation (2.17) is valid with the assumption that the response of the medium is instantaneous. To have an idea of the ratio of magnitudes among a polarization term of order n and one of order $n+1$, a good estimate is given by

$$\left| \frac{P_i^{(n+1)}}{P_i^{(n)}} \right| \approx \left| \frac{E}{E_{at}} \right| \tag{2.18}$$

where the atomic electric field is typically on the order of $E_{at} = 10^{10}$ V/m. Thus, if one considers a field of about $E = 10^5$ V/m, it is evident how the intensity of higher order terms decreases drastically. From a rough estimate, in the expansion of nonlinear polarization, each term is five orders of magnitude weaker than the previous one [43].

Being silicon a centro-symmetric material, it is characterized by a vanishing second-order susceptibility. In fact, due to symmetry, a change in the sign of the electric fields causes a change in the sign of the polarization, and equality $\chi^{(2)}_{ijk}E_jE_k = -\chi^{(2)}_{ijk}(-E_j)(-E_k)$ can be satisfied only if $\chi^{(2)}_{ijk=0}$. Let's then consider a material with a third-order nonlinear susceptibility $\chi^{(3)}$, to which a monochromatic field is applied, that can be expressed in the form $E(t) = E_\omega cos(\omega t)$. The term of the polarization due to the nonlinearity can be expressed as

$$P^{(3)}(t) = \varepsilon_0\chi^{(3)}E^3(t). \tag{2.19}$$

Equation (2.19) can be easily translated into the form

$$P^{(3)}(t) = \frac{1}{4}\varepsilon_0\chi^{(3)}E^3_\omega cos(3\omega t) + \frac{3}{4}\varepsilon_0\chi^{(3)}E^3_\omega cos(\omega t), \tag{2.20}$$

where the right side of equation is composed by two terms. The first one is bound to the process of third harmonic generation (THG), where three photons from the incident beam at frequency ω are converted into a photon at frequency 3ω. The last term, describes a nonlinear contribution to the polarization that oscillates at the same frequency as the input optical beam ω, and is responsible for a nonlinear contribution to the refractive index experienced by a wave at frequency ω. The refractive index in such a material, in the presence of a field of intensity I, is given by

$$n = n_0 + n_2 I \tag{2.21}$$

where n_0 is the linear refractive index (the one that is commonly considered in linear optics) while n_2, is the nonlinear refractive index, usually referred to as the Kerr coefficient. Equation (2.21) describes Kerr effect, which consists of the dependence of the refractive index from the intensity of the incoming field. The relation between n_2 and the third-order susceptibility is given by:

$$n_2 = \frac{3}{2\varepsilon_0 n_0^2 c}\chi^{(3)}, \tag{2.22}$$

which sets an explicit dependence of n_2 from the nonlinear susceptibility [45]. If we consider the complex dielectric function $\varepsilon(\omega) = \varepsilon' + i\varepsilon''$, the n_2 coefficient is bound to the real dispersive part, while the imaginary part is due to nonlinear losses, represented by two-photon absorption (TPA).

In fact, the third-order nonlinear susceptibility in silicon is mainly due to bound electrons and optical phonons. TPA is typically an undesired effect, that consists in the formation of free electron and hole consequently to the absorption of a couple of photons at energy higher than $E_g/2$, that in silicon corresponds to wavelengths below 1.1 μm [132]. Obviously, being silicon an indirect bandgap semiconductor, TPA is a phonon-assisted process. A consequence of TPA is that electrons which have been promoted to the conduction band are responsible for free-carrier absorption, leading to further changes in the refractive index and susceptibility.

While the second-order nonlinear susceptibility of silicon is vanishing due to symmetry, its third-order nonlinearity is considerably high with respect to other materials. For instance, silicon shows a Kerr coefficient at telecom wavelength more than two orders of magnitude higher than silica glass [132]. This allows to observe interactions among photons with relatively low power, making silicon waveguides intensively studied for phenomena based on third-order susceptibility, as self phase modulation, cross phase modulation, stimulated Raman scattering and four-wave mixing. However, nonlinear refractive index for third-order nonlinear materials is typically on the order of $n_2 = 10^{-14} cm^2/W$ [133, 131], as in the case of silicon. This very low value is the reason for which strategies of field confinement must be adopted to enhance the interaction between the field and the material, in order to observe nonlinear effects.

Four-Wave Mixing

If we look back at equation (2.17), we can see that nonlinearity can couple fields with different amplitudes and frequencies. If we focus on the third term, that we report here for convenience

$$P_i^{(3)} = \varepsilon_0 \sum_{jkl} \chi_{ijkl}^{(3)} E_j E_k E_l, \tag{2.23}$$

we can see that it involves four fields, which can be in principle at different frequencies. Here, we will always refer to the particular case of degenerate four-wave mixing (DFWM), where the frequencies of two of the incoming fields are the same, and a component of the polarization oscillates at frequency $2\omega_2 - \omega_3$:

$$P(2\omega_2 - \omega_3) \propto \chi^{(3)} E_{\omega 2}^2 E_{\omega 3}. \tag{2.24}$$

Two incoming fields at frequency ω_p, usually called pump, are converted in two fields, namely *signal* and *idler*, at frequencies ω_s and ω_i respectively. The constraints of conservation of energy and momentum must always be satisfied, as described by equations:

$$2\omega_p = \omega_s + \omega_i \tag{2.25}$$

$$2\mathbf{k_p} = \mathbf{k_s} + \mathbf{k_i}. \tag{2.26}$$

At this point we believe that a disambiguation is necessary, in fact in literature the definition of *degenerate* FWM can be not univocal. For instance, Shen refers to degenerate FWM when all the four waves have the same frequency [42]. Another possibility, as reported in [34], is the case in which the generated photons are degenerate, that can be obtained from two input fields with different energies. One recent example of this is reported in [134], where microrings were used to generate frequency-degenerate photon pairs, useful for quantum metrology and quantum state engineering. We thus intend to precise here that from now on, with degenerate FWM we will always refer to the case of the mixing between two incoming waves at the same frequency.

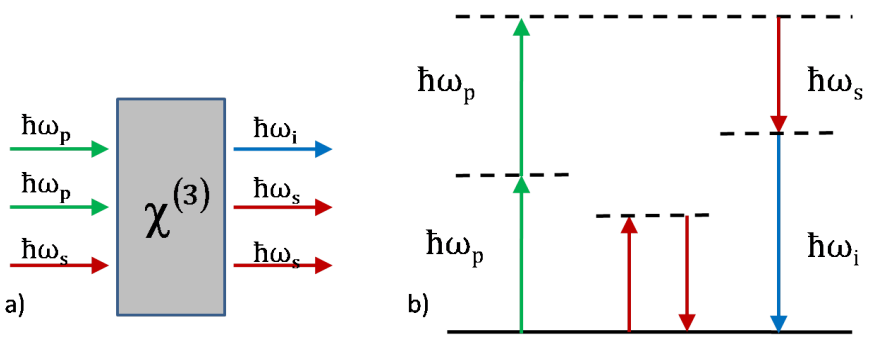

Figure 2.8: a) Schematic picture of the stimulated FWM. Two pump photons at energy $\hbar\omega_p$ are input in the nonlinear medium, together with a signal photon at energy $\hbar\omega_p$, that is not directly involved in the transition and is found again in the output. The pump photons are converted in the signal and idler outgoing photons at energies $\hbar\omega_s$ and $\hbar\omega_i$ respectively. b) Level diagram of stimulated FWM, where up-going arrows are incoming fields, down-going arrows are outgoing fields and the dashed lines represent virtual levels.

It is also important to specify here that FWM is a parametric process, meaning that the quantum state of the material does not change during the interaction. In other words, there is not exchange of energy, momentum or angular momentum between the electromagnetic field and the material. The transition involves only virtual levels, and is considered as an instantaneous process, with a typical time of few femtoseconds [43].

FWM can be either a classical or a quantum phenomenon, depending on the properties of incoming fields. The classical case is that of stimulated FWM, in which the transition is stimulated by a further incoming signal field, which does not take part actively in the process, as represented in Fig. 2.8. On the other hand, spontaneous four-wave mixing (SFWM) is the quantum effect, where only a bright pump field at frequency ω_p is injected in the medium, and the transitions are initiated by the vacuum fluctuations [42]. Both spontaneous and stimulated processes will be analysed more in detail in section 2.3.3 about FWM in microring resonators.

2.3.2 FWM in integrated waveguides

Let's consider now the process of stimulated FWM in integrated waveguides. A pump wave of frequency ω_p and a signal wave at a different frequency ω_s are injected in the silicon waveguide. Because of the $\chi^{(3)}$ term of the material, if the phase matching condition is fulfilled, a new wave called idler is generated at frequency $\omega_i = 2\omega_p - \omega_s$, satisfying the conservation of energy as reported in equation (2.25). Generally, frequency-conversion processes like

FMW require the ratio between the fields to be

$$|E_P| >> |E_S| >> |E_I| \tag{2.27}$$

that allows us to neglect the depletion of the pump and other nonlinear effects like self-phase modulation (SPM) or cross-phase modulation (XPM) that could be induced. The fields propagating into the waveguide in the z-direction can be described by equations [42, 135]:

$$\frac{\partial A_P(z)}{\partial z} = \left(i\beta_P - \frac{\alpha_P}{2}\right) A_P(z) \tag{2.28}$$

$$\frac{\partial A_S(z)}{\partial z} = \left(i\beta_S - \frac{\alpha_S}{2}\right) A_S(z) + \gamma A_P^2(z) A_I^*(z) \tag{2.29}$$

$$\frac{\partial A_I(z)}{\partial z} = \left(i\beta_I - \frac{\alpha_I}{2}\right) A_I(z) + \gamma A_P^2(z) A_S^*(z) \tag{2.30}$$

where A_P, A_S and A_I are the field amplitudes for pump, signal and idler respectively. The β coefficients are the longitudinal propagation constants for the waveguide mode at each frequency, while α are the propagation loss coefficients. The last component on the right side of equations (2.29) and (2.30) is due to FWM and allows us to introduce the coefficient γ, that is the waveguide nonlinear parameter: this quantity can give an estimate of the strength of the interaction between pump and signal fields to generate idler field A_I.

From the equations of the field it is also possible to find the phase mismatch between the interacting waves:

$$\Delta k = 2k_p - k_i - k_s. \tag{2.31}$$

We shall notice that the conservation of energy constraint implies that two pump photons are absorbed while a signal and idler pair is created: this means that the input signal field is exploited only to initiate the transition but is not involved in the transition. Together with considering undepleted pump approximation, we are also neglecting Raman scattering effects, thus excluding the phonon contribution to third-order nonlinearity, and neglecting the effects of generated free-carriers on the FWM process. This assumption can be considered valid as far as we are considering continuous-wave interactions in intrinsic silicon [136].

2.3.3 Stimulated FWM in silicon microrings

Silicon nano-waveguides can achieve tight light confinement thanks to the high refractive of silicon and a typical cross-sectional area of about 0.1 μm^2. Furthermore, as put in evidence from the nonlinear refractive indices reported in table 2.1 [137], nonlinearity of silicon is much greater than that of silica, so nonlinear optical effects happen more often than in optical fibers.

Material	n_2 at 1550 nm [cm^2/W]	Ref.
Si	4.5×10^{-14}	[138]
SiO_2	1.54×10^{-16}	[139]

Table 2.1: Nonlinear refractive indices for silicon and silica.

Thanks to their capability to trap light, microrings can provide a further enhancement of radiation-matter interaction at resonance. The equally spaced resonances of a microring make it an object perfectly suitable to exploit parametric effects, since their spatial geometry and equally spaced resonances allow to automatically satisfy the conservation of momentum and energy at resonance.

The first theoretical and experimental work about four-wave mixing in a semiconductor microring resonators has been reported by Absil et al. in 2000, for a GaAs/AlGaAs waveguide [140], and was repeated in 2008 in silicon microrings in SOI platform [46]. In this experiment, a CW laser is used to inject an intense pump field at frequency ω_p and power P_p, together with a much weaker signal at frequency ω_s and power P_s into the waveguide. Following the procedure in [140], one can solve the coupled-wave equations (2.28), (2.29) and (2.30) using the relations for the waveguide-ring coupler section, getting the power of the generated idler:

$$P_i = (\gamma L)^2 |F(k)|^8 P_s P_p^2 \tag{2.32}$$

where γ is the waveguide nonlinear parameter and and $F(k)$ is the field enhancement. Assuming that it is the same for pump, signal and idler, it can be expressed as

$$F(k) = \left| \frac{\sigma}{1 - \tau a e^{ikL}} \right| \tag{2.33}$$

that is strictly dependent on the coupling conditions, and whose maximum value is given by the on-resonance field enhancement F_0, for $k = k_0$, while τ and σ are the transmission coefficient along the waveguide and the cross-coupling coefficient from the waveguide to the microring respectively, as defined in section 2.2. This means that, in practice, in order to achieve the maximum enhancement, pump and signal frequencies must be tuned with the microring resonances. In this case, thanks to the equally spaced resonances, the idler field generated at frequency $\omega_i = 2\omega_p - \omega_s$, satisfying the conservation of energy, will arise in correspondence of another resonance of the microring.

A useful relation allows to compare the performance of a ring and a straight waveguide:

$$\frac{P_{i,ring}}{P_{i,wg}} = \left(\frac{L_{ring}}{L_{wg}} \right)^2 F_0^8 \tag{2.34}$$

where the ratio between the idler power generated in a ring and a waveguide goes with the eighth power of the field enhancement! This represents

indeed a dramatic increase in the generation efficiency that can be achieved at resonance. It can also be demonstrated [140] that the field enhancement at resonance, at critical coupling condition, can be written as:

$$F_0 = \left| \frac{\sigma}{1-\tau^2} \right| = \frac{1}{\sigma} = \sqrt{\frac{2Q}{k_0 L}} \tag{2.35}$$

which is valid in the very ideal case of $\sigma \ll 1$, i.e. neglecting every kind of propagation loss from the waveguides. By substituting equation (2.35) into (2.32) one finds a fundamental relation that allows to predict the generated idler power as a function of signal and pump power, which is valid in the limit of undepleted pump [141]:

$$P_i^{ST} = (\gamma 2\pi R)^2 \left(\frac{Q v_g}{\omega_p \pi R} \right)^4 P_s P_p^2. \tag{2.36}$$

Equation (2.36) shows how the generation efficiency can be predicted from the microring parameters: in fact, R is the radius of the ring, Q is the quality factor of the resonances, v_g is the group velocity, ω_p is the pump frequency, γ is the waveguide nonlinear parameter introduced in equations (2.29), (2.30). The Q factor and the frequency of the involved resonances are assumed to be similar, thus equation (2.36) is valid with the assumption that $Q_p \sim Q_s \sim Q_i$ and $\omega_p \sim \omega_s \sim \omega_i$. Indeed, some useful trends can be extracted from (2.36): P_i scales quadratically with P_p and linearly with P_s, and conversion efficiency scales as Q^4/R^2.

We can express parameter γ in a form that will result more useful later:

$$\gamma = \frac{\omega_p n_2}{c A_{eff}} \tag{2.37}$$

where n_2 is the nonlinear refractive index, A_{eff} is the effective area of the waveguide and c is the speed of light. With the assumption that group velocity dispersion is negligible, the group velocity can be expressed as $v_g = \text{FSR} \cdot 2\pi R$. Thus, equation (2.36) can be further manipulated to the form:

$$\gamma = \left(\frac{2\pi R c}{\lambda_p v_g} \right)^2 \frac{\pi}{2RQ_p\sqrt{Q_i Q_s}} \frac{1}{P_p} \sqrt{\frac{P_i}{P_s}} \tag{2.38}$$

where the non-linear parameter γ is expressed as a function of P_p, P_s and P_i through the parameters of the resonances and of the microring.

2.3.4 Spontaneous FWM in microring resonators

In the classical stimulated FWM a pump and a signal laser are needed, even if the signal photon is not required for the conservation of energy in the process, since, as already noticed, it does not contribute to the energy exchange. When the initial number of signal and idler photons is zero, the process of FWM

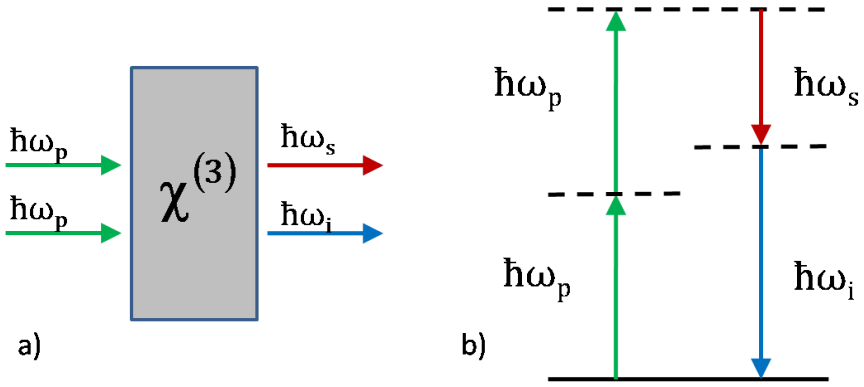

Figure 2.9: a) Schematic picture of spontaneous FWM in a χ^3 material, where two pump photons at energy ω_p are converted into a signal and idler photon at energy ω_s and ω_i. b) Energetic diagram of spontaneous FWM process, from which is evident the conservation of energy. As in the case of Fig. 2.8, dashed lines are representing virtual levels.

can be initiated by vacuum fluctuations. This is the case for spontaneous four wave mixing (SFWM), also called parametric fluorescence, which is particular interesting for the generation of correlated photon pairs. Being a quantum phenomenon, it can't be approached classically, and a rigorous treatment goes beyond the purposes of this thesis, while we refer to [42] for more details. From a simpler point of view, this process can be seen as a four particle elastic scattering in which two pump photons annihilate, producing a signal and a idler photon, as shown in Fig. 2.9.

SFWM in silicon microrings was first reported by Clemmen [47]. Helt et al. in 2010 carried out a theoretical analysis of SFWM in microrings, to which we refer for a rigorous treatment [50]: in this work, starting from the third-order hamiltonian describing the process, the spontaneous emission rate in the undepleted pump approximation is predicted. Without entering in the details of the calculations, we report the main results.

Since idler and signal in SFWM are symmetric with respect to the pump, the on-resonance process will involve a pump resonance N_p, and two resonances N and $\bar{N}$ satisfying $\bar{N} = 2N_p - N$. A practical requirement is that the mode profile and group velocities of the modes must have little variations in the frequency range of interest, that is much easier to be fulfilled if one considers modes N that are very close to the mode of the pump N_p. If this is satisfied, one can fairly assume that $\omega_p \sim \omega_i \sim \omega_s$ holds. Given the stimulated effect, with input pump at resonance N_p and signal at resonance N the generated pump idler can be expressed as

$$P_{\bar{N}} = (\gamma P_{N_p} L)^2 |F_N|^2 |F_{\bar{N}}|^2 |F_{N_p}|^4 P_N \tag{2.39}$$

which is in well agreement with (2.36), and is valid in the limit of no loss

and weak coupling. Considering the same field enhancement F_0 for all the resonances, which can be considered consistent with the previous assumptions, equation (2.39) can be rewritten as:

$$P_{\bar{N}} = (\gamma P_{N_p} L)^2 |F_0|^8 P_N. \tag{2.40}$$

From theoretical calculations [50], the generated power for a resonance of order N (or $\bar{N}$) in the spontaneous process turns out to be:

$$P_N = (\gamma P_{N_P} L)^2 |F_0|^6 \hbar\omega_0 v/(2L) \tag{2.41}$$

where F_0 is the on-resonance field enhancement, as defined in equation (2.35). Comparing equation (2.41) with (2.40) one can identify the factor

$$\frac{\hbar\omega_0 v}{2L|F_0|^2} \tag{2.42}$$

as the quantum analogous of the stimulating power in the spontaneous case, i.e., the power associated to vacuum fluctuations that are initiating the process. Spontaneous generation rate can be easily compared with the stimulated generation rate if we rewrite it in the following form:

$$P_i^{SP} = (\gamma 2\pi R)^2 \left(\frac{2Q}{k_\mu 2\pi R}\right)^3 \frac{\hbar\omega_s v_g}{4\pi R} P_p^2. \tag{2.43}$$

In fact, from the ratio between (2.36) and (2.43) one finds:

$$\frac{P_i^{SP}}{P_i^{ST}} = \frac{1}{4Q}\frac{\hbar\omega_p^2}{P_s} \tag{2.44}$$

which turns out to be independent from the size of the ring, while depends on the Q factors, the signal power and the power $\hbar\omega_p^2$ that, in the range of telecommunication wavelengths is about 160 μW [41].

In the cited experimental work on silicon microrings by Azzini et al., it has been successfully demonstrated that the generation rate in microring resonators is proportional to $Q^3 P_P^2/r^2$, where Q is the quality factor of the resonances, P_P the pump power and r the radius of the ring [41]. It was also experimentally proved that the generated photons are correlated [142] and, more recently, that they can be entangled in energy-time [49]. Time-energy entanglement is extremely appealing for QIP, since it can be easily manipulated in integrated devices and is more robust against loss of information over long distance communication with respect to polarization entanglement. In fact, one of the main drawbacks in polarization encoding consists in the decoherence bound to the transmission of quantum information over long distances along optical fibers. A typical cause is accidental birefringence in optical fibers, that can be due to slight asymmetries in the cross-section of the core or to mechanical stress. As a consequence, states with different polarization

can propagate with different phase velocities, leading to a change in the total polarization state and to loss of information [143, 144]. Birefringence in optical fibers can also lead to polarization mode dispersion, causing photons with different polarizations to propagate with different group velocities inside the fiber [145]. It has to be noticed that, even if polarization is probably not the best tool to encode qubits to be transmitted through optical fibers, this is not necessarily true for every medium: in fact, polarization entanglement has been demonstrated over a distance of 144 km of free-space links [146].

Chapter 3

Four-Wave Mixing in Porous Silicon Microrings

The main subject of this thesis is the generation of photon pairs exploiting nonlinear processes in integrated silicon microring resonators. However, while the enhancement of FWM in silicon microrings is quite a well established and thoroughly studied process, it has never been observed in porous-silicon-based integrated structures. In the last decades, porous silicon gained a lot of importance due to its applicability to disparate fields, ranging from the development of photovoltaic devices [147, 148] to optical and electrical sensing [149], including biosensing [150], label-free biosensing [151, 152, 122] and vapour sensing [153, 154, 155]. However, one of the reasons for which porous silicon has drawn so much attention is to be found in its emission properties [156]. In fact, porous silicon based structures have been reported to have a strong photoluminescence emission, covering a broad energy range from the near infrared, through the visible region, and into the near UV [157, 158]. Light emission from porous silicon has been studied theoretically and experimentally [159, 160, 161], in some cases also induced by an external current [162]. Emission from porous silicon can also be due to its pronounced Raman effect [163], whose correlation to photoluminescence has been explored [164, 165]. However, photoluminescence emission from porous silicon in the near infrared is still not completely understood, and one of the most accredited explanations involves mid-gap dangling bond states on the surface of the material [166, 167].

Another reason that makes porous silicon so appealing consists in its fabrication process: in fact, planar structures having areas of few cm^2 and tens of layers can be produced fairly inexpensively by electrochemical etching [166, 168]. This fabrication technique, as will be described in section 3.1, allows to produce a multilayered material where the refractive index of each layer depends on its porosity, that is the volume fraction of air, which can be controlled by changing the parameters in the fabrication process. Consequently, lateral patterning of PSi films can be performed with electron-beam lithography or direct imprinting [169, 170], in order to obtain integrated structures,

analogously to the fabrication process of SOI based photonic devices.

PSi is characterized by a third-order nonlinear response which has been investigated for years, mainly in multilayered structures [171, 172]. Recently, from nonlinear studies on slab waveguides fabricated by selective oxidation of PSi slabs, it was found that the third-order nonlinear coefficient of PSi is intermediate between the values observed in semiconductors and those measured in oxides, even when the air fraction of the material reaches 70% [173]. It should be noticed that, despite such high nonlinearity, these experiments have required very intense pump powers. Light confinement in micro-resonators played a crucial role in the reduction of power needed to observe nonlinear optical effects in silicon integrated devices, allowing for the observation of these phenomena even under continuous-wave (cw) excitations. The recent demonstration of PSi integrated microring resonators with high quality factors, on the order of 10^4 [122], suggested that the measurement of low-power nonlinear effects could be achieved also in PSi mirostructures. Such a result could open to new and unexplored capabilities, given the flexibility of the physical properties of PSi, even considering that its large internal surface area would allow the incorporation and infiltration with other species.

In this chapter we will describe the measurement of nonlinear optical properties in porous silicon integrated structures, that have been realized with the same fabrication method reported in [122]. First we will describe the fabrication process of porous silicon samples, and in particular focusing on the etching process to obtain the porous slab waveguide. Then, we will report the result of optical characterization of integrated PSi microrings, through the measurement of transmission spectra that allowed us to evaluate the quality of the resonators and losses. We will report about the four-wave mixing measurements that have been performed on microrings, whose results will be discussed and used to determine the nonlinear optical properties of the material under study. The results will be discussed, together with the derivation of the waveguide nonlinear parameters that have been extracted from the FWM measurements.

3.1 Fabrication of porous silicon

The fabrication of the sample consists of two steps. First, a PSi asymmetric slab waveguide is realized by means of electrochemical etching in an hydrofluoric acid (HF) solution. This part of the process is relatively cheap and easy to carry out even in a basic chemistry laboratory. Then, the ridge waveguides and microrings can be patterned on the top layer by means of electron beam lithography (EBL) and reactive ion etching (RIE). The fabrication of the PSi slab waveguides used in this thesis was carried out at Electrical Engineering and Computer Science at Vanderbilt University (Tennessee, USA), while EBL and RIE were performed at the Center for Nanophase Material Sciences at Oak Ridge National Laboratories (Tennesse, USA).

3.1.1 Etching process

The fabrication process of PSi waveguides is particularly flexible, in fact thickness and porosity of each layer can be tailored by properly choosing the current density and etching time [168]. During the process, a p-type boron-doped silicon wafer (0.01 Ω/cm) with a surface of few cm^2, is submerged in an electrochemical cell with an HF (hydrofluoric acid) solution. Given the high danger associated with this kind of acid, most of the fabrication process has to be performed inside a fumehood and with adequate protections. When a constant voltage is applied to the electrodes of the etching cell, a dissolution process takes place, described by the following reaction [168]:

$$\mathrm{Si} + 4\mathrm{HF} + 2\mathrm{F}^- + 2\mathrm{h}^+ \rightarrow \mathrm{SiF}_6^{2-} + \mathrm{H}_2 + 2\mathrm{H}^+ \tag{3.1}$$

where the carriers responsible for the erosion of the silicon are the fluorine ions F^- and the positive charge carriers of silicon h^+. When a hole h^+, driven by the electric field, reaches the surface, a F^- ion can replace a hydrogen atom bonded to Si. When all the four bonds of silicon have been broken, a silicon atom is released from the crystal structure, leaving a small defect (tip) on the surface [168]. The pore preferentially grows in correspondence of this small tip, because of the local concentration of electric field. Then the dissolution tends to follow the direction of the applied electric field (vertical), while it is inhibited in the Silicon region between pores (horizontal) because it is depleted of holes h^+. The result of the process is a columnar porous structure, with pores with diameter of few tens of nm, that are perpendicular to the surface of the sample, as clearly visible in the SEM image of the cross-section of the sample shown in Fig. 3.4 (a). The analysis of the fabrication of porous silicon goes beyond the purposes of this thesis, however, for further studies on the mechanism of pore formation we refer to [174, 175, 158].

3.1.2 Fabrication of the sample

Fabrication of porous silicon waveguide

The assembled etch cell during the realization on a PSi waveguide is shown in Fig. 3.1. The lateral and bottom walls of the cell are made of Teflon, that it is a material chemically resistant to HF. The anode is constituted by the silicon wafer itself, placed on top of an aluminium plate to which the negative potential is applied, while the cathode consists of a spiral-shaped platinum wire, visible in Fig. 3.1, which is resistant to HF. The shape of the cathode is important since it must provide an almost uniform electric field, allowing at the same time that the hydrogen generated in the dissolution can escape from the cell. An O-ring is used to seal the silicon sample between the various components of the cell, which is finally locked with a stainless steel cylinder and screws. The cell is then filled with a solution of hydrofluoric acid (HF) in ethanol with a volume concentration of 15%, so that he sample and

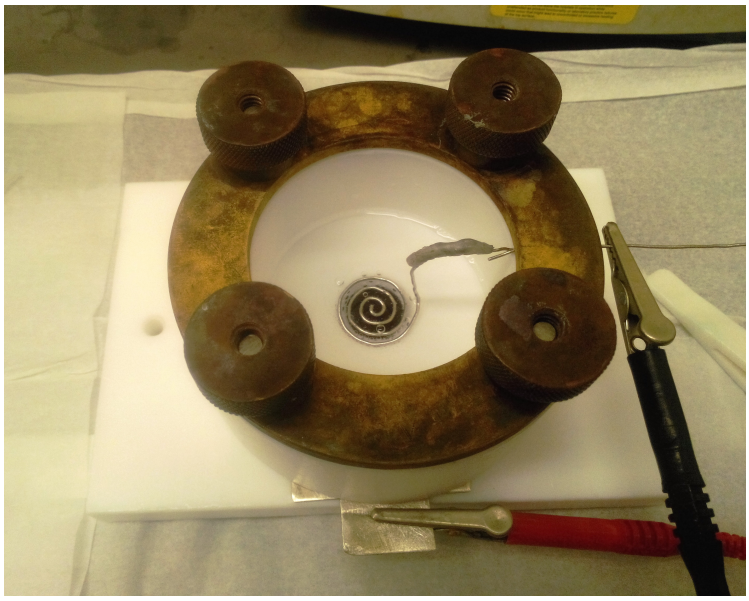

Figure 3.1: Photo of the assembled etch cell. The cell is made of Teflon and is secured with stainless steel cylinder and screws. The silicon wafer is visible from the hole in the bottom of the cell, fully covered by the HF solution. Just above the wafer, sealed with an O-ring, the platinum spiral-shaped cathode is also covered by acid solution, and is connected to the black wire that provides negative voltage. The anode is the silicon wafer, that is placed above an aluminum plate to which positive voltage is applied by the red wire. The wafer and the cathode are then fully covered by the HF solution.

the platinum spiral above it are fully covered by the solution. Finally, the wires are connected to a current supplier (Keithley 2400S) and the voltage is applied to the electrodes. The etching current and time are properly adjusted to obtain porous silicon layers of the desired thickness and porosity. The generator is driven by a computer, where a dedicated Labview software allows to set the parameters (current and time) for each layer, and the growth is controlled by the software. During the etching, the formation of the pores leads to fluctuations in the resistance of the wafer, thus the generator must be stabilized to supply a constant current to the system. In order to monitor the current, the generator sends an output to the dedicated software, that allows to check if there is any unwanted variation of current density during the etching. After the etching, the wafer is removed by the cell and rinsed in ethanol, dried with nitrogen, and then submerged in a 1.5 mM/l KOH solution in ethanol for pore widening. Finally, the sample undergoes an annealing step at 500°C for 5 minutes, in order to obtain smoother sidewalls of the subsequently realized microstructures [122].

Choice of the etching parameters

The etching parameters used to obtain our sample and the properties of the corresponding layers are reported in table 3.1. A proper choice of the etching parameters was possible thanks to a preliminary analysis on porous silicon monolayers, that allowed us to link thickness, porosity and refractive index of a layer to the current density and etching time.

	current density	etching time	thickness	index
guiding layer	5 mA/cm^2	122 s	0.6 μm	1.79
cladding	48 mA/cm^2	6 s	1.4 μm	1.24

Table 3.1: Etching parameters used for the realization of our sample. Current density and etching time are chosen to obtain a certain layer thickness and effective refractive index.

In the first part of this analysis, the thickness of an etched PSi monolayer is determined from a SEM image of the cross-section of the layer. Then, a measurement of the reflectance spectrum of the layer, resulting in an interference pattern, allows to obtain the refractive index of the layer, as reported in [176].

Bruggeman effective index approximation [177, 178] can be finally adopted to associate porosity with effective refractive index. As shown in Fig. 3.2 (a), an increase in the applied current density leads to higher porosity: values between 45% and 85% can be achieved for current densities between 5 mA/cm^2 and 100 mA/cm^2. The etching rate as a function of current density is reported instead in Fig. 3.2 (b): as can be noticed, the etching time must be set according to the current density. In particular, etching rate ranging from 5 nm/s up

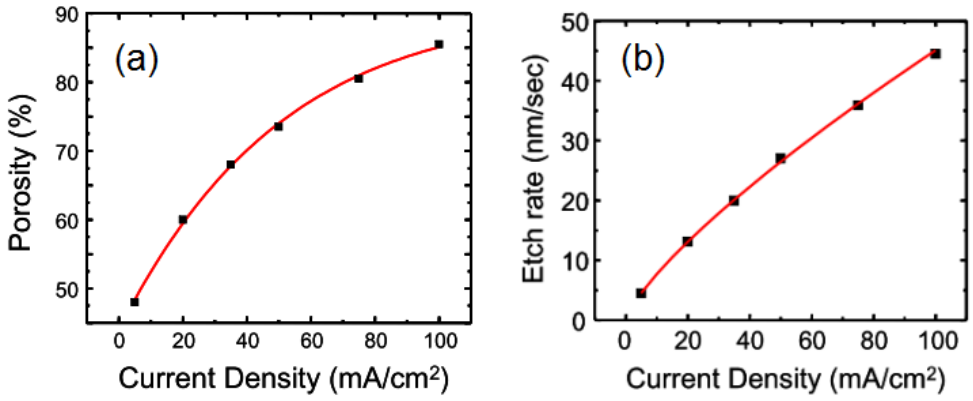

Figure 3.2: (a) Dependence of the porosity from the applied current density. Higher porosity can be obtained increasing current density (b) Etch rate as a function of current density, showing that the speed increases with higher current density. The red lines are the result of a best fit with power laws, whose result can be used to properly choose the etching parameters [176]. Both trends have been experimentally determined on a silicon wafer with p+ doping (0.01 Ω/cm) etched in a 15% solution of HF in ethanol [176].

to 45 nm/s can be achieved with current density varying between 5 mA/cm^2 and 100 mA/cm^2. The trends shown in Fig 3.2 (a) and (b) were originally reported in [176], and allow to properly choose the etching parameters in order to obtained the desired porous silicon layers.

Litography

Once the slab waveguide has been made, the ridge waveguides and rings can be patterned with standard EBL and RIE. In this process, a 300nm-thick film of resist (ZEP520 A) is deposited on the PSi surface. EBL (JEOL JBX-9300-100kV) is used to pattern the design on the resist, followed by a 30 seconds development in xylenes and rinsing. The etching is then performed by means of an RIE tool (Oxford Plasmalab 100) where $C_4F_8/SF_6/Ar$ gases are used to transfer the pattern on the guiding layer. The residual ZEP resist can then be removed with 10 minutes of O_2 plasma cleaning. Finally, a manual cleavage of the sample is necessary in order to reduce the total size of the sample, so that the waveguides are about 2-3 mm long.

3.1.3 Sample Layout

The sample consists of a wafer sized about 10 mm × 3 mm, constituted by an array of straight waveguides which start in one edge of the sample and finish in the opposite edge. A critical aspect is that the length of the waveguide can not be precisely controlled because of the manual cleavage of the

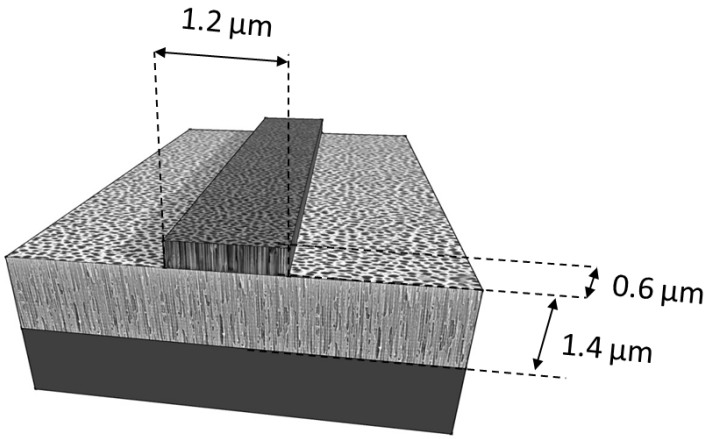

Figure 3.3: Representation of the cross-section of the sample: the channel waveguide, having a width of 1.2 μm, is obtained from the full-depth etching of the guiding layer, characterized by a thickness of 0.6 μm and refractive index of $n_{wg} = 1.79$, while the cladding layer below, with thickness 1.4 μm, has a lower index $n_{clad} = 1.24$.

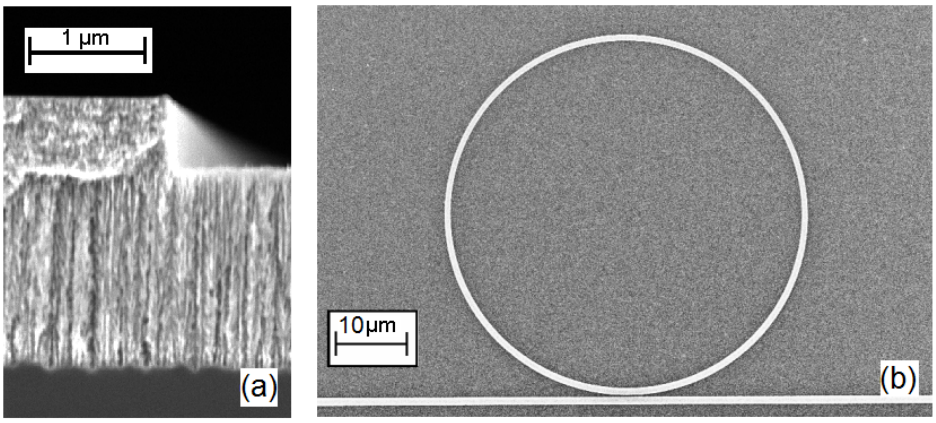

Figure 3.4: (a) SEM image of the cross section of the sample, showing a detail of the side-wall of the waveguide. The vertical porous structure is well visible in the cladding, where the porosity is higher. (b) SEM image of the top view of a detail of the sample, showing the microring with radius of 25 μm coupled to the straight waveguide, with a coupling distance of about 200 nm.

sample, during which it could be also accidentally damaged. However, the sample that we used has an almost uniform width of 3 mm, which coincides with the total length of the waveguide. Ridge waveguide has a width of 1.2 μm and a thickness of 0.6 μm, as shown in Fig. 3.3 (a), where the cross-section is represented: these values were designed to have a waveguide supporting a single mode at the operating wavelength, around 1.5 μm, with TE polarization. The values of the cross-section of the waveguide, as well as the radius of the microring, are larger than the usual values for crystalline silicon, due to the lower refractive index contrast of the considered case. Porous silicon is in general a birefringent material, with the optical axis oriented along the (vertical) growth direction. Working in TE polarization, with the electric field mainly in the plane of the structure, allow us to neglect such anisotropy, for the field effectively experiences an isotropic system.

Calculations performed with effective index method (EIM) showed that the effective index of the mode in the waveguide is $n_{eff} = 1.51$, with the assumption that dispersion in this wavelength range is negligible. During a preliminary characterization on waveguides with different lengths, propagation losses from the channel waveguides were measured to be on the order of 27.5 dB/cm [122].

Each waveguide is coupled to a microring, placed approximately in the middle of the waveguide, with a gap distance of about 200 nm, optimized in order to have critical coupling. This condition can be strongly affected by slight changes in the effective index and by losses from the waveguide and the microring, that can slightly vary from one point to another of the sample. Thus, different replicas of each microring, with gap distances slightly varying around 200 nm were fabricated, in order to ensure that at least one is at critical coupling, even taking into account for this variability. Tha whole sample includes microrings of different sizes, with radii varying between 10 μm and 30 μm.

At both ends, the waveguide is provided with two coupling tapers that are about 500 μm long, along which the maximum width of 20 μm shrinks down to the width of the bus waveguide of 1.2 μm.

3.2 Linear characterization of the sample

To characterize the linear response of the sample, the transmission spectra of microrings with different radii and coupling distances have been measured. We don't report here all the results, however such characterization allowed us to choose for the FWM experiment the microrings with 25 μm radius. In fact, in average they showed the best quality factors, combined with good coupling conditions.

3.2.1 Transmission measurements

To perform transmission measurements, the sample is placed on a support on top of a translating and rotating stage to adjust its position. The in-coupling and out-coupling are provided by means of two polarization maintaining (PM) tapered fibers, that are used to match the mode profile in the waveguide, mounted on 3-axis translators. Tapered fibers are directly aligned to the tapers at opposite ends of the waveguide coupled to the ring to be measured: the rotating and translating stages are thus necessary to align the tapered fibers so that they are centered and parallel to the waveguide.

External polarizers are used to control the polarization: all the measurement are done in TE polarization, since the waveguides and microring are designed to work in this configuration. As a help in the alignmen operation a magnified image of the sample is focused on both a visible and an IR camera, by means of a custom-made microscope mounted above the sample, in a configuration similar to the one described in section 4.2.1.

For a rougher first alignment, the sample is excited with a broadband superluminescent diode laser (Thorlabs SLD 5260) and the transmitted light is analysed by a spectrometer and detected by a liquid-nitrogen-cooled CCD camera with a spectral resolution of 70 pm. To reach higher resolution, up to 1 pm, we used as source a tunable laser (Santec TSL-510) in scanning mode, while the transmitted light was collected by a InGaAs detector (Newport 918D-IG-OD3) and measured with a high sensitivity Power Meter. The spectrum is finally reconstructed with a Labview software.

The result of a transmission spectrum of a microring with radius 25 μm is shown in Fig. 3.5, from which it is possible to determine a free spectral range FSR = 7 nm. In Fig. 3.6 we report a detail of the transmission spectrum of the same microring, with a resolution of 5 pm, where the resonances used as idler, pump and signal in the FWM experiment are highlighted. The solid black line in Fig. 3.6 is the measured transmission, while the dashed red line is the best fit with a lorentzian function. The obtained central wavelengths for idler, pump and signal are $\lambda_i = 1571.60$ nm, $\lambda_p = 1578.58$ nm and $\lambda_s = 1585.57$ nm, with Q factors $Q_i = 5800$, $Q_p = 5900$ and $Q_s = 4200$.

3.2.2 Insertion and propagation losses

From the ratio between input and output power, measured with an InGaAs detector placed right before or after the sample, respectively, we were able to estimate the insertion losses of our sample to be on the order of 30 dB around the interested wavelength range. Propagation losses, that can be attributed to the scattering associated with the material roughness, were measured to be 27.5 dB/cm, as reported in [122]. Considering that the total length of the waveguide is around 3 mm, the propagation losses account at most for 10 dB of attenuation in the worst case, thus the main contribution to losses can be attributed to the poor coupling efficiency between the tapered fiber and the

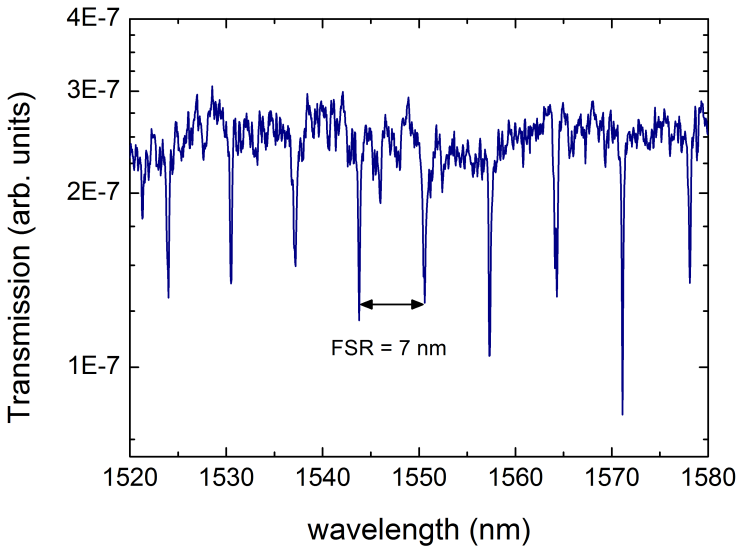

Figure 3.5: Transmission spectrum of the microring with 25 μm radius, measured with the tunable laser in scanning mode. The average free spectral range of 7 nm is put in evidence by the arrow.

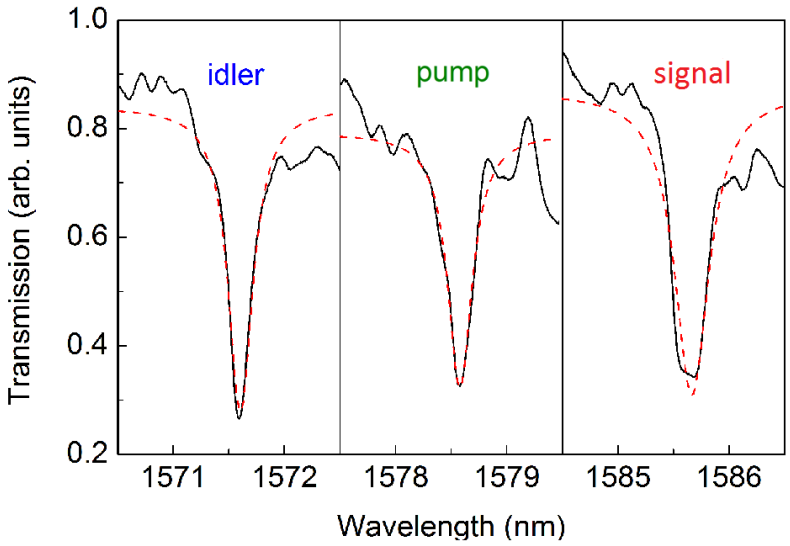

Figure 3.6: Transmission spectrum of the sample showing the resonances used as idler, pump and signal in the FWM experiment. The solid black line is the measured transmission, the dashed red line is the result of a lorentzian fit of the resonances, from which we estimated an average quality factor of $Q \approx 5000$.

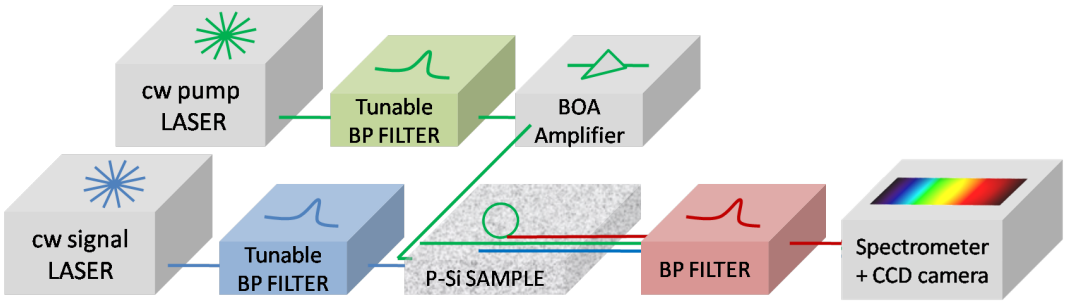

Figure 3.7: Schematic representation of the experimental set-up. The pump laser, tuned at the central wavelength of the dip individuated as pump resonance, is spectrally filtered and amplified with a BOA. The signal laser, tuned at signal resonance, is also spectrally filtered and combined to the pump laser by means of a fiber beam splitter (not shown in the image). One of the outputs of the beam splitter, as better specified in the main text, is connected to the tapered fiber aligned to the input taper of the waveguide. The output, exiting from the taper at the opposite side of the waveguide, is then filtered using a BP filter centered around the idler wavelength, that rejects the intense transmitted signal and pump lasers. The resulting filtered light is then sent to a spectrometer coupled to a CCD camera for detection. The whole set-up is working in TE polarization, with PM fibers.

coupling taper. Such high losses can be due to cross-section mismatch, as well as to reflection and scattering from the rough edge of the sample.

Indeed, propagation losses constitute a limit to the Q factor of the resonator. In fact, knowing the propagation losses α, the intrinsic upper limit for Q at wavelength λ_0 is given by equation (2.12), that we report here for convenience:

$$Q_{int} = \frac{2\pi n}{\lambda_0 \alpha} \tag{3.2}$$

where in our case $\alpha = 6.33$ cm^{-1}, and mode effective index is $n = 1.51$, as obtained from EIM based calculations. When the ring is at critical coupling, the loaded Q is given by $Q = Q_{int}/2$, resulting in a theoretical value of $Q \approx 4800$. The higher values that have been obtained from the transmission spectra of the resonances (up to $Q \approx$6000) can be attributed to a condition of slight undercoupling.

3.3 Four-wave mixing experiment

In the FWM measurement, the sample is excited with a pump and a signal laser tuned at the central wavelengths of the corresponding resonances. To do so, we used an experimental set-up as the one depicted in Fig. 3.7. We

used as sources two tunable cw lasers (Santec TSL-210 and Santec TSL-510) working in the wavelength range of interest, between 1500 nm and 1630 nm. The pump laser is amplified with a polarization maintaining booster optical amplifier (BOA) to increase the available power, necessary because of the high insertion losses of the sample. The lasers are spectrally filtered with two band-pass (BP) filters with bandwidth 8 nm and a side-band attenuation higher than 30 dB, in order to clean out the amplified spontaneous emission. The two lasers are then sent to the input ports of a 90:10 fused silica beam splitter. In particular, in order to optimize the available pump power, the output port transmitting the 90% of the pump and 10% of the signal was sent to the sample, while the other port was sent to a power meter, used to monitor the total power during the measurements. The light that comes out from the sample is filtered with a BP filter with a rejection on the order of 120 dB, to remove the residual pump and signal lasers. The filtered idler is then sent to a spectrometer (Acton Spectra Pro 2500i) and collected by a liquid-nitrogen-cooled CCD camera (Acton InGaAs OMA V). The spectrum is measured in units of counts per second, that can be converted in power thanks to a calibration of the CCD camera with a high sensitivity power meter.

Results

The spectrum resulting from a FWM measurement is shown in Fig. 3.8. The main peak on the left is generated by the stimulated FWM process, and is located at idler wavelength (1571.6 nm), as expected from the constraints of conservation of energy. The weaker peaks on the right are the residual pump and signal, that are almost completely rejected by the filters after the sample.

The integration time of the CCD camera, which is the exposure time to get a spectrum like the one in Fig. 3.8, is 30 seconds. Such a long time was needed because of the weak output power due to the high insertion losses of the sample, and indeed constituted an obstacle to a live optimization of the generated FWM, that made necessary the use of the IR camera, where a magnified image of the microring was projected. In fact, because of the roughness typical of the porous material, a huge amount of light is scattered out of the waveguide and the microring. When the laser is in resonance with the microring, there is "more" light inside the resonator than in the waveguide, resulting in higher scattering losses, as visible in the inset of Fig. 3.8. This allowed us to finely tune wavelength of pump and signal lasers, maximizing the power coupled to the ring, by optimizing the light scattered out of it just by looking at the image of the sample on the infrared camera.

The result shown in Fig. 3.8 was obtained with a pump power of 650 μW and signal power of 60 μW, that allowed to obtain a generated idler of 0.6 pW. All the reported input (output) powers have been estimated in the portion of the bus waveguide right before (after) the ring. To do so, we derived from the square root of the insertion losses, assuming that the input and output efficiencies are the same. In this way, from the measured insertion losses of

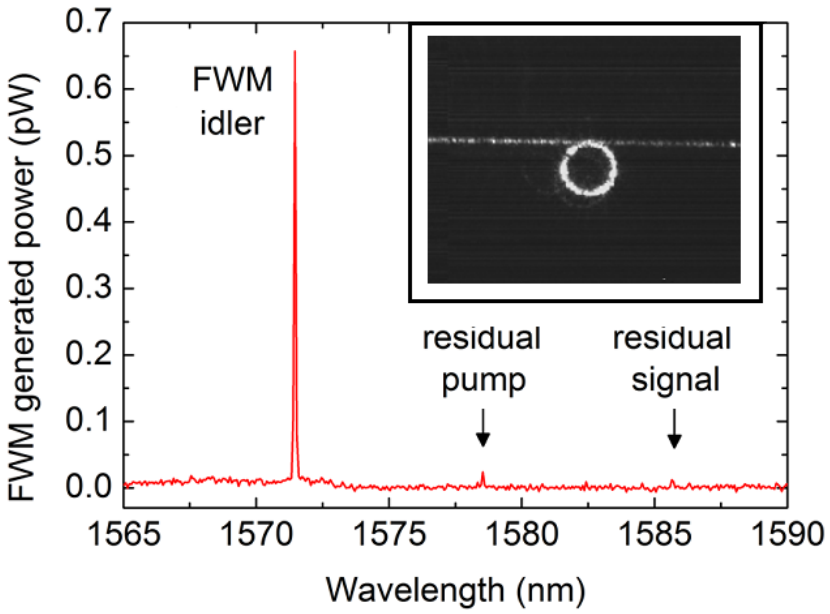

Figure 3.8: Result of FWM measurement with coupled pump power of 650 μW and signal power of 60 μW. The residual pump and signal peaks are visible respectively at 1578.58 nm at 1585.57 nm, while the idler peak arises at 1571.6 nm. Acquisition time is 30 seconds. The photo in the inset, taken with the IR camera, shows a portion of the waveguide coupled to the microring, which is resonantly excited by the pump laser. Bright regions are due to infrared light scattered out from the waveguide, from which is visible that the ring, when resonantly excited, scatters out more light with respect to the waveguide. The dimmer replicas of the ring that might be noticed are ghost images due to multiple reflections from the optical components of the microscope.

30 dB, with a corresponding transmission of 0.1%, we estimated a maximum coupling efficiency of 3.1%. Every reported value of coupled power has an uncertainty that was evaluated to be around 5%.

The output power, even if can seem low with respect to generation of pairs in silicon microring, is remarkable if we consider the high losses and the fact that the ridge waveguide has a fraction of air around 60%. This result was possible thanks to two crucial features of the field inside the microring: the increased effective nonlinearity, due to the light confinement in the ridge waveguide, and the pump field enhancement given by the resonant structure. In fact, even if PSi is characterized by huge surface roughness, the sample studied here is composed by microrings with Q factors sufficiently high to observe FWM at low power.

Dependence from input power

It is well known from literature that the power generated at idler frequency is described by:

$$P_I = (\gamma 2\pi R)^2 \left(\frac{Q v_g}{\omega_P \pi R}\right)^4 P_S P_P^2 \tag{3.3}$$

from which a quadratic dependence from pump power P_P and a linear dependence from signal power P_S are expected. In equation (3.3) R is the radius of the microring, Q is the quality factor of the resonances, ω_P is the pump frequency and v_g is the group velocity. The group velocity is obtained from the relation

$$v_g = \mathrm{FSR} \cdot 2\pi R, \tag{3.4}$$

where we consider as free spectral range (FSR) the mean value of frequency difference between adjacent resonances in the range of interest, determined from the transmission spectrum. Finally, the waveguide nonlinear parameter γ at frequency ω_P for a waveguide with nonlinear refractive index n_2 is given by:

$$\gamma = \frac{\omega_P n_2}{c A_{eff}} \tag{3.5}$$

where c is the speed of light and A_{eff} is the effective area of the waveguide. However, there are many important emission processes in porous silicon, like stimulated Raman scattering or photoluminescence, that might compete with SFWM. To make sure that the emission peak arisig around the wavelength of the resonance at 1571.6 nm, visible in Fig. 3.8, is actually an effect of FWM, one can verify that it follows the trend described by equation (3.3). To do so, we measured the generated idler power as a function of pump power and signal power, with results that are shown in Fig. 3.9.

In particular, in Fig. 3.9(a) signal power is fixed at 60 μW and the dependence of P_I from P_P is shown: each black triangle comes from a single

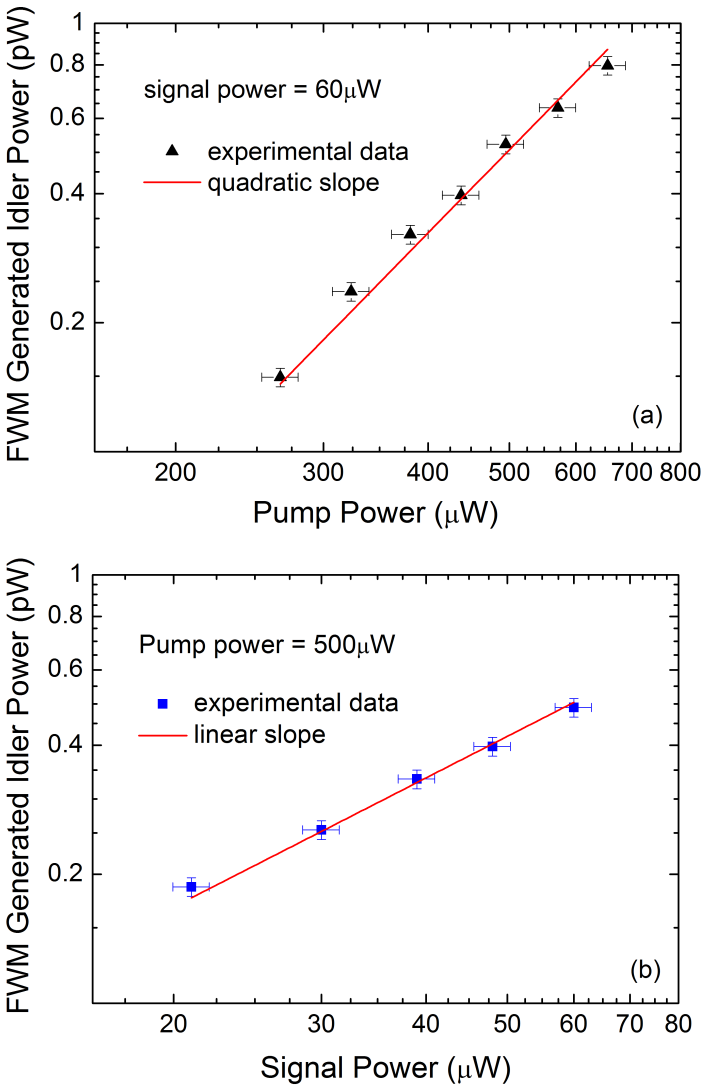

Figure 3.9: (a) Dependence of generated FWM at idler resonance from coupled pump power, with signal power P_S =60 μW, showing a quadratic trend. Black triangles are experimental data, solid red line is the quadratic trend that best fits the data. (b) Generated FWM as a function of signal power, with fixed pump power of P_P =500 μW. In this case, blue squares are experimental data, while solid red line represents the linear trend that best fits the data. These trends can be considered as a clear signature of stimulated FWM.

	γ [$W^{-1}m^{-1}$]
Silicon	200
Chalcogenide glass	93.4
Hydex	0.233

Table 3.2: Values of γ measured in different materials. The value found in Silicon was experimentally determined from FWM in Si [41], as well as for Hydex [179]. The value for arsenic selenide chalcogenide glass was obtained from supercontinuum generation in ChG nanowires [180].

measurement of the total idler power, integrated over the linewidth of the idler resonance, while the solid red line represents a quadratic trend. On the other hand, in Fig. 3.9(b) the dependence of P_I from P_S is shown, where blue squares are experimental data and solid red line represents, in this case, a linear trend.

Indeed, the behaviour that was determined in both cases is in good agreement with the prediction of equation (3.3), where generated idler power scales quadratically with pump power and linearly with signal power. These trends, typical of FWM, have been verified within the error bars: it allowed us to identify the phenomenon that we observe as stimulated FWM, enhanced by the resonant structure of the microring.

3.3.1 Nonlinear parameter γ of PSi waveguides

Each single FWM measurement can be used to calculate the value of the waveguide nonlinear parameter γ, exploiting the following relation:

$$\gamma = \left(\frac{2\pi Rc}{\lambda_P v_g}\right)^2 \frac{\pi}{2RQ_P P_P \sqrt{Q_I Q_S}} \sqrt{\frac{P_I}{P_S}}, \tag{3.6}$$

with group velocity v_g defined in equation 3.4. Applying equation (3.6) to every FWM measurement we calculated the values of γ reported in the graph in Fig. 3.10. Here, black triangles are from the data in Fig. 3.9(a) while blue squares are from Fig. 3.9(b). The dashed red line represents the mean value, that was found to be:

$$\bar{\gamma} = (20 \pm 2) W^{-1}m^{-1}. \tag{3.7}$$

The error bars are obtained from standard propagation of errors and are mainly due to uncertainties in the coupled powers.

With the measured value of γ, the nonlinear refractive index n_2 can be obtained by reversing equation 3.5. To do this, the value of the effective area of the waveguide was calculated as follows [181]

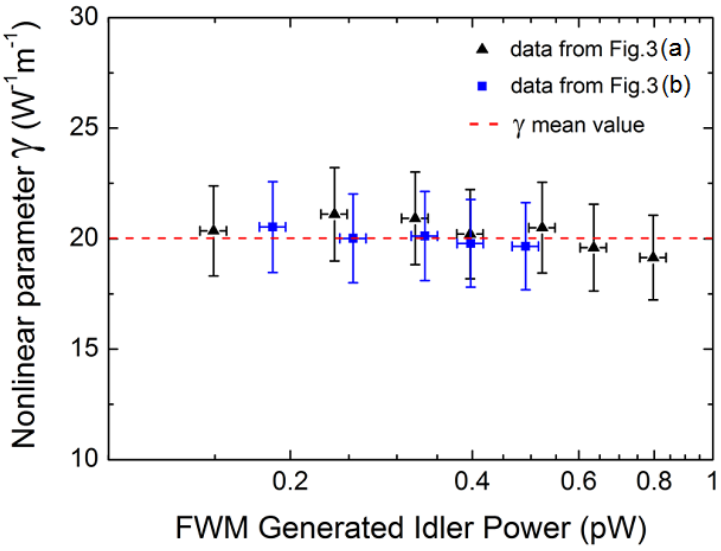

Figure 3.10: The values of γ calculated from equation (3.6) for different values idler power. Black triangles are from measurements reported in Fig. 3.9 (a) while blue dots are from Fig. 3.9 (b). The calculated mean value is $\gamma = (20 \pm 2)\mathrm{W}^{-1}\mathrm{m}^{-1}$, represented by the dashed red line. It was found to have no dependence from signal and idler power within the error bars.

$$A_{eff} = \frac{\left(\int |E|^2 dxdy\right)^2}{\int_{ridge} |E|^4 dxdy}, \tag{3.8}$$

where E is the electric field and x and y are the directions of the axis orthogonal to the propagation direction of the waveguide. The integral in the numerator is carried over the whole space, while the one in the denominator is carried on the ridge cross-section. The value that was found from numerical calculations is $A_{eff} \approx 0.94\mu\mathrm{m}^2$, which turned out to be strongly dependent on the size of the ridge waveguide. Exploiting relation (3.5) we could use this value to calculate the value of the nonlinear refractive index n_2 at pump frequency:

$$n_2 = (4.26 \pm 0.4)10^{-18}\mathrm{m}^2\mathrm{W}^{-1}, \tag{3.9}$$

where we consider as predominant source of error the uncertainty in the coupled power.

This result is consistent with previous works, where pump and probe techniques involving a Ti:Sapphire-pumped OPA were needed. It was possible to determine a nonlinear refractive index of $n_2 = (4.2 \pm 0.8) \cdot 10^{-18}$ m^2/W for PSi waveguides with porosity around 70-80% [173]. Indeed, the breakthrough in our measurement consists in the drastically reduced coupled power: while in

the above mentioned work the power coupled to the waveguide is greater than 10 mW, in our measurement it was less than 1 mW. This was possible thanks to the enhancement of the field due the high quality of the resonator.

Conclusions and perspectives

In this chapter, we reported on the measurement of low-power FWM in porous silicon microring resonators. This experiment allowed us to estimate the nonlinear parameter of the considered waveguides to be $\gamma = 20 \pm 2\ \mathrm{W^{-1}m^{-1}}$, that turned out to be in good agreement with other results previously reported in literature, and to be intermediate between values found in crystalline semiconductors and in oxides. The observation of this effect was non-trivial, since other important emission processes in porous silicon, like stimulated Raman scattering or photoluminescence, could compete with the effect that we intended to study.

We underline that this represents the first case in literature of a measurement of the enhancement of a nonlinear effect with porous silicon integrated resonant structures. To do this, we took advantage on the possibility to realize porous silicon microrings with high Q factors [122], particularly remarkable if we consider the huge intrinsic losses due to the roughness of the material. Furthermore, the fabrication process of porous silicon is low-cost, for porous silicon is cheaper than SOI, and is flexible, allowing to produce layered wafers with well controllable thickness and refractive index. There is a price to pay for the flexibility of the fabrication process of the material, represented by a low reproducibility, that reflects in a practical difficulty to mass-produce photonic circuits based on porous silicon devices. However, the development of novel techniques involving direct imprinting of porous silicon [170, 169] could be a promising strategy towards the possibility to realize a large number of devices with short time, low cost and good reproducibility. Another well known weakness of porous silicon consists of its instability due to oxidation and interaction with the environment, that is a huge obstacle in the use of this material for the realization of complex photonic circuits. However, it could be of crucial importance in the development of disposable devices for sensing application, in particular if one considers that they can be associated with reference objects that can help to overcome the above-mentioned instability.

From another point of view, the porosity of the material is a strategic property if we consider its relevance for sensing applications. In fact, porous silicon has been recently used for selective sensing of differently-sized molecules, and can be functionalised to detect specific substances. In this perspective, the results reported in this chapter could lead to new and unexplored applications, in particular to the measurement of nonlinear properties of liquid materials that could be infiltrated in the porous structure, giving the possibility to enhance and study the nonlinear properties of different materials. Of course, this would require a retroactive optimization of the waveguide parameters, since the effective index of the medium would change with the infiltration. However, given

the novelty of the achieved results, we believe that our work could trigger further exploration of nonlinear effects in porous materials, and that it can be a good starting point for applications of porous silicon integrated devices in nonlinear optics.

Chapter 4

On-chip filtering and routing of correlated photos

As discussed in the previous chapters, silicon microrings are a promising tool for the generation of correlated photons pairs. In this chapter, we illustrate the strategy that we adopted to try to solve some practical issues that are still associated to this kind of source. A major practical problem is the rejection of the laser that is used as pump in the FWM experiments: the bright pump that is injected in the waveguide to excite the system is in fact mostly transmitted. In the case of spontaneous processes the pump can be many orders of magnitude more intense than the generated photons, and the rejection necessary to completely suppress it has been determined to be above 100 dB [41, 34]. Up to now, off-chip filtering requires bulk dichroic filters, preventing an actual integrability of the source. Another practical issue costists of the need to separate the generated signal and idler photons, and route them to different outputs of a device, in order to be available and ready to use. The purpose is to realize the so called *lab-on-a-chip*, where bulky components of the experiment are substituted by integrated devices.

The strategy that we developed to solve this issue is based on SOI-based hybrid photonic-electrical circuits with components that can be thermally tuned. This chapter will start with a description of the sample and its fabrication process. After reporting the characterization of the sample, we will describe the experiment which can be divided in two parts. The first part consists of the spontaneous FWM from microring resonators, with full rejection of the pump achieved on a single chip. The second part is the *chip-to-chip* experiment, where correlated photons generated in one chip are spectrally filtered and transferred to a second receiver chip, where they are separated and output. We will finally report on the time-correlation measurements performed on the photons coming out of the second chip.

4.1 Fabrication process

This first section will describe the fabrication technique for the samples that have been used in the work reported in this chapter, as well as the one of chapter 5. The sample is based on silicon-on-insulator (SOI) architecture, where optical circuits are realized out of a thin silicon layer, by means of litography and etching. After a short part about the fabrication technique, we will describe the experimental configuration necessary to work with this kind of samples, and the results of the characterization of the devices.

4.1.1 Fabrication of OpSIS samples

The SOI-based samples under study were fabricated at A*STAR Institute of Microelectronics (IME), as part of the OpSIS project (see introduction of chapter 2) for the development of high quality CMOS-compatible multi-project wafers with photonic devices.

The fabrication consists of an industrial process applied to a silicon-on-insulator (SOI) wafer from SOITEC. SOI is a multi-layered structure constituted by a 220 nm-thick boron-doped silicon layer on top of a 2 μm-thick buried oxide layer, over a bulk silicon substrate, having a total thickness of less than 1 mm. The high refractive index contrast between silicon ($n = 3.49$) and silicon oxide ($n = 1.46$) allows to strongly confine light in the thin silicon layer thanks to total internal reflection (TIR). As will be described later, this architecture can be used as basis to realize different kinds of photonic devices, such as channel waveguides, grating couplers, microring resonators, etc. To do this, the first step consists of generating a mask of the layout over the top silicon surface. This can be obtained by means of UV photolitography: a photoresist is first deposed on the surface, focused UV radiation at 248 nm is used to draw the circuit and then the development removes the regions that have been illuminated. Anisotropic dry etching at different depths is performed to define the structures in the 220 nm-thick silicon layer. The first etching step to a depth of 60 nm is used for grating couplers, a second step at 130 nm is used for rib waveguides. A final full-depth etch, down to the oxide substrate, is used to pattern the ridge waveguides with height 220 nm and width 500 nm, designed to be single mode in the $1500 - 1600$ nm wavelength range.

A diagram of some of the devices that can be realized, associated to their cross-sections, is shown in Fig.4.1: here the three possible etching depths are visible, together with the aluminum routes that can provide connection to electrical contacts. Phosphorus implantation is performed on the exposed silicon layer, in order to obtain n-doped regions for the thermal tuning of individual components. The top of the sample is then filled with an oxide cladding, with an average thickness of about 2 μm. A following thermal annealing at 1030 °C for 5 seconds is performed to activate dopants. The final step is the realization of contact vias and two levels of aluminum interconnects.

From preliminary studies of the transmission properties of the sample, the

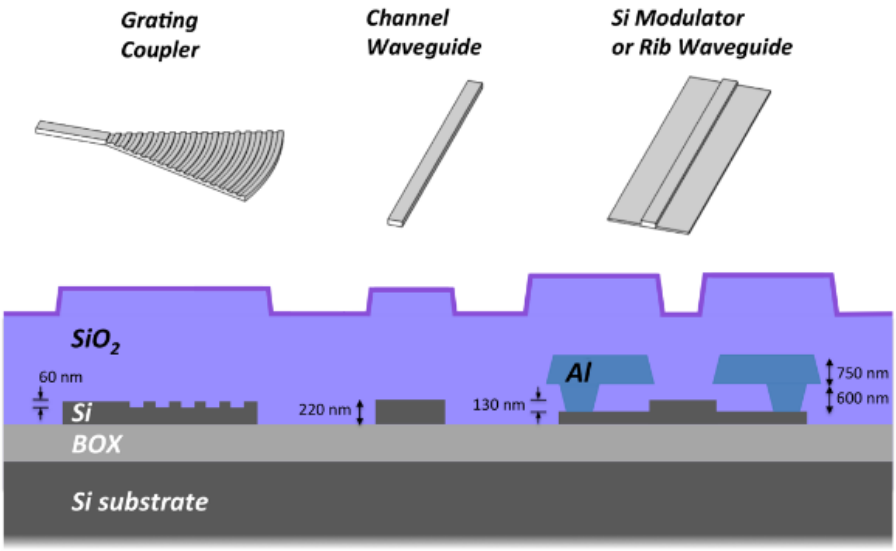

Figure 4.1: Diagram of the components that can be found in the OpSIS chip with the respective cross sections. The platform features a 220 nm top silicon layer that has three possible etch depths: 60 nm is used for grating couplers, 130 nm for rib waveguides, while full etch is used for ridge (channel) waveguides [182].

measured losses were 2.7 ± 0.06 dB/cm for the ridge waveguide and 1.5 ± 0.6 dB/cm for the rib waveguide [183].

Grating couplers

In order to build large-scale photonic system on-chip, achieving low insertion losses is a priority that in our device was obtained using grating couplers, exploiting the advantages that they offer with respect to edge-coupling (see section 2.1). In fact, they enable efficient wafer-scale testing, they can be placed everywhere across the wafer and are more alignment-tolerant. The working principle of the grating couplers is based on the diffraction of light out-of-plane into a fiber placed approximately normal to the surface. It can be done with a diffraction grating as the one shown in Fig. 4.1, that in our device is realized by means of a shallow silicon etch of 60 nm.

The major issue with this component is bound to losses: substrate loss, for instance, is due to the gratings being nearly symmetric in vertical direction, bringing to a leakage of the optical power into the substrate, estimated to be around 35-45%. Another problem is the different shape between the exponential mode of the grating and the gaussian mode of the fiber, leading to mode-mismatch losses. Such losses can be reduced, as in our case, by using non-uniform focusing gratings to better match the diffracted profile with single mode optical fibers [184]. The gratings that we utilize are also characterized by a large diameter of the mode, on the order of 10 μm, that enables a stable optical coupling. The reported average insertion losses for gratings with such designs are 3.1 dB at 1550 nm, with a 1.5 dB bandwidth of 50 nm [185].

We want to notice that the grating couplers in our sample are aligned and separated by a fixed distance of 127 μm: this gives the possibility to utilize a single array of optical fibers, whose cores are separated by the same distance of 127 μm from each other, to couple light into and out of the sample. This is a useful trick to achieve simpler and faster alignment operation.

The result of the characterization of our grating couplers, consisting of the transmission spectrum of two cascaded gratings, will be reported in section 4.2.2.

Generating microring

The generating microring, intended to be the source of photon pairs, is designed to have a high Q factor and power density, while allowing for resonance tuning. To achieve a high Q factor, a low-loss ridge waveguide geometry, with a cross-section of 500 × 220 nm^2, is adopted. The radius of the ring is 15 μm, in order to increase the relative power density, resulting in a wavelength separation between resonances of about 6 nm. The ring is designed to be at critical coupling, in order to optimize the extraction efficiency of the generated photons.

One peculiar aspect of OpSIS samples is the possibility to tune the resonances of the ring driving them with an external current. However, the presence of dopants, necessary to achieve tunability, could lead to a degradation of the quality factors, thus reducing the efficiency of the spontaneous four-wave mixing process. This can be avoided using a heater system that consists of a 220 nm-thick inner semi-ring, doped with high concentration phosphorus, separated from the generating ring by a 1 μm wide silica cladding to avoid mode coupling between the two structures. The nominal resistance of the device is about 360 Ω: with this value we expect that we can tune the resonance along one FSR with currents of few mA. We refer to section 4.2.2 for a detailed characterization of the generating ring, where a fitted resonance and a result of the thermal tuning will be reported.

DBR filter

A generic distributed Bragg reflector (DBR) is a mirror structure that can be obtained from a periodical sequence of layers of two materials with different refractive index. In our integrated DBR, the modulation of the refractive index is achieved by periodically shrinking the waveguide width from 500 nm to 440 nm, exploiting the dependence of effective index from waveguide width (see section 2.1). The geometric features used in its design go beyond the diffraction limit of the UV beam used in the photolitography process, resulting in an effective "shallow" modulation of the width. Our DBR, in particular, was designed to have strong reflectivity in a stop band of about $1-2$ nm, centered around $\lambda_0 = 2n_{eff}\cdot\Gamma \approx 1536$ nm, as defined by $\Gamma = 320$ nm and $n_{eff} = 2.4$, and with a high transmission in the side bands. The effective central wavelength of the stop-band can vary due to slight variations of the silicon layer thickness.

Since preliminary attempts showed that a DBR with N = 2000 periods has an extinction ratio of about $20-25$ dB, a total number of periods equal to N = 8000 was chosen in order to reach a pump rejection above 80 dB, necessary to filter out the bright residual pump after the spontaneous FWM process. However, in order to limit the total footprint of the sample, the DBR is folded in the middle with a 180° bend, as can be seen in Fig. 4.2. This could result in interference fringes that in principle could be removed by tuning a phase shifter, specifically designed to this purpose.

The experimental characterization of the DBR spectrum, along with a detailed transmission spectrum of the stop band, will be reported in section 4.2.2.

Tunable add-drop filters

The two add-drop ring resonators, intended to separate and route signal and idler, have been designed to have a FSR larger than the one of the pair-generation ring, thus they have a smaller radius of 6.5 μm. This results in a FSR of about 15 nm, allowing to avoid simultaneous spectral overlap between multiple resonances of the generation ring.

The tunability in this case exploits thermo-optic effect, enabled by a resistive heater embedded in the structure, in the form of doped silicon regions contacted by aluminum vias to the electrical interconnect layer. To minimize losses due to free carrier absorption the phosphorus dopant concentration must be kept low. For this reason, while for good electrical connection a phosphorus concentration of $5\times10^{20}\text{cm}^{-3}$ is used, its value is kept low, around $5\times10^{17}\text{cm}^{-3}$, in the waveguide region overlapping with the optical mode. The resistance of the device is approximately 130 Ω. To maximize the collection efficiency the add-drops are in overcoupling configuration, leading to a loaded Q much lower than its intrinsic value.

The characterization of the add-drops is reported in section 4.2.2, where the transmission spectrum of a resonance and the result of thermal tuning will be shown.

4.1.2 Chip layout

All the above-mentioned components are constituting parts of the sample that was used in this experiment. A micrograph picture of the whole sample is shown in Fig. 4.2, that has been slightly modified for more clarity. The in- and out- coupling are provided by an array of six non-uniform focusing grating couplers (two of which are not visible) aligned along the same direction and separated by a constant distance of 127 μm. The two upper gratings should be used for the alignment of the sample, while the input grating (1) injects the light in a rib waveguide to which the tunable generating microring (2) is coupled. If we follow the optical path, right after the ring we can find the Bragg reflector, divided in two segments, each with 4000 periods, to reduce the total footprint. As can be seen from the image, an optical phase shifter is located close to the 180° bend between the two segments of the DBR, that was designed to correct eventual Fabry-Pérot interference fringes. The total length of the DBR, which is not visible from the picture, is of about 1 mm. After that, a directional coupler splits the waveguide in two directions: one is used for monitoring the output of the ring-DBR subsystem, the other one is sent to the add-drops resonators (4) and (5), that have been designed to further filter the pump and demultiplex signal and idler photons. The output grating (8), not shown to reduce the size of the image, collects the common through port of the add-drops, while their drop ports are delivered to outputs (6) and (7). In correspondence to the add ports two Germanium photodiodes are visible, that were intended to help align the signal and idler resonance frequencies, but they were not used in our experiments.

A more schematic representation is shown in Fig. 4.3, where a sketch of the sample is associated to the task of each device, as described in the caption of the image.

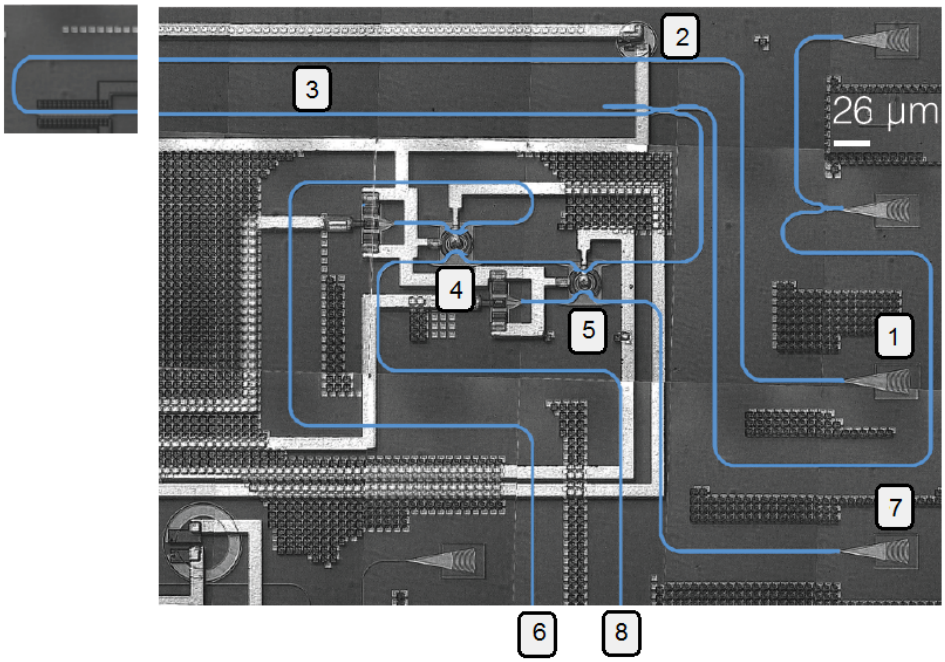

Figure 4.2: Micrograph image of the sample. On the right side of the image, the grating couplers used to couple light into/out of the device are visible. In particular, grating (1) is used as input for pump light, that is then delivered via a 500×220 nm^2 ridge waveguide to the microring (2), which is used as photon pair source. The DBR (3) composed by two parallel segments, is used for spectral filtering of the residual pump. The multiplexed signal and idler photons are then sent to tunable add-drops (4) and (5), for demultiplexing and/or further spectral filtering. The drop ports of (4) and (5) are sent to the grating couplers (6) and (7) respectively, while all the light that is not coupled to the add drops will exit from the through port and collected by grating (8). The picture has been modified for better clarity: the channel waveguides are put into evidence by the light blue colouring, and portion of the DBR (3) and grating couplers at the outputs (6) and (8) have been cut out to reduce the size of the image. To give an idea of the total footprint, a chip with a surface of 2.4×1.36 mm^2 can be fitted with four of the reported devices.

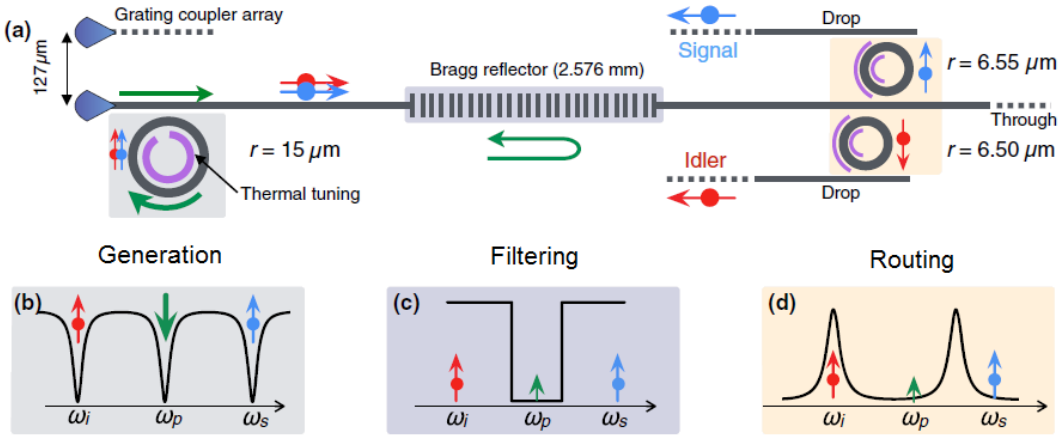

Figure 4.3: (a) Representation of the sample, with a schematic description of the task of each component. In- and out- coupling are provided by an array of equally spaced grating couplers. The generating ring, pumped at resonance frequency ω_p, generates photons in adjacent resonances at frequencies ω_i and ω_s, exploiting SFWM (b). The generating microring can be thermally tuned until the pump resonance falls inside the stop band of the DBR filter, which has a bandwidth of about 1 nm (c). In this way, the pump light will be reflected by the DBR, while the generated photons will be able to pass almost undisturbed through it, since they will be at a distance of a FSR of the generating ring (about 6 nm). The two add-drops can be thermally tuned so that one of them is in resonance with the idler frequency (d), while the other one is in resonance with signal frequency, and they will be delivered to distinct drop ports. In this configuration, generated signal and idler photons can be demultiplexed to different channels and sent to two different outputs of the sample. The ratio between the add-drop and generating ring radii are chosen so that their FSR are not multiple, and a single add-drop cannot collect idler and signal photons generated from resonances of the same order simultaneously.

4.2 Characterization of the samples

The preliminary part of the measurements was the realization of the experimental set-up, which required a meticulous and accurate preparation. This preliminary work of set-up arrangement and optimization, as well as a proper choice of the sample, are extremely important in order to perform the experiment. The experimental set-up that we are going to describe is schematically represented in Fig. 4.4. Next, in this same section, we will report on the results of the characterization measurements of the different devices on chip.

4.2.1 Experimental set-up

The sample is mounted on an aluminum support placed over a Peltier element, which is used to set the temperature of the sample between 10°C and 50°C, with a sensitivity of about 0.1°C. The temperature of the Peltier is controlled by a thermocouple placed on the aluminum support solidal to the sample, exploiting a PID controller with a stabilization feedback. All the elements were pasted to the support with a silver lacquer, providing a good thermal conductivity, for a better homogeneity and faster response of the temperature stabilization. The Peltier is basically used to control the temperature of the whole chip.

A custom-made microscope, mounted on a translating stage, is used to image the sample from the top. A magnified image of the sample is focused to both a visible and an infrared (Xenics) CCD camera, which redirect the image to two screens where the top view of the sample can be visualized, with an effective magnification of the setup on screen of about 200×. The microscope was designed to achieve such magnification even if the working distance from the surface of the sample must be of several centimeters, in order to leave enough space to align the fiber array above it. The microscope is necessary to accurately align the transmission line, as well as the metallic tips on the electrical pads to control heating elements. Another CCD camera, not shown in the setup in Fig. 4.4 provides a lateral view on the sample, useful to monitor the distance of the fibers, and of the metallic tips, from the upper surface of the chip.

The fiber array, schematically represented on the right side of Fig. 4.4, is aligned on top of the sample and used to couple incoming and outgoing light, mounted on a holder with a total of 6 degrees of freedom, composed by a triple-axis piezoelectric translator and triple-axis rotating stage, to finely adjust the position and orientation of the fibers. The spacing between the cores of the optical fibers in the array is 127 μm, which is equal to the spacing between the grating couplers on the chip, allowing for the simultaneous alignment of up to 8 channels.

From the design of the grating couplers, the field comes out with a mode angle of 17° with respect to the normal [184]. In order to optimize the coupling, the fiber array must be brought very close to the sample, ideally at a distance

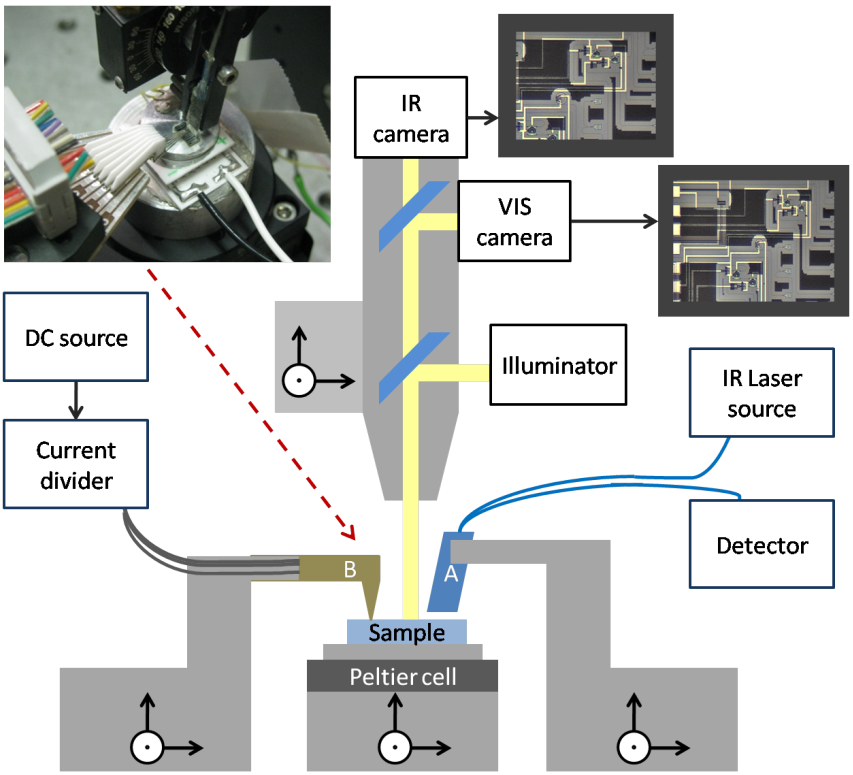

Figure 4.4: The sample is put on top of a Peltier element, mounted on a 2-axis translation stage and a rotating stage. On top of the sample a custom-made microscope is installed, mounted on a 3-axis translation stage, used to illuminate the sample and to project its magnified image on both a visible and an infrared camera. The fiber array A, aligned on top of the sample and used to simultaneously couple incoming and outgoing light, is mounted on a translator with a total of 6 degrees of freedom, composed by a 3-axis piezoelectric translation and 3-axis rotating stage. The array consists of 8 fibers: the one chosen as input is connected to an infrared laser source, while the output fiber is sent to a detector (see main text for more details). The metallic tips B, mounted on a 3-axis translating and a rotating stage, are used to deliver different currents to the heaters on the sample through the metallic pads. The currents are provided by a DC source connected to a custom-made current divider with variable resistances. The inset figure in the upper left corner is a picture of a detail of the experimental set-up, where the metallic tips and the fiber array aligned to the sample are visible.

of few microns: for this reason the fiber array needs to be polished with the removal of its back corner that otherwise would prevent to reach such a small distance from the surface. If the fiber array was polished at an angle of 14.5°, light would come out with an angle matched to the mode of the grating coupler. However, the fibers that we used have been polished at a slightly lower angle, i.e. 11.5°, in order to have more flexibility and to have the possibility to tune the inclination of the fiber in order to optimize the coupling, and at the same time minimizing the distance. In order to calculate the correct angle of the array we took into account the refraction of light at the interface between air and the fiber, that can be derived by Snell's law. The optimal angle of the array with respect to the normal turned out be around 9.5°. We want to notice that the possibility to modify the wavelength of maximum coupling by changing the inclination of the fiber is a direct consequence of the dispersion in the medium of the fiber.

In order to measure the transmission spectra, an infrared laser, used to excite the system, is injected into the fiber aligned to the input grating, while the fiber aligned to the output grating is sent to a detector. We adopted two different configurations for the transmission measurements. For a rough alignment and fast characterization, superluminescent diode (Thorlabs SLD1550P-A1, controlled by Newport Model 6000) was used as a broadband source, and the transmitted light was sent to o spectrometer (Acton Spectra Pro 2500i) and collected by a liquid nitrogen cooled CCD camera (Acton InGaAs OMA V). The best spectral resolution that can be achieved with this transmission set-up is 70 pm. In the alternative configuration, the source consists of a monochromatic tunable infrared laser (Santec TSL-510), used in scanning mode, and an InGaAs detector (Newport 918D-IG-OD3) connected to a high dynamic-range Powermeter (Newport 1936-C), after which the spectrum can be reconstructed by a Labview software. This configuration is much slower, in fact a broad and highly resolved spectrum can take several minutes, not allowing for live alignment, and could suffer of mechanical instability. On the other hand, it is the only way to reach the resolution of 1 pm, that is needed to resolve high Q resonances.

The metallic tips, on the left side of Fig. 4.4, are mounted on a triple-axis translating stage with a rotating stage for in-plane adjustment. The tips have to be aligned and contacted to resistive pads on the surface of the sample, that through aluminum interconnects provide current to the heaters. The current, generated by a DC supplier, must be divided in order to deliver current to different heating devices simultaneously. To do it, we realized a customized current divider that could be used to split the current into 10 different channels, each one carrying a current that could be set independently from the others by controlling variable resistances.

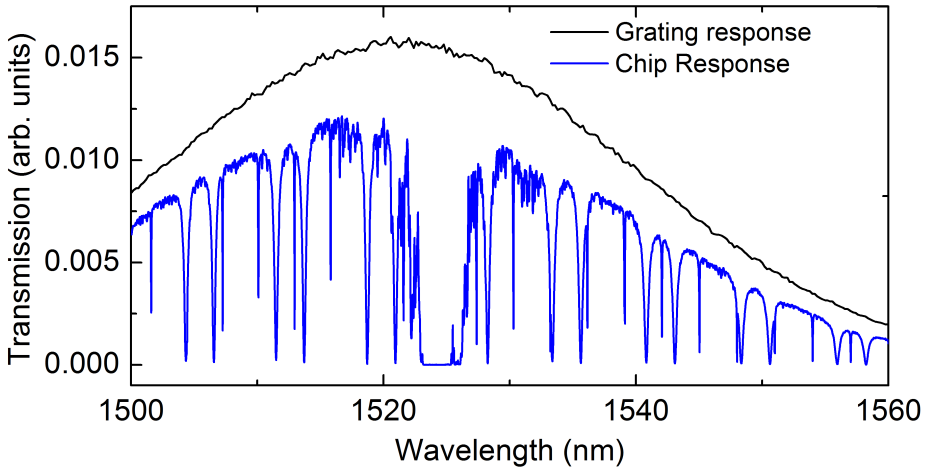

Figure 4.5: Transmission spectrum of the sample: blue line is the transmission of the whole circuit, while black line is the the transmission spectrum of an alignment loop composed by two grating couplers and a waveguide. The two spectra were measured keeping the fiber array at the same angle with respect to the normal of the sample.

4.2.2 Results of the characterization

In order to characterize the sample and to optimize the alignment, the first step is to characterize the coupling condition. To do this, we started by determining the response of the grating couplers, which can be done by measuring the transmission spectrum of a closed loop with two gratings and a waveguide, using a broadband laser as a source and a cooled CCD camera as detector for live alignment. The angle of the fiber array was set in order to have the highest transmission of the grating at the wavelength for which we need the maximum coupling. This coincides with the DBR central wavelength, because it is where we want the pump resonance to be in order to use the DBR for pump rejection. After a first rough alignment of the grating, one can know exactly the position of the DBR and then tilt the angle of the fiber array in order to maximize the transmission at that wavelength.

A transmission spectrum of two cascaded grating couplers is reported in Fig. 4.5, represented by the black line, plotted together with the transmission of the sample, represented by the blue line. The two spectra have been measured maintaining the same inclination of the fiber array, i.e. in the same coupling condition. As can be seen from this graph, the grating response modulates the intensity transmitted by the sample, with a full width at half maximum of about 50 nm and average insertion losses that we measured to be about 5 dB.

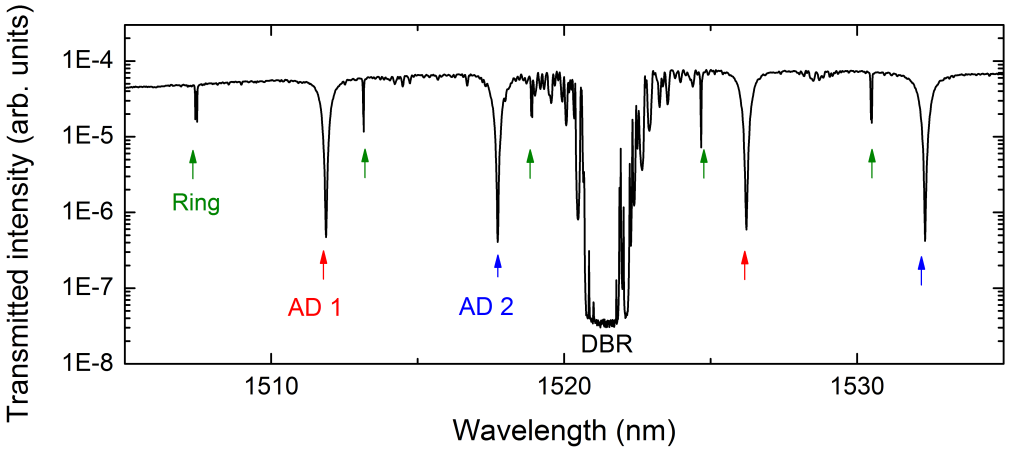

Figure 4.6: Transmission spectrum of the sample collected from the through output: the narrow dips pointed by green arrows are the resonances of the generation ring, the broader dips pointed with red and blue arrows are the resonances of the two add drops, the wide band around 1520 nm is the stop band of the DBR. Notice that the features in the bottom of the stop band of the DBR are not resolved.

After the alignment operation, it was possible to take a high-resolution transmission spectrum of the sample, as the one shown in Fig. 4.6, where the transmission of all the components on the chip is clearly visible. The broad stop band around 1525 μm is due to the reflection of the DBR, the dips pointed by red and blue arrows are the resonances of the add-drops and the narrow dips pointed by green arrows are the resonances of the generating ring.

Generating and add-drop microrings

The characterization of the microrings consists of measuring the transmission spectra of the resonances and fitting them with lorentzian functions. The results are shown in Fig. 4.7, where the resonance dip of an add drop (a) and a generating ring (b) are shown, together with the lorentzian curve that better fits the data. The parameters obtained by the fit are the linewidth $\Delta\lambda$ of the resonance and its central wavelength λ_0, that can be used to calculate the Q factor exploiting equation (2.15), that we recall here for convenience

$$Q = \frac{\lambda_0}{\Delta\lambda}.$$

Add drops have a typical linewidth of about 300 pm, resulting in $Q \approx 5 \times 10^3$, while the narrower resonance of the generating ring leads to values up to $Q \approx 5 \times 10^4$, corresponding to a photon lifetime of about 30 ps. Such a high quality factor is needed to reach the enhancement to perform SFWM with high

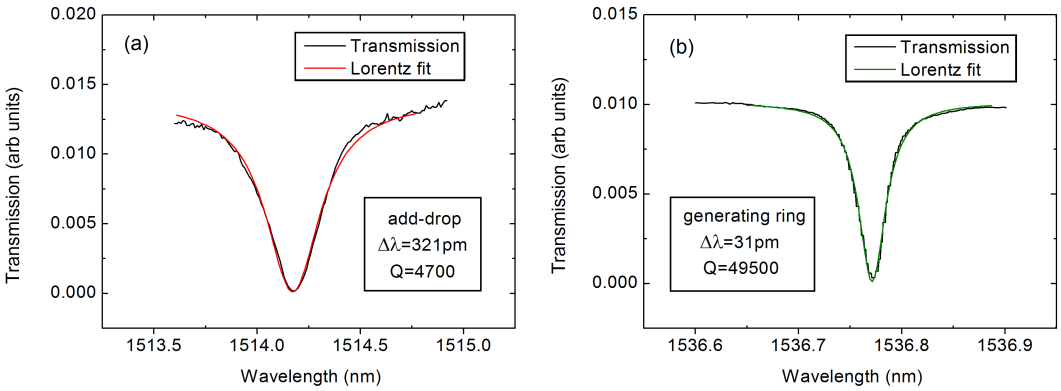

Figure 4.7: Transmission of the resonance dip for an add-drop (a) and a microring (b), measured with the set-up for high-resolution measurements, with a tunable monochromatic laser as source and an InGaAs detector. The curves have been fitted with a lorentzian function, whose result is represented by the red (a) and green (b) line, respectively. Add drops have a typical linewidth of about 300 pm, resulting in a Q≈5000, while it is much narrower for generating ring, around 30 pm, leading to quality factors up to Q≈50000.

generation rate at low pump power [41]. The FSR for add-drop resonators was measured to be about 14.4 nm, while it is 5.7 nm for the generating microring, while insertion losses for the add-drops are estimated to be around 1.5 dB. The Q factor of the add-drops is preferred to be lower than that of the generating ring, in order to have more flexibility when using them as filters and demultiplexers. In fact, if they were too narrow, even small perturbations could bring to an overall instability of the device.

The second part of the characterization of microrings deals with the thermal tuning, whose results are reported in Fig. 4.8 (a) for the generating ring and Fig. 4.9 for the add-drops. The graph in Fig. 4.8 (b) shows the shift in the position of the pump resonance as a function of the dissipated power. The experimental points are closely following a linear trend, allowing to accurately predict the position of the resonance knowing the dissipated power. We notice that a linear dependence from power means a quadratic dependence from current: this constitutes a practical limitation to the maximum shift that can be achieved.

Even though the add-drops have been designed to be tunable across a whole FSR, we found that in our sample the shift of the resonance is associated to a reduction of the Q factor. This effect is clearly visible in the graph reported in Fig. 4.9, where for increasing currents there is a progressive degradation of the resonance lineshape. This phenomenon, although found to be reversible when stopping the current, it affects the filtering capability of the resonator. Thus, in the preliminary part of our experiment, we found more convenient to search for a sample where the add-drops resonances had to be tuned just of few nm.

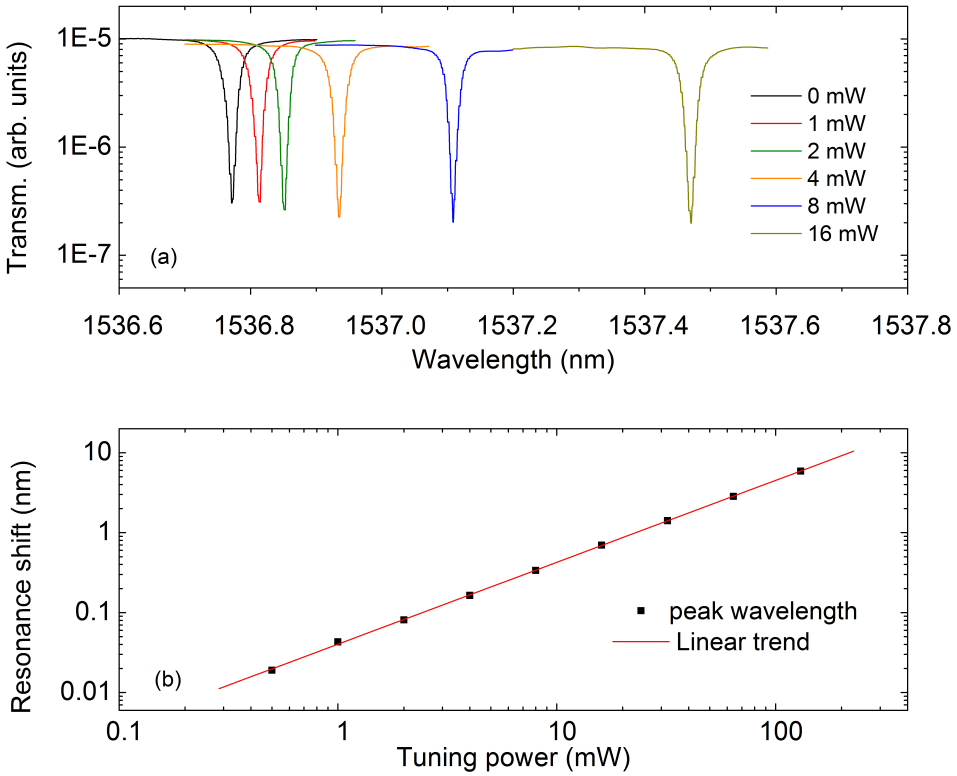

Figure 4.8: Characterization of the thermal tuning for the generating microring resonance. (a) Position of the resonance of the generating ring for different values of the tuning current. The legend allows to associate the power dissipated in the heater to each resonance position. (b) Linear dependence: each point is the dip wavelength as a function of tuning power. The red line represents a linear trend, which is closely followed by the experimental points: this allows to accurately predict the position of the resonance from the tuning power (or current).

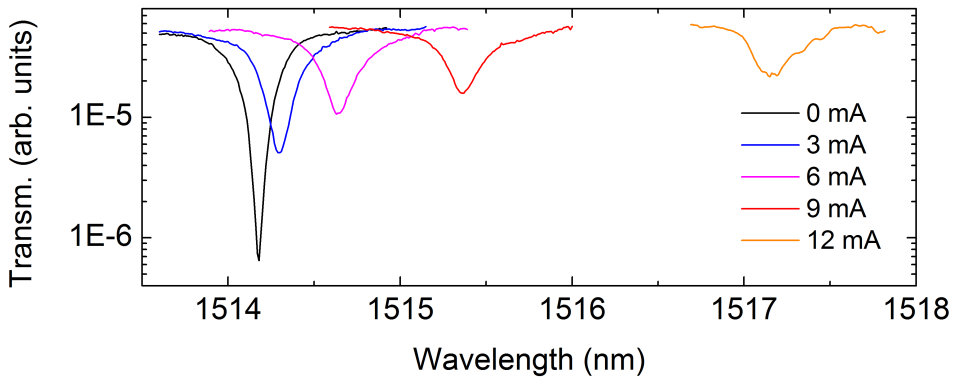

Figure 4.9: Shift of an add-drop resonance when applying different tuning currents. The dissipated power can be found from the nominal resistance of the heaters, reported in section 4.1.1.

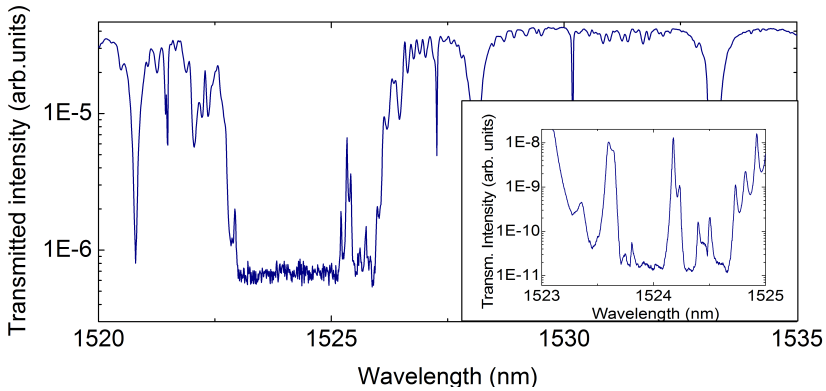

Figure 4.10: Characterization of the DBR: the larger spectrum is measured without filtering the ASE sidebands of the laser (see main text for more details) so the bottom of the DBR appears flat and truncated. The spectrum in the inset was obtained instead by using a tunable bandpass filter to clean out the ASE of the laser, allowing us to measure the bottom of the stop band. The reported transmissions are in arbitrary units, but the scales of the two graphs are consistent with each other. Thus, from the ratio between the maximum transmission and the average bottom of the stop band, it can be inferred that the rejection of the DBR is on the order of 65 dB.

We suggest that this problem, however, could be simply avoided by adopting the same kind of heaters of the generating microrings. In fact, as explained in section 4.1.1, they have been designed in order to avoid the presence of dopants in the resonator, allowing to achieve a good tunability without substantially affecting the Q factor.

DBR filter

To characterize the DBR we start by the analysis of the transmission spectrum in the stop band region. As can be seen from the transmission spectrum reported in Fig. 4.10, the irregular shape of the stop band does not allow to determine a precise value for the bandwidth, but from several measurements it turned out to be around $1 - 2$ nm, with central wavelength varying around 1525 nm.

The transmission spectrum reported in Fig. 4.10 was measured using a tunable laser in scanning mode and a InGaAs detector. The result is a truncated stopband of the DBR, whose bottom could not be measured, due to the noise of the integrated ASE of the laser, that prevents to succesfully measure the rejection of the DBR. In fact the tubable IR laser used for high resolution measurements (Santec TSL510) is characterized by a ratio between the laser peak and ASE background of about 30 dB. It means that, even if the dynamic range of the detector is higher, if the ASE is not filtered we are limited in the

measurement of a rejection lower than 30 dB. We solved this problem by using a tunable bandpass filter (Santec OTF 350) that provides a 50 dB of side-band suppression: tuning the bandpass in correspondence of the stop band of the DBR, we were able to measure its actual spectral response, with a result that is reported in the inset of Fig. 4.10. From this spectrum, the non-uniformity of the stopband is clearly visible: it can overcome 70 dB of suppression in some narrow wavelength ranges, but has a mean value of about 65 dB. We can attribute the inhomogeneities in the transmission to weak Fabry-Pérot fringes, due to the bend between the two sections of the DBR. Tuning the phase-shifter, which was intended to correct this effect, did not bring any substantial improvement.

The second part of the characterization of the DBR consisted in the study of thermal tunability. As already described, the sample had to be placed above the Peltier element, in order to control the temperature of the whole chip. In fact, during measurements, it turned out to be very useful to stabilize the temperature while tuning the ring and the add drops, since we observed that when tuning three devices simultaneously the system is not stable probably because of thermal inhomogeneities and fluctuations. The Peltier element turned out also to be an essential component for the chip-to-chip experiment, that will be described in section 4.4, where spectral tuning of the DBR was needed. The Peltier allows to control the temperature of the sample between 10°C and 50°C. From preliminary measurements, we were able to determine a tuning coefficient of about 70 pm/°C, resulting in the possibility to rigidly shift the spectrum of the sample along a range of 3 nm.

Control experiments showed that the measured rejection of the DBR is reduced from the expected value of $80 - 100$ dB, to a measured value of approximately 65 dB. We suspect that this could be due to laser light backscattered from the surface of the sample, in particular from the oxide cladding and the silicon substrate, and coupled directly from the input to the output fibers, without entering in the waveguides. If it was the case, a better rejection could be achieved by modifying the sample in order to reduce the amount of collected backscattered light. For instance, this could be obtained with a larger spatial separation between the input and output gratings, or inserting trench structures, to reduce the amount of collected backscattered light. Another hypothesis that could justify this mismatch between the expected and measured rejection is bound to the disorder that could result from the features of DBR going beyond the diffraction limit of the beam used in the litography process. In fact the presence of disorder or randomness of the periodic structure, could induce a saturation of the dependence of the DBR reflection from the number of periods [186]. For this reason, we propose to carry on further studies on the considered kind od DBR, in order to explicitly determine the dependence of reflection from the number of periods. Another solution could consist in the development of an alternative design, without going beyond the diffraction limit, in order to reduce eventual randomness effects.

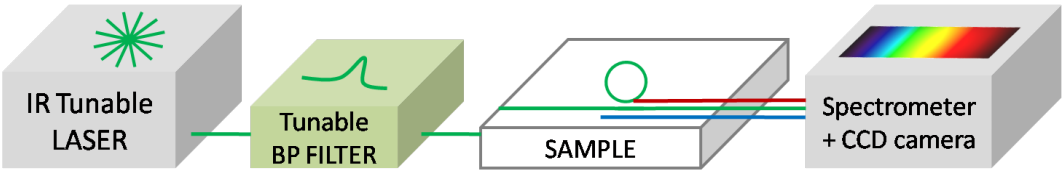

Figure 4.11: Schematic representation of the setup for the SFWM measurements with on chip filtering. The ASE sidebands of the pump laser are removed by a tunable bandpass filter. The filtered pump is injected into the chip, which is in the same configuration as the one represented in Fig. 4.4, with translators to align sample, fiber array and metallic tips. The through port of the sample is collected by a fiber, delivered to a spectrometer and collected by a CCD camera.

4.3 SFWM with on-chip filtering of the pump

A representation of the experimental set-up for the SFWM measurements is shown in Fig. 4.11. The sample is mounted in the same set-up as the one that was represented in Fig. 4.4. The excitation is provided by a tunable monochromatic laser (Santec TLC 510), spectrally cleaned with a tunable bandpass filter (Santec OTF 350) to suppress ASE sidebands that could compromise the visibility of the expected generated photons. The pump laser is injected into the sample via one of the 8 ports of the fiber array, that is aligned to the array of gratings on the sample. We refer to back Fig. 4.3 for a scheme of the sample layout and of how it is intended to work. Since the resonance wavelength of the generating ring can in principle be out of the DBR spectrum, thermal tuning is needed to bring the resonance inside the stop band of the DBR. The FSR of the generating ring is much larger than the filtering bandwidth of the DBR, ensuring us that idler and signal generated photons will pass undisturbed while the pump laser will be reflected. The only requirement is that we choose a resonance at a wavelength below the DBR bandpass, since the integrated heaters can only produce a redshift of the resonance. After the tuning of the ring resonance, the pump laser must be set at the same wavelength. From a practical point of view this is non trivial, since when the resonance is in the middle of the DBR, it is not visible anymore in the transmission spectrum. However, we can estimate its position taking advantage of the linear dependence from the tuning power, and then optimizing it by maximizing the generated signal and idler, if they are intense enough to be optimized live, or by maximizing the coupling, that could be achieved with a minimization of the residual transmitted pump.

We want to notice that the light rejected from the DBR is actually back-reflected, causing the generation of signal and idler photons towards the input direction, that can be backscattered from roughness and sent back towards the output direction. This effect could in principle lead to an overestimation of

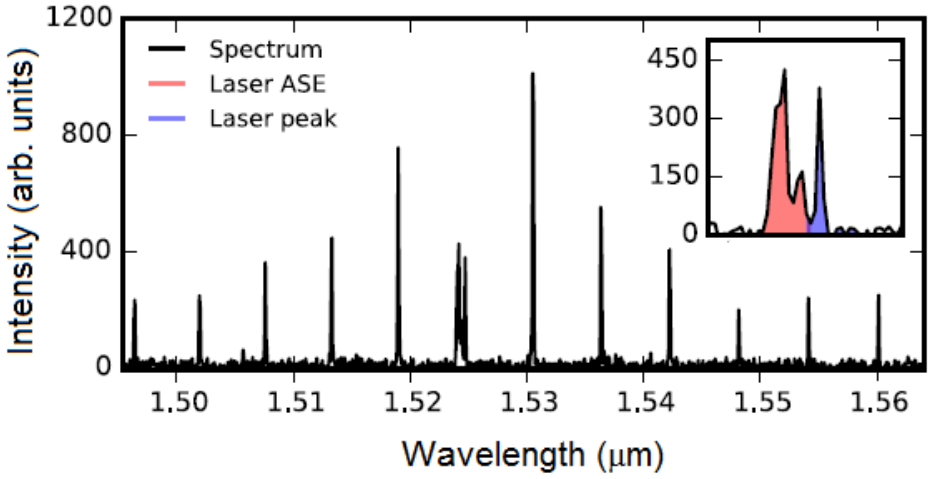

Figure 4.12: Spectrum resulting from a SFWM measurement in the single-chip experiment. The pump laser is set at a wavelength of 1524.7 nm, in correspondence with the resonance of the generating microring which has been tuned inside the DBR stopband. The pump laser is almost completely filtered by the DBR and the add-drops are tuned in resonance with it. The inset shows the residual laser (light blue) and the ASE of the pumping laser that was not filtered by the external filter. The resonances close to the pump wavelength are the brightest ones, while emitted intensity decreases moving far from the pump wavelength: this can be attributed to the response of the grating couplers.

the nonlinear generation efficiency. However, the pump light is diminished due to the coupling to the generating ring itself, leading the power of the back-reflected light to be about one order of magnitude lower than the incoming one, as could be inferred from the depth of the dip resonance of the generating ring, visible in Fig. 4.7 (b). This means that the generated photons, being quadratically dependent from the pump power, would be about two orders of magnitude less than the ones excited by the "original" pump, thus not significantly affecting the generation rate.

When the pump laser is set at the wavelength of the pump resonance, thus is in resonance with the ring, signal and idler photons are generated in correspondence of all the surrounding resonances, at frequencies that are symmetric with respect to the pump, due to conservation of energy, as expected from SFWM process. Since in this experiment the rejection of a single DBR, being ~ 65 dB, is not sufficient to suppress the pump, also the add-drops were tuned in resonance with the pump wavelength in order to further filter it, giving up on the possibility of using them as demultiplexers. We estimated that with this procedure a total extinction ratio of about $95 - 100$ dB is achieved. The generated photon pairs are not picked up by the add-drops, so they can be collected from the common through port. The outcoming light is then sent,

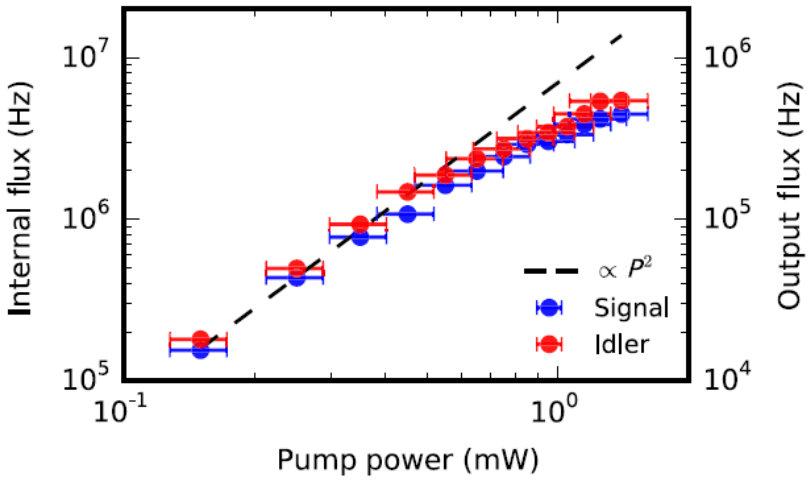

Figure 4.13: Dependence of SFWM generation rate for idler and signal fields, as a function of the power coupled with the ring. The dashed line is a guide to the eye proportional to the square of the pump power. The scale on the left is the internal generation rate, estimated inside the resonator. The scale on the right is the output flux, i.e. the external chip count rate, after correction for the CCD efficiency. Error bars are taking into account for uncertainties in the estimated coupled power, which is on the order of 10%.

without any external filtering stage, to a spectrometer and a liquid-nitrogen cooled InGaAs CCD camera used as a detector. The spectrum resulting from a SFWM measurement is reported in Fig. 4.12. Here a small amount of residual pump is still visible in the middle, as well as some of the residual ASE emission of the pump laser, as underlined in the inset of Fig. 4.12. The residual ASE could have been fully filtered, for instance, using a narrower bandpass filter prior to the sample: we suggest that this additional filtering stage could be easily realized on chip, for example introducing a further integrated DBR. The dependence of generated signal and idler power from the pump power is reported in Fig. 4.13. The external photon flux is obtained from the calibration of the CCD camera used for the detection with a high sensitivity powermeter. The internal photon flux is estimated inside the microring, taking into account for insertion losses along the optical path from the generating ring to the detector. As can be seen from Fig. 4.13 the internal generation rate can be as high as several MHz. The dashed black line represents a trend that is proportional to P_p^2, helpful to visualize that both signal and idler generation rate scale quadratically with pump power. However, the deviation from the quadratic trend at a coupled pump power of about 1 mW can be explained with pump power saturation due to two-photon absorption (TPA) in silicon [187].

One remarkable result with this first experiment is that by summing up

all the integrated intensities of the generated signal or idler peaks in a SFWM spectrum as the one shown in Fig. 4.12, the total generated power is 8 (10 for the idler) times larger than the residual pump laser. The remaining pump photons follow a poissonian statistic and they are not correlated in time: this means that the level of rejection achieved in our work could be already sufficient to perform quantum optics experiments, like heralding or entanglement measurements, with on-chip filtering. However, this result was achieved on our chip only by sacrificing the possibility to demultiplex signal and idler photons.

4.4 Chip-to-chip experiment

The second experiment involved two chips, nominally identical to the one used in the first experiment, where each chip has some specific tasks. The ring resonator and the DBR of the first chip A are used to generate photon pairs and to filter the pump. The resonances of the add-drops on chip A must be tuned far from generating ring resonances: in this way the signal and idler generated photons will exit from the through port of the chip, together with some residual pump. The output of chip A is then redirected on the input port of the second chip B, where the residual pump undergoes a second filtering stage by means of the DBR. In this case, temperature control of the whole chip is needed to tune the two Bragg reflectors in order to bring their stopbands to overlap. The add-drops on chip B are used to demultiplex signal and idler photons, that are then collected by the drop ports and exit from two different output grating couplers.

4.4.1 Chip-to-chip experimental set-up

In Fig. 4.14 a schematic representation of the set-up for measuring time correlations between photons generated in the chip-to-chip set-up is shown. Chip A is excited by a monochromatic infrared tunable laser, spectrally filtered with a tunable bandpass filter to remove the ASE of the laser. In this case the generating microring on chip A is used to produce the photon pairs by SFWM. Signal and idler, together with some residual pump, exit from the through port of chip A and are sent to chip B, where the add-drops are used to separate signal and idler.

In order to measure the SFWM spectra, the drop ports are sent to a spectrometer and CCD camera detection system, not shown in Fig. 4.14, and the experiment is carried out analogously to the already discussed single-chip experiment, with some differences. In this case in fact, the two DBR must overlap: this can be obtained controlling the temperature of one of the samples, that leads to a rigid shift of the whole transmission spectrum. The resonances of add-drops on chip A must be tuned far from the signal and idler resonances of the generating ring. On the other sample, in this case, the add- drops must be tuned in resonance with idler and signal wavelengths, in particular with he

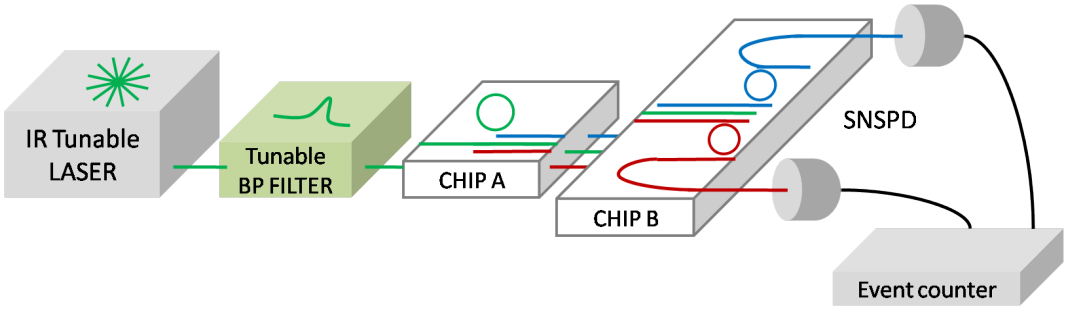

Figure 4.14: Schematic representation of the set-up for chip-to-chip experiment. The microring on chip A is excited using a spectrally filtered infrared tunable laser, and photon pairs are generated by SFWM. The resulting signal and idler, exit from the through port of chip A and are sent to chip B, where the DBR filters the residual pump and the add-drops are used to separate signal and idler. To measure the SFWM intensity, the drop ports can be first sent to a spectrometer and CCD camera detection system, not shown in the picture. For correlation measurements, instead, the output of each drop port must be sent to a superconducting single-photon detector (SSPD), whose output voltages are sent to an event counter used to build coincidence histograms, in order to estimate the time-correlation of the generated pairs. Both chip A and B are in the experimental configuration reported in Fig. 4.4, with fiber array for coupling, a microscope above, metallic tips aligned on the contacts, etc.

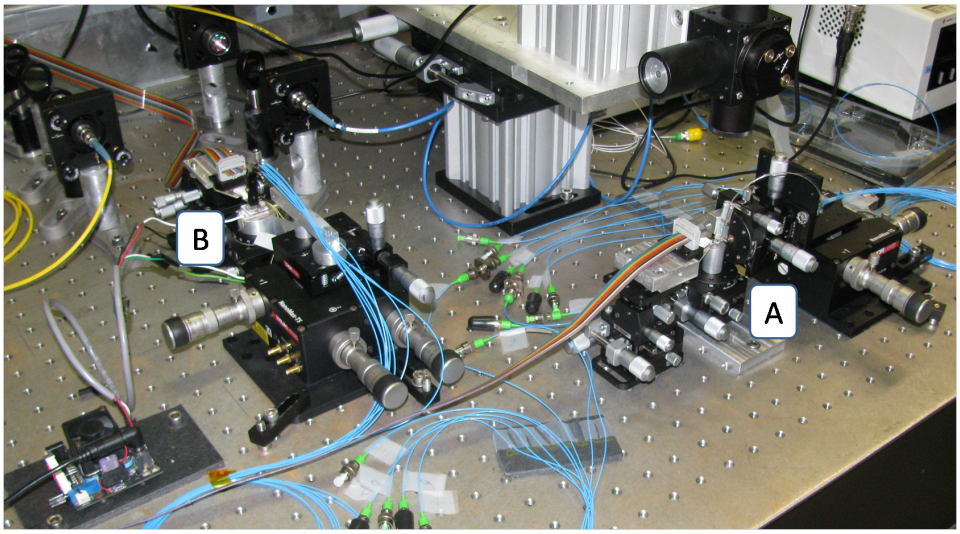

Figure 4.15: Photo of the experimental set-up in the chip-to-chip configuration. The lables are indicating the positions of the for generating (A) and routing (B) samples. Blue cables are single-mode optical fibers connected to the fiber arrays, coloured ribbons are electrical connections to the metallic tips.

brightest peaks symmetric with respect to the pump, in order to deliver them to two different drop ports.

From a practical point of view, the modification of the experiment required a lot of efforts, since we had to build a second experimental set-up for alignment and tuning, identical to the one represented in Fig. 4.4, for the chip B, with the exception of the microscope that could be shared between the two samples. The result is visible in the photo of the whole set-up, shown in Fig. 4.15. Another non-trivial task was to find a couple of samples that was suitable for this experiment. In fact, the central wavelength of the stop band of the DBR could vary of more than 10 nm among different samples, probably because of fluctuations in the thickness of the silicon guiding layer. However, the Peltier element allows to rigidly shift the transmission spectrum by a maximum of 3 nm. For this reason, we had to discard lots of samples until we found two of them with stopband that were close enough to be overlapped by thermal tuning.

After the first SFWM measurements, necessary also to optimize the tuning and alignment condition, the output of each drop port can be delivered to a superconducting-nanowire single-photon detector (SSPD by Scontel) as shown in Fig. 4.14. SSPD are based on a superconducting nanowire that work at temperature below 4 K, needing a system of pumped liquid helium to be cooled down. The output voltages of the SSPD are sent to an event counter, from which we are able to build coincidence histograms, used to estimate the time-correlation of the generated pairs. Both chip A and B are in the experimental configuration reported in Fig. 4.4, with fiber arrays for light coupling,

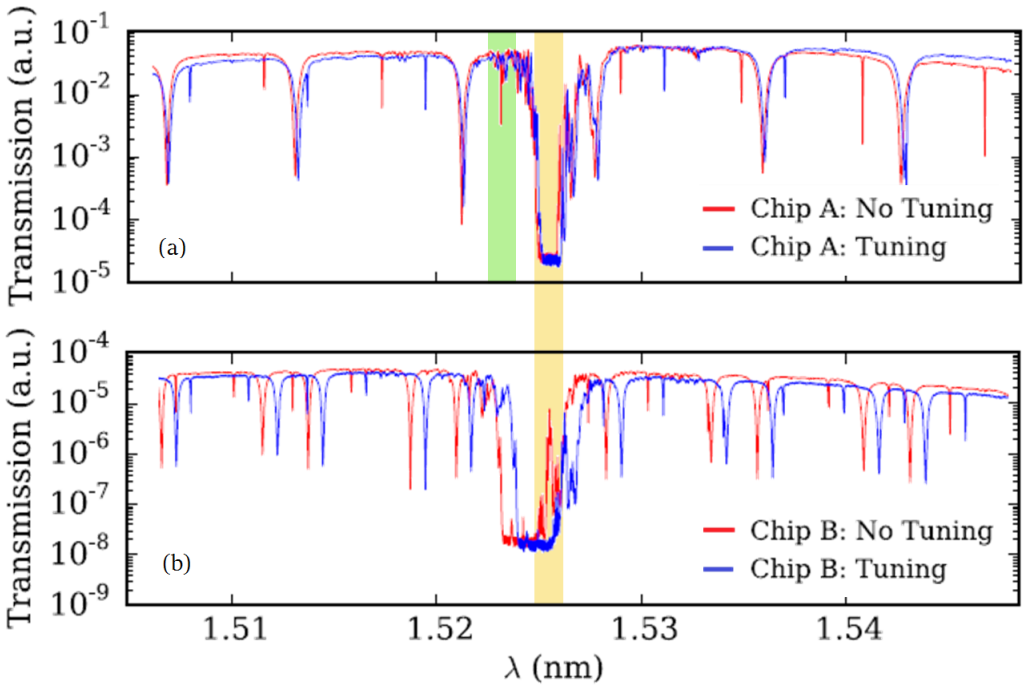

Figure 4.16: Effects of thermal tuning. (a) Transmission spectra of chip A before (red line) and during (blue line) the thermal tuning of generating microring. The pump resonance, highlighted with a green background, redshifts due to the thermal tuning and disappears inside the stopband of the DBR. (b) Transmission spectra of chip B before (red line) and during (blue line) the thermal tuning of the whole chip, achieved thanks to the Peltier element. The yellow background is intended to highlight the obtained spectral overlap between the DBRs on the two different chips.

a microscope above for alignment optimization, metallic tips on the contacts ot provide current to the heaters. The only difference consists in the function of the Peltier element. In fact, while in the previous experiment of on-chip filtering it was used just to stabilize the temperature of the sample, in this case is used to thermally tune the spectral response of the receiver chip in order to reach a perfect overlap between the stopband of the DBRs on different samples. This effect is clearly visible in Fig. 4.16, where the rigid shift of the transmission spectrum of chip B is shown, due to the change in temperature controlled by the Peltier element.

4.4.2 Integrated filtering and demultiplexing of photon pairs

The spectra reported in Fig. 4.17(a) and 4.17(b) are the result of SFWM measurement, collected from the through port of chip *B*, before (a) and after (b) tuning the add-drop resonances in correspondence of idler and signal peaks closest to the central pump resonances, which are also the brightest ones. The reason for the pronounced decrease in the peak intensities when increasing the spectral distance from pump wavelength, that can be noticed in Fig. 4.17 (a) and (b), can be attributed to the spectral response of input and output grating couplers. As expected, the generated peaks at the resonances selected by the tuned add-drops are not visible anymore in Fig. 4.17 (b). The disappeared photons can be found in the spectra reported in Fig. 4.17 (c) and (d), collected from the drop ports of the tuned add-drops. It can be noticed that no pump is visible in any of the drop ports: we estimate that the total pump isolation with this configuration is about 150 dB, accounting for the two DBR filters and the add-drop rejection.

From the result reported in Fig. 4.17 we can say that we succesfully achieved on-chip SFWM with complete rejection of the pump and demultiplexing of signal and idler, without the need of further off-chip filters.

4.4.3 Time-correlation measurements

The generated signal and idler photons, routed in different outputs, are delivered to two off-chip superconducting single-photon detectors (SSPD), without any other filtering stage. The superconducting materials work at temperature below 4K, for this reason the detectors must be mounted in a refrigerating unit inside a liquid He dewar at 1.7 K. The bias current of the detectors are set so that the dark counts are on the order of 300 Hz. The detection efficiencies are 5% and 10% for idler and signal, respectively. If compared to InGaAs detectors, the lower efficiency is compensated by a fast time response, which is 65 ps, instead of some ns, and much lower dark counts rate, on the order of 10^2 Hz instead of 10^4 - 10^5 Hz. Fiber polarization controllers are used along the two detecting lines in order to maximize the single photon detection rate. The response time of the detector sets a limit to the temporal resolution of the experiment: if we choose a time window corresponding to the time response of the detector, the resolution is equal to 65 ps. Time correlation measurements are performed with an event counter, in order to study the time-correlation of the generated photon pairs. The output from the detectors is correlated using a Picoquant Hydraharp event timer, which records a stream of events on a computer that has a dedicated software to build a temporal histogram, where a coincidence event is counted every time that two photons arrive at the two detectors with a certain delay from each other.

When two photons have been emitted in coincidence, and they run through the same optical length, they will get to the detectors with zero time delay. If

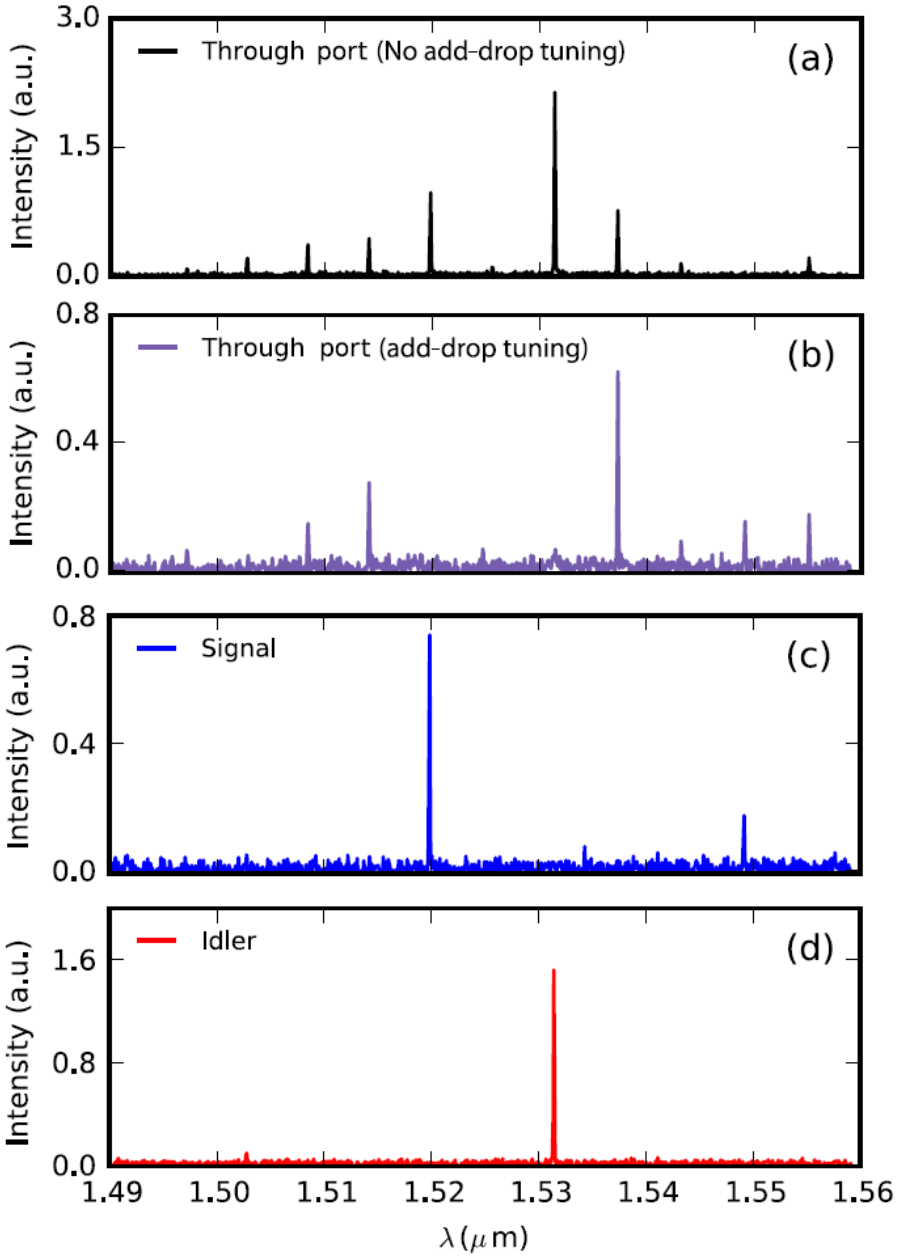

Figure 4.17: Results of SFWM measurements in the chip-to-chip configuration. (a) Output from the through port when the add-drop is not tuned. (b) Output from through port when the add-drops are tuned in correspondence of the brightest peaks. (c) and (d) are the output from the drop port collecting the signal and idler photons, respectively. We may notice that no residual pump is visible in any of the reported spectra.

Chip	Source of loss	Signal (dB)	Idler (dB)	Total (dB)	Ref.
A	DBR	3	3	6	
A	Multimode interferometer	0.28	0.28	0.56	[188]
A	Phase shifter	0.23	0.23	0.46	[189]
A	Monitoring tap	1	1	2	
A	Waveguide losses	0.31	0.31	0.62	[182]
A	Output grating coupler	5	5	10	
B	Input grating coupler	5	5	10	
B	Multimode interferometer	0.28	0.28	0.56	[188]
B	DBR	3	3	6	
B	Phase shifter	0.23	0.23	0.46	[189]
B	Monitoring tap	1	1	2	
B	Add-drop filter	1.5	1.5	3	
B	Waveguide losses	0.31	0.31	0.62	[182]
B	Output grating coupler	5	5	10	
	Detection efficiency	10	13	23	
	Total	36.14	39.14	75.28	

Table 4.1: Summary of the losses of signal and idler photons through the transmission line of the chip-to-chip experiment. Intrinsic waveguide propagation losses are 2.4 ± 0.3 dB/cm and grating coupler insertion losses are 4.4 ± 0.2 dB/cm.

there is a difference in their optical paths, it can be calculated in order to find the actual time delay corresponding to a zero delay from the source.

An example of the result of the time correlation measurements is reported in Fig. 4.18 (a), where a clear coincidence peak at zero time delay is visible. The events out of the central peaks are due to accidental events, that could have been caused by coincidences between dark counts and detection of only one photon of a pair.

The dependence of coincidence rate on pump power is is shown in Fig. 4.18 (b), where the pump power is estimated in the generating ring on chip A while the coincidence rate is the one measured after chip B. Each black dots in Fig. 4.18 (b) is obtained from a single correlation measurement. It can be seen from the graph that they are closely following the solid blue line, which represents the trend of the combined power of signal and idler generated by the same ring in the firs experiment. We specify that each point in 4.18 (b) is the result of a single measurement at constant pump power. The relatively low value of coincidence rate can suggest that every point required a long measurement time, on the order of one hour, to get a significant number of events in order to reach a good visibility. On the other hand, this can be seen as a demonstration of the good mechanical and thermal stability of our experimental set-up.

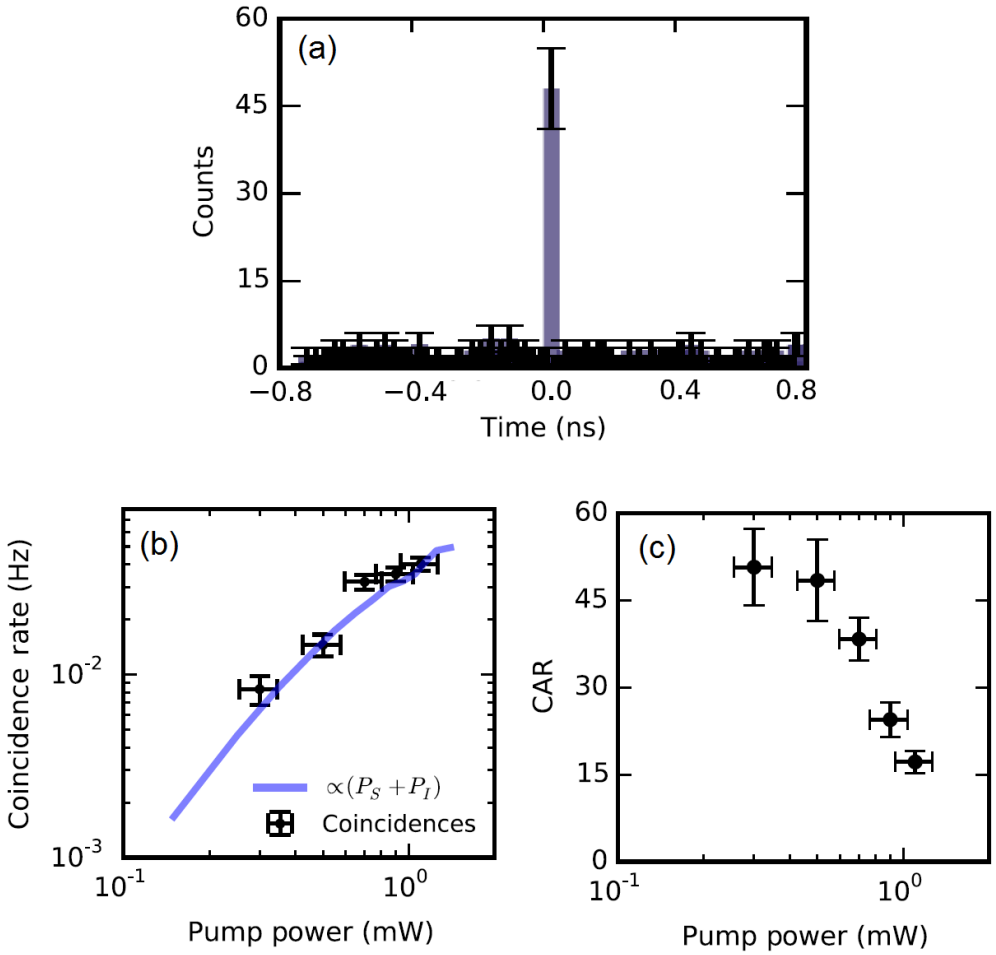

Figure 4.18: Results of the correlation measurements. (a) Histogram resulting from a coincidence measurement, where each time bin has a a temporal width of about 70 ps. It is clearly visible a coincidence peak at zero time delay, which is a proof of time correlation between signal and idler photons. (b) Coincidence rate as a function of pump power. Black crosses are single experimental measurements, while the light blue line is proportional to the coincidence rate of generated photons in the first experiment, rescaled for better clarity. (c) Coincidence-to-accidental (CAR) ratio as a function of pump power: it is well above the classical limit of 2, ensuring that our source is generating non-classical states of light.

The losses on the detected coincidences are 75.28 dB, as obtained from the count of the total losses reported in table 4.1. In order to estimate the losses, we summed up the losses of each section in the optical path of photons from the generating ring to the detectors. The loss of 5 dB for input/output and output coupling is due to the grating couplers response, while a directional coupler placed just after the in-coupling grating, designed to monitor the alignment of the sample, gives a contribution to attenuation of 1 dB. We measured a loss of about 5 dB for the path from the generating ring through the Bragg reflector and the following beamsplitter used as a spectral monitoring tap: the loss of 3 dB reported in table 4.1 is obtained subtracting, from the 5 dB, the losses of other components that were part of the measurement loop. We measured 1.5 dB loss for the add drop filters. The two SSPD have 10 % and 5 % efficiencies, leading to a loss of 10 dB and 13 dB, respectively. The estimated total losses are 36.14 dB for signal photons and 39.14 dB for idler photons. The loss on the coincidence rate is given by the sum of the losses on both channels, and here we estimate a loss on the coincidence rate of about 75.28 dB.

By taking the ratio between the coincidence rate in Fig. 4.18 (a) and the estimated internal generation rate extracted from Fig. 4.13 we obtain a measured loss of 79 dB. This slight discrepancy can be due to a better alignment of the grating couplers when measuring the dependence from power with respect to the alignment for the coincidence measurements. For instance this could be due to a drift of the piezoelectric controllers of the fiber array position. We want to notice that many losses can be reduced by modifying the design of the sample and with technology advancements, for example by using detectors with higher quantum efficiencies or couplers with improved designs.

Finally, the determination of the coincidence to accidental ratio (CAR) is very important to evaluate the quality of a source of correlated photons [142, 87, 190]. A definition of CAR can be obtained as the ratio between the number of time-correlated photons in the coincidence peak, with respect to the average number of accidental photons, constituting the background, that are recorded in the same time window [47, 25]. A useful expression for CAR is given by [87]

$$\mathrm{CAR} = \frac{\mathrm{CC}}{\mathrm{AC}} = \frac{1}{\beta \Delta t} \tag{4.1}$$

from which is evident that the ratio between the coincidence (CC) and accidental (AC) counts is inversely proportional to the generation efficiency β and the time window of the detector Δt. However, this relation holds only if losses and detection efficiency are the same for signal and idler, and as far as the time window is larger than the coherence time of the emitted photons, that in our case depends from the ring resonance. Furthermore, the value of CAR is expected to decrease as the inverse of the generation rate, and thus quadratically with pump power [87].

The graph reported in Fig. 4.18 (c) shows the CAR for our coincidence measurement, as a function of the pump power coupled into the generating

ring. The classical limit of CAR is 2, and we could overcome the classical value by more than one order of magnitude, achieving a CAR of 50±6, as can be seen also in Fig. 4.18 (b) relatively to a coupled pump power of 0.3 mW. This result allows for a high-fidelity preparation of entangled photon pairs or heralded single photons. However, some practical considerations have to be made. In fact, in our experiment the value of CAR is affected by the unbalancing between the detection efficiencies for signal and idler: in fact, even if in principle CAR should not depend on detection efficiency, in our case we expect an amount of detected signal photons that is the double of detected idler photons, resulting in an effective increase of accidental ratio. On the other hand, we expect a minimum contribution from the time resolution of the SSPD detectors (65 ps), which is on the same order of magnitude of the coherence time of generated photons, estimated to be around 30 ps for the considered microrings pumped with a cw laser. Another possible factor that could be limiting the measured CAR could be given by a not complete filtering of the pump, which could result in an increase of the accidental counts.

4.4.4 Conclusions

In the work described in this chapter we successfully demonstrated a monolithic and tunable source of correlated photon pairs on an integrated silicon photonic device.

In the first reported experiment, we demonstrated that the pump laser can be in principle fully filtered on a single chip, enabling the possibility to integrate single-photon sources and detectors on the same chip. The filtering was achieved using passive elements like DBR and add-drop microrings. However, this achievement required lot of efforts and, to our advice, too many parameters to be controlled at the same time. We believe that the performance of a single chip could be drastically improved by adopting some *tricks* in the design of the sample. For instance, more detailed experimental studies on the integrated DBRs could clarify if a larger number of periods could allow to reach the necessary rejection. One could also verify if a larger separation, or even the introduction of trenches, between the grating couplers could lead to a better performance of the DBR. Furthermore, another practical problem that we had to face is the deterioration of the add-drop resonances during the thermal tuning, due to injected carriers. This, in fact, forced us to search for samples where the add-drops resonances required a minimal tuning. This could have been avoided if the thermal tuning of add-drops was achieved with the same mechanism used for the generating rings, that would have allowed for a good extraction of idler and signal photons, regardless of the initial positions of their resonances. Another difficulty was bound to the instability in the response of the samples when tuning many parameters at a time and working at temperatures beyond the room temperature. To avoid this problem, we had to elaborate some practical solutions, like the installation of a Peltier element under the sample to control its temperature, and of an external box to limit

the air fluctuations in the surrounding environment.

Despite these issues, we were also able to perform a second experiment, where the generated photons, partially filtered, were transmitted to a second device, where the pump was completely rejected and signal and idler photons were routed on different output channels. Without the need of further external filters, we were able to measure photons pairs with generation rate above 1 MHz and time correlation with a CAR of 50, ensuring us the non-classical properties of the generated light. Even if it was not measured in this experiment, it has been shown that SFWM the same kind of resonators allow to produce time-energy entangled photons [191]. We believe that our architecture represents a promising road to integrated quantum optics, with applications like fully integrated QKD emitters and receivers based on time-energy entanglement protocols [192], or realization of boson sampling with heralded photon pairs [193]. Another remarkable aspect of our experiment is that the source has been fabricated with a CMOS compatible photonic process with a total footprint below 1 mm^2, allowing high reproducibility, scalability and possibility of high density integration.

Among some recent advancements in the integrated filtering, the work by Matsuda et al. demonstrated partial on-chip filtering [194], but requiring additional external filters to achieve the rejection necessary to suppress the pump. As pointed out also in [34], the integration of filtering and routing is a challenge still to be solved for integrated photon sources, and our work, being the first reported case of full on-chip filtering and routing of correlated photons, can be considered indeed a very promising solution. Another implementation of on-chip filtering and routing that is worthwhile to be mentioned, based on silicon photonic crystal cavities, has been recently proposed [195].

Chapter 5

JSD: characterization of the quantum state

As discussed and experimentally shown in the previous chapters, silicon integrated optical devices, such as microring resonators, are very promising sources of quantum correlated photon pairs based on spontaneous four-wave mixing (SFWM). In a theoretical work by Helt et al. [50] it has been suggested that by only changing the coherence properties of the pump excitation, one can in principle control the spectral correlations of the generated pairs, ranging from nearly uncorrelated to highly correlated photons. In fact, when using a pump laser with a long coherence time, i.e. with a narrow linewidth, the conservation of energy in the process implies a strong energy correlation between the generated photons. On the contrary, when using a laser with a short coherence time, i.e. with a broader linewidth, the constrain of energy conservation is somehow relaxed, in the sense that the energies of generated photons are bound from a whole set of energies comprised into the pump spectrum, resulting in photons with low energy correlation. In the case of energy correlations, highly spectrally correlated photons result to be in an entangled state, while indistinguishable heralded single photons can be obtained from spectrally uncorrelated pairs, without the need for additional filtering stage. This capability to produce non-classical states of light for different applications, along with the possibility of mass production of integrated optical circuits, suggests the development of fast and reliable techniques to quickly characterise the quantum properties of these devices. This is a challenging task, as it requires the reconstruction of the biphoton wavefunction, which describes all the properties of the generated pairs in the energy Hilbert space. In the assumption that the generated state is pure, one can determine the presence of energy correlations by measuring the Joint Spectral Density (JSD), i.e. the squared modulus of the joint spectral amplitude, describing the pair. In microring resonators, JSD measurements are very challenging, for photon pairs are generated within a bandwidth of few tens of picometers, determined by the linewidth of the resonances. This task is well beyond any coincidence-based technique ever

implemented, both for what concerns spectral resolution and duration of the measurement. In this chapter, we demonstrate that the characterization of the JSD of photon pairs generated by SFWM can be obtained by studying the corresponding Stimulated FWM, with unprecedented resolution and fast measurement. This chapter will start with an introduction to the Joint Spectral Density. The sample under study, which is based on the same OpSIS architecture reported in chapter 4, will be described, and we will report about the linear characterization and preliminary SFWM measurements. Then, we will describe the set-up for the measurement of JSD, focusing in particular on the custom made tunable Fabry-Pérot filter that have been realized in order to achieve the resolution necessary to resolve the linewidth of the resonances. Finally, the results of JSD measurements will be discussed and compared with the predictions based on numerical simulations.

5.1 Introduction to the measurement of JSD

As already discussed in sections 2.3.3 and 2.3.4, FWM process can be either spontaneous, that can be described only by quantum mechanics, or stimulated, that can be also understood classically. Einstein famously linked spontaneous and stimulated emission, writing down the relations between the coefficients A and B in the well known Einstein's equations [11]. What is interesting to our purposes is that while spontaneous emission can be difficult to measure, stimulated emission is generally easier to perform, because one deals with classical fields and doesn't need single photon detection. In this sense, Einstein's relations are at the basis for the core idea of our measurement of JSD: exploiting a classical phenomenon in order to efficiently study its quantum counterpart. The analogous of Einstein's relations between spontaneous and stimulated emission have been derived for SFWM and FWM [196]. The principle is inspired to that of stimulated emission tomography [197], and there are already experimental proofs that the characterization of quantum states can be carried out exploiting the corresponding classical effect [198, 199].

A useful relation provides a link between the number of photons generated in the stimulated process and the number of photons that would be generated in the corresponding spontaneous process, with a proportionality constant that is about the average number of photons in the stimulating field. Such relation can be expressed as [197]:

$$\frac{\langle n_{\omega_i} \rangle_{A_{\omega_s}}}{\langle n_{\omega_i} n_{\omega_s} \rangle} \approx |A_{\omega_s}|^2 \tag{5.1}$$

where $\langle n_{\omega_i} \rangle_{A_{\omega_s}}$ is the average number of generated idler photons at frequency ω_i, stimulated by a signal seed at frequency ω_s, $\langle n_{\omega_i} n_{\omega_s} \rangle$ is the average number of photons that would be generated in the corresponding spontaneous effect, and $|A_{\omega_s}|^2$ is the average number of photons within the coherence time of the stimulating signal.

Let's consider the quantum state $|\omega_s, \omega_i\rangle$ describing two photons at frequencies ω_s and ω_i. The bi-photon wavefunction describing the pair generated by a parametric process (SPDC or SFWM) can be derived from a standard perturbative approach [200], and, ignoring the vacuum component, can be expressed as

$$|\psi\rangle = \iint d\omega_s d\omega_i f(\omega_s, \omega_i)|\omega_s, \omega_i\rangle, \tag{5.2}$$

where $f(\omega_s, \omega_i)$ is the joint spectral amplitude of the two photons and $|\omega_s, \omega_i\rangle$ is the quantum state with signal photon at frequency ω_s and idler photon at frequency ω_i. The JSD is defined as the squared modulus of the joint spectral amplitude, i.e.

$$\text{JSD} = |f(\omega_s, \omega_i)|^2 \tag{5.3}$$

and allows one to obtain information about the quantum correlation of the generated photons [198, 201]. The two-photon spectral state $f(\omega_s, \omega_i)$ is completely determined by the spectral amplitude of the pump laser and phase-matching function, while the JSD, being its squared modulus, does not bring information about the phase, and can be interpreted instead as a probability density. Its measurement is traditionally based on spectrally resolved coincidence measurements, characterized by long measurements time and low resolution [202, 203]. This is particularly demanding for ring resonators, given their narrow generation bandwidth. State-of-the-art techniques based on coincidence measurements do not have sufficient resolution to investigate spectral correlations of photon pairs generated in such devices. Doing it by directly counting the photons generated in the spontaneous process would result in complicated and time consuming measurements. In fact, it would require to spectrally filter the generated photons with very narrow bandpass filters, thus reducing the output intensity, and to reveal them with two single photon detectors. The coincidences between the detectors are recorded in an histogram, analogously to what reported in 4, and each coincidence measurement will result in a single pixel of the JSD diagram. It means that, to achieve a good resolution, for example of 50 $\times$ 50 pixels, this must be repeated thousands of times. On the contrary, exploiting the stimulated process instead of the spontaneous one, would lead to intrinsically much stronger emission and resulting into very high signal-to-noise ratios, thus allowing to perform fast and highly resolved two-photon state characterisation [196, 198, 199]. For this reason, we developed a measurement technique based on stimulated emission, where the detected signal is much more intense than the one obtained from coincidence measurement between spontaneous events.

5.1.1 Schimidt number

One of the first theoretical works studying SFWM in microring resonators showed how the principle that we just mentioned can be applied to this struc-

ture. In fact, in [50], the spontaneous generation of photon pairs could be predicted from the rate of stimulated emission, and it was also suggested that the biphoton wavefunction can be controlled by changing the coherence time of the pump laser.

Schmidt decomposition technique [204] is commonly used to obtain a complete characterization of the existing entanglement between the photons constituting the pair [24, 205]. The method basically consists in the decomposition of the joint spectral amplitude, finding a bi-orthogonal system u_n, v_n such that $f(\omega_s, \omega_i)$ may be expressed with the following expansion

$$f(\omega_s, \omega_i) = \sum_{n=0}^{\infty} \sqrt{\lambda_n} u_n(\omega_s) v_n(\omega_i) \tag{5.4}$$

where $u_n(\omega_s)$ and $v_n(\omega_i)$ are Schmidt modes, i.e. eigenvectors of the reduced density matrices for the signal and idler photons, with corresponding eigenvalues λ_n. The mode functions u_n, as well as v_n, form a complete and orthonormal set. The decomposition reported in equation (5.4) provides the information about the eigenstates of the two-particle system. The amount of spectral entanglement may be quantified, for istance, by the degree of non-separability of $f(\omega_s, \omega_i)$, that is usually discussed in terms of entropy of entanglement, defined as [24]

$$S = -\sum_{k=0}^{\infty} \lambda_k log_2 \lambda_k. \tag{5.5}$$

If the two-photons are not frequency correlated, $f(\omega_s, \omega_i)$ is completely factorable and the entropy of entanglement will be equal to zero. The spectral entanglement, and so the correlation between signal and idler frequencies, will be proportional to the number of terms on the right-hand side of equation (5.5). Another quantity that is often considered in literature to *quantify* entanglement is the Schmidt number K, which is the average number of Schmidt modes involved, defined as [205]

$$K = \frac{1}{\sum_n \lambda_n^2}. \tag{5.6}$$

Small values of K correspond to low correlation, the lower possible value being $K = 1$ for totally uncorrelated (disentangled) photons. Two-photon states can have many Schmidt modes, with the general trend that high values of K correspond to strong entanglement. The maximum value of K depends on the total volume of phase-space that is accessible to the system under constraints, such as conservation of energy and momentum.

We reported here the general approach, while for more details about the case in which we are interested, i.e. the calculation of Schmidt number for time-energy correlated photon pairs generated by SFWM in silicon microrings, we refer to [50].

5.2 Experimental set-up

Before entering into the real JSD measurement, this section will be dedicated to a description of the sample and of the experimental set-up used for the characterization and for SFWM measurements.

5.2.1 Sample layout and characterization

The sample is fabricated with the same standard CMOS-compatible silicon photonics fabrication process described in section 4.1.1: analogously to the samples described in chapter 4, it was realized by OpSIS and is part of a multi-project wafer. In Fig. 5.1 (a) a detail of a top view of the chip that includes the source used in this experiment is shown.

The source is a 15 μm radius microring resonator, critically coupled to a straight silicon ridge waveguide, with thickness of 220 nm, width of 500 nm, and a total length of about 900 μm. A nonuniform focusing grating coupler is intended to be used to couple light into the waveguide by means of a fiber array aligned above the sample, as already described in section 4.1.1. As can be seen from Fig. 5.1 (a), the waveguide ends with an edge coupler, from which the light going out of the sample can be collected by means of a polarization maintaining (PM) tapered fiber aligned to the end of the straight waveguide. The coupling at the edge of the sample is provided by an inverse taper, obtained by a progressive shrinking of the waveguide width from 500 nm down to 220 nm: this was designed to match the mode of the waveguide with that of the tapered fiber used to collect light out of it, in order to increase coupling efficiency. The spectral response of the edge coupler is much flatter, along a wide wavelength range, with respect to that of the grating coupler. Considering this, since we intend to study correlation of photons generated in different spectral positions, we decided to use the grating coupler as input and the edge coupler as output.

Analogously to what described in section 4.2.1, the sample is mounted on a translating and rotating stage, 3-axis translators with piezoelectric allow to finely adjust the position of the fiber array, and a microscope with visible cameras above and at the sides of the sample are used to help in the alignment operations. The difference from the set-up reported in section 4.2.1 is that in this case we don't need to tune the resonance of the microring, so the heaters are not employed, and the metallic tips have been replaced with the out-coupling tapered fiber, mounted on a triple-axis translator. This difference can be noticed from the photo in Fig. 5.1 (b), where the sample is visible, together with the input and output coupling fibers.

The set-up for transmission measurements is analogous to the one reported in section 4.2.1. For fast alignment operation, we used in fact a broadband diode laser as a source, and the spectrometer coupled to the CCD camera for detection, while for high resolution spectra, as the one in Fig. 5.2, a tunable laser in scanning mode (Santec TSL-510) and an InGaAs detector (Newport

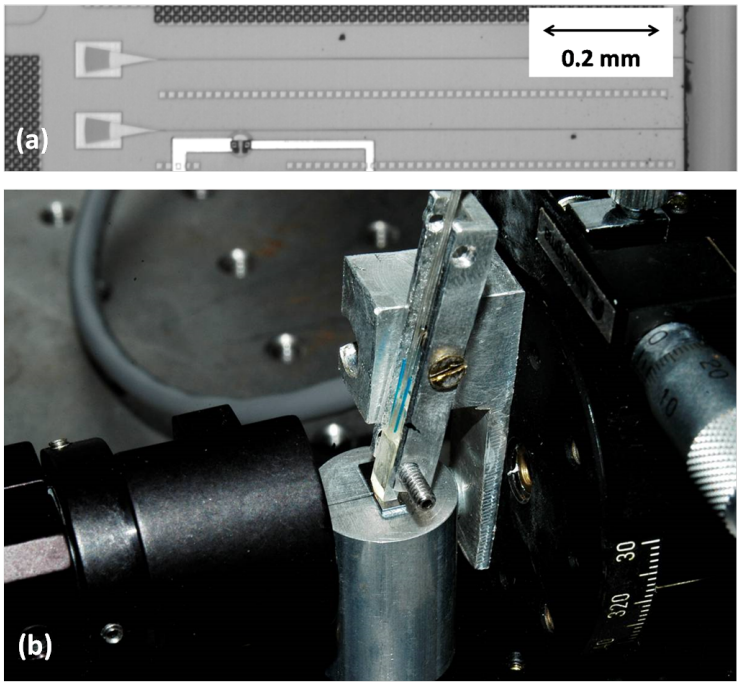

Figure 5.1: (a) Micrograph of the sample used in this experiment, constituted by a 900 μm-long silicon waveguide, with a microring resonator with a radius of 15 μm critically coupled to it. The grating coupler is used for coupling light into the waveguide, which is interrupted at the edge of the sample: the output must be collected with a tapered fiber aligned to the side coupler. The upper waveguide, without microring resonator, has been used as a reference to determine insertion losses. (b) Photo of the sample, placed on top of an aluminum support, mounted on a rotating stage. The side-coupled tapered fiber is visible on the left, while the fiber array, with almost vertical orientation, is placed above the sample.

918D-IG-OD3) with a powermeter were employed.

Linear characterization

During preliminary alignment operations, the angle of the fiber array is adjusted in order to optimize the transmission spectrum, as well as the position of the tapered fiber.

Fig. 5.2 shows the measured transmission spectrum of the structure under investigation (black line), together with the transmission of a reference waveguide, without resonator (grey line). In both cases, the bell shape of the transmission is due to the spectral response of the grating coupler (see section 4.2.2). The labels next to the transmission dips are indicating the resonances that have been chosen to carry out the SFWM experiments: the pump resonance is the one in correspondence of the maximum transmission. This choice turns out to maximize the generation efficiency, given its quadratic dependence from pump power. The two adjacent resonances, which are still in the region of high out-of-resonance transmission, are chosen as idler and signal for the FWM experiment.

Since the spectrum in Fig. 5.2, having a resolution of about 5 pm, does not allow to appreciate the profile of the resonances, we report in Fig. 5.3 a spectrum with resolution of 2 pm, showing the resonances of idler, pump and signal that are used in the SFWM and FWM experiment. From spectra in Fig. 5.3 it is clearly visible that the ring resonator is at critical coupling condition, since the transmission at resonance drops to zero. From a fit of the dip resonances with a lorentzian function we were able to determine a linewidth of about $\delta\lambda \approx 40$ pm and a central wavelength of 1552.51 nm. Applying to the measured linewidths the relation for the extraction of Q factor from the resonance parameters (2.15), we found an average quality factor of about $Q \approx 4\times10^4$. In particular, for the pump resonance, we have $Q_p = 40800\pm2000$, corresponding to a coherence time of

$$\tau = \frac{1}{\Delta\omega} \approx (33 \pm 2) \text{ ps}, \tag{5.7}$$

which is the dwelling time of the photons inside the resonator. The average free spectral range (in wavelength domain) of the resonator was determined to be 10.1 nm.

5.2.2 SFWM measurements

After the preliminary linear characterization, we performed spontaneous four-wave mixing (SFWM) measurements in two different regimes: for the long coherence time regime, we used a cw laser (Santec TSL-510) while for shorter coherence time we used a pulsed laser (Pritel FFL), both tunable and working in the infrared range, around 1.5 μm. A schematic picture of the experimental set-up is shown in Fig. 5.4 where the pump laser, filtered with a bandpass (BP)

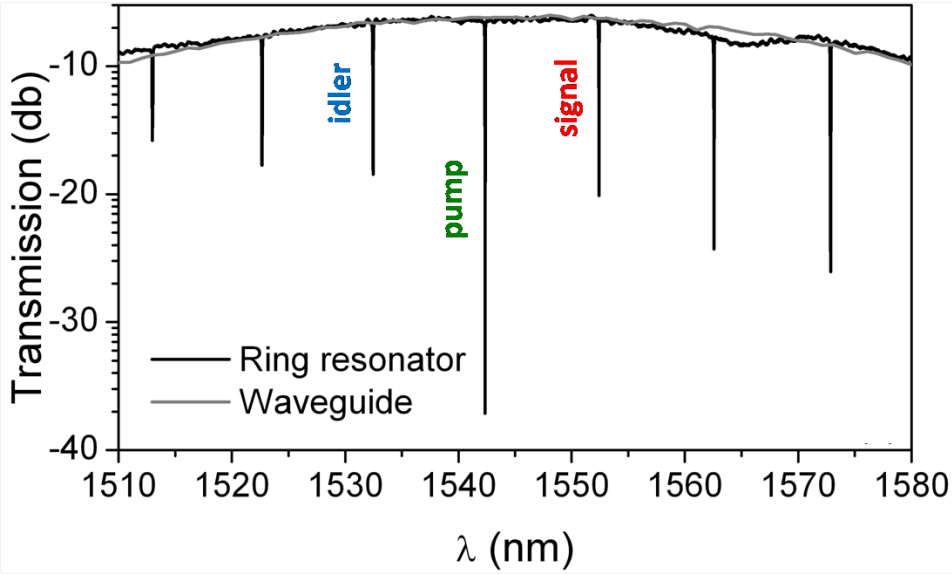

Figure 5.2: Transmission spectrum of the sample (black line) and of the reference waveguide (grey line). The resonance chosen as pump is at the wavelength with maximum transmission, while the two adjacent resonances are chosen as signal and idler. Spectral resolution is 5 pm.

filter to clean out sidebands, is used to excite the sample. The outcoming light is filtered with external BP filter centered at the idler (or signal) wavelength, with high extinction ratio, in order to reject the transmitted pump laser and SFWM emission from other resonances of the ring. The filtered idler (or signal) is then sent to the detection system, constituted by a spectrometer (Acton Spectra Pro 2500i) coupled to a liquid-nitrogen cooled CCD camera (Acton InGaAs OMA V). The spectral resolution with this measurement is of about 70 pm, and id limited by the resolving power of the diffraction grating of the spectrometer and to the size of the pixel of the CCD camera used for detection. We want to notice that this resolution is larger than the linewidth of the resonances of the ring (measured to be about 40 pm), thus is not sufficient to resolve the shape of the spectrum of the generated photons. This is the reason why we had to develop an instrument with higher resolution, as will be described in section 5.3.2.

Experimental result of SFWM

The spectra obtained from a SFWM measurement are shown in Fig. 5.5. Here, the sample has been excited with a pulsed laser (Pritel FFL) tuned in correspondence to the central wavelength of the pump resonance λ_p, with an energy of 0.8 pJ per pulse and a repetition rate of 10 MHz. In the graph reported in Fig. 5.5 both generated idler (blue line) and signal (red line) are shown, which have been measured in two different acquisitions, tuning

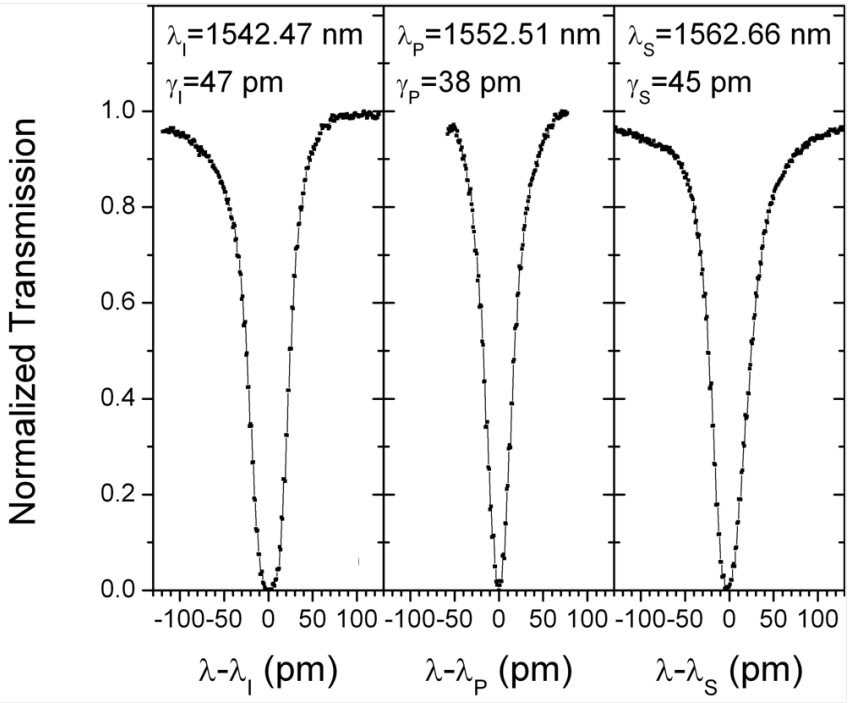

Figure 5.3: Detail of the transmission spectrum with higher resolution (2 pm) for the resonances used as idler, pump and signal for the FWM experiment. Black dots are experimental data, while the line is the result of the best fit with a lorentzian function.

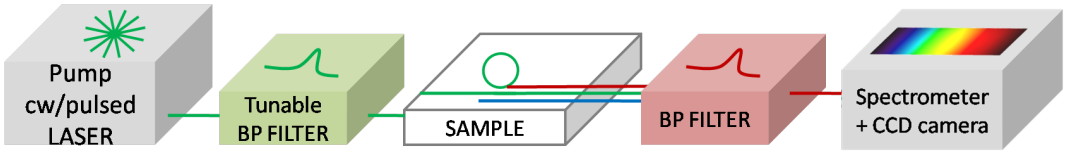

Figure 5.4: Schematic picture of the experimental set-up for the SFWM measurement. The sample is excited by a cw or pulsed pump laser, spectrally cleaned by a bandpass filter. The light coming out from the sample undergoes a filtering stage to reject the pump and the photons generated at other wavelengths. Since the FSR of the microring is about 10 nm, a filter with a bandwidth narrower than 10 nm had to be used.

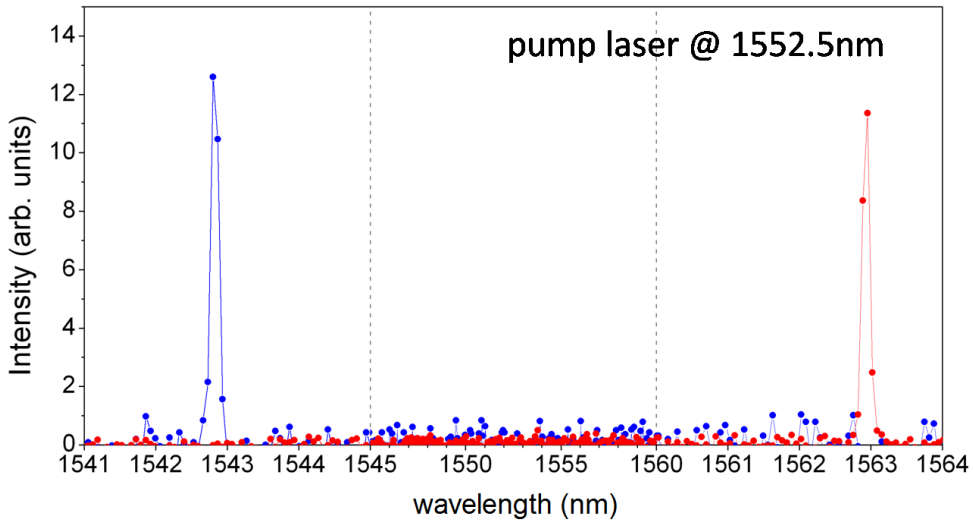

Figure 5.5: Example of a spectrum obtained from a spontaneous FWM measurement with pulsed pumping, showing the generated idler (blue line) and signal (red line). The pump field is not visible as it is completely rejected by external filters. The experimental points are connected with a line for a better visualization of the spectrum. Detection system is a spectrometer coupled to a CCD camera, with a spectral resolution of about 70 pm: the shapes of the resonances are not resolved.

the center of the BP filter in correspondence of either the idler or the signal resonance. The scale in the central region is shrinked in order to have more resolution on the peaks generated by SFWM. We then carried out the same SFWM measurements in the cw regime, replacing the pulsed laser with a cw laser, with a result that is analogous to the one reported in Fig. 5.5.

In order to have a more complete analysis, we report also the dependence of generated photons from pump power. In particular, Fig. 5.6 (a) shows the idler (blue circles) and signal (blue circles) photon generation rate, obtained with cw pump, as a function of coupled pump power. Fig. 5.6 (b) shows the result of the same experiment performed with pulsed pump, where the average number of generated idler (red circles) and signal (blue circles) photons per pulse as a function of the pulse energy is reported. In both graphs, a dashed line is representing a quadratic dependence, that allows to quickly visualize that the quadratic trend, expected from the theory of SFWM, is confirmed with both cw and pulsed pumping. This is demonstrating that linear parasitic processes (Raman scattering or photoluminescence) are not influencing the measurement. For a coupled pump power above 100 μW for the cw case, or above 1 pJ per pulse in the pulsed case, a saturation effect is visible, due to ring bistability bound to refractive index change consequent to two-photon absorption [41].

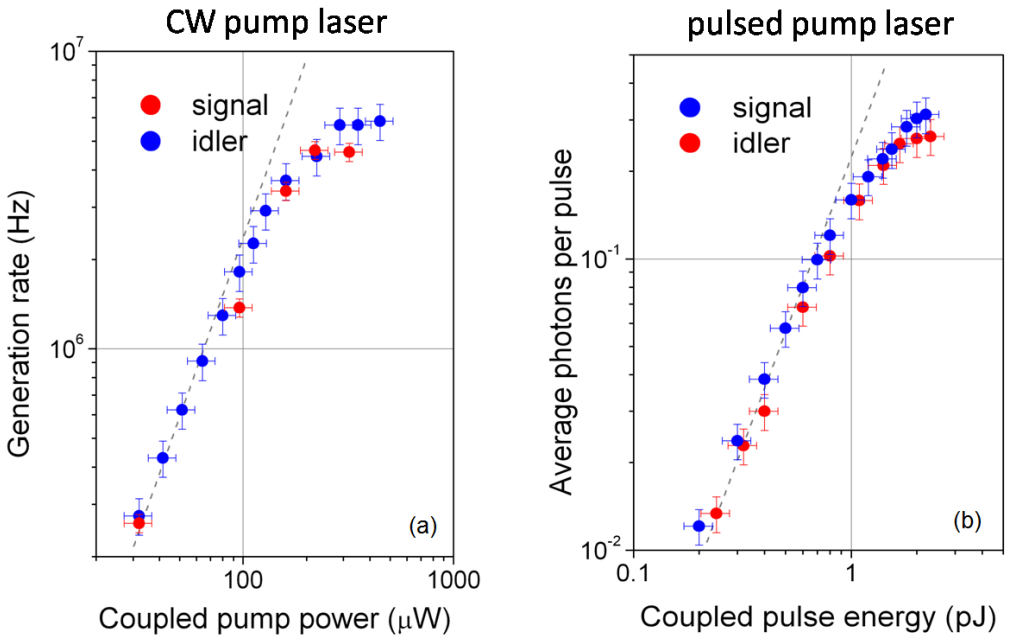

Figure 5.6: (a) Dependence of the generation rate of signal and idler from coupled pump power, in the case of cw pumping. (b) Average number of generated photons per pulse, as a function of coupled energy per pulse, in the case of pulsed pumping. In both graphs, the dashed line is a quadratic dependence. Coupled powers (generation rates) have been estimated measuring the input (output) power and taking into account for propagation losses, that in our case turn out to be negligible, and coupling losses. Horizontal error bars are due to a 10% uncertainty in the estimation of the coupled pump power, while vertical error bars are the squared root of the measured number of photons per second (a) or per pulse (b).

Coupled pump powers have been estimated from a correction of the pump power measured right before the sample, taking into account for coupling losses from the grating coupler, that have been measured to be around 5 dB (see section 4.2.2). Propagation losses can be considered negligible, since the waveguide has a total length of less than 1 mm and reported propagation losses are on the order of 3 dB/cm. The internal generation rate has been estimated measuring the output power of generated signal and idler with an InGaAs detector, and taking into account for coupling losses and for losses along the photon path. The generation rates reported in our results are comparable with that obtained by similar structures [49, 53].

5.3 Measurements of JSD

In this section we will discuss in detail the JSD measurement, performed in order to characterise the spectral correlations of the photon pairs generated in the microring by SFWM. The measured JSD gives in practice the signal wavelength as a function of the idler wavelength, and vice versa. If one wanted to do it with a coincidence measurement on spontaneously generated photons, for each wavelength comprised in the signal resonance one should have to record all the wavelengths inside the idler resonance: depending on the wanted resolution, very narrow spectral filters may be necessary, resulting in very long measurement time. However, as already explained in the first section of this chapter, the JSD can be obtained more efficiently exploiting the stimulated process. In this case, the effect is stimulated by a seed laser, scanning along the wavelength range of the signal resonance. The spectral resolution on the signal resonance is given by the minimum scanning step of the cw seed laser. The generated idler photons, instead, have to be filtered with a tunable band pass filter (BP), that must be narrow much narrower than the linewidth of the idler resonance, since it must be used to sample the photons generated at different wavelengths inside the idler resonance. We will describe first the experimental set-up, focusing in particular on the FP filter and on the feedback mechanism used to control it.

5.3.1 Experimental set-up for JSD measurement

The JSD measurement involves the excitation of a resonant mode of the microring using a pulsed (cw) pump laser, with short (long) coherence time, while a tunable cw laser is used to excite the signal resonance, providing the seed for the stimulated FWM. Keeping the pump wavelength fixed, we could scan all the wavelengths comprised in the signal resonance by tuning the cw seed laser. On the other side, in order to sample the generated idler photons, we used a custom-made Fabry-Pérot interferometer as a scanning tunable filter. From a more practical point of view, in order to minimize the movements of the FP filter, the seed laser scans along the signal resonance wavelength

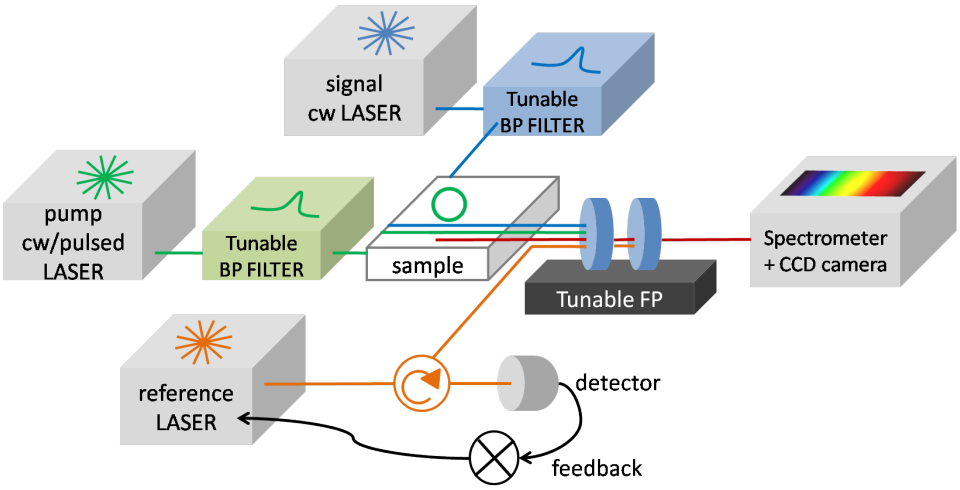

Figure 5.7: Experimental set-up for JSD measurements. Two tunable infrared lasers are spectrally cleaned by Band Pass filters (BP), combined in a beam-splitter (not shown in the image) and coupled to the sample. A custom built tunable Fabry-P'erot interferometer (FP) is used to filter the generated idler resonance with the wanted spectral resolution. The FP filter is stabilized and controlled by means of a reference laser operating in a different wavelength range (around 1.3 μm) that is sent to the FP interferometer through a circulator so that its reflection can be collected by a detector and used in an active feedback loop. The output from the FP filter is sent to a spectrometer and a CCD camera where the filtered spectrum can be detected.

range for each fixed position of the FP (i.e. at fixed idler wavelength), and it is repeated for every wavelength comprised in the idler resonance. A more detailed schematic representation of the experimental set-up is shown in Fig. 5.7. The sample is pumped either with a pulsed (Pritel FFL) or cw (Santec TSL-210) laser as in SFWM but, in addition, a second tunable cw laser (Santec TSL-510), whose wavelength can be controlled with an accuracy of about 2 pm, is employed to stimulate the generation of photon pairs. Band Pass (BP) filters are used after each laser to get rid of the broadband background arising from amplified spontaneous emission (ASE) of the lasers. The signal and pump lasers are combined using a polarization maintaining 50:50 beam splitter, and one of the outputs of the beam splitter is sent to the input grating coupler of the sample. Outgoing light is collected at the sample output through a tapered fiber, and a home-made Fabry-Pérot filter is used to analyze the generated idler beam with a resolution of about 5 pm. The FP is made by two 90/10 fused silica beam splitters, mounted on translating stages, and controlled by piezo-electric actuators. The output of the sample is injected in the FP and collected back by two identical collimators.The tunable filter is actively stabilized by injecting an additional reference laser (around 1.3 μm) inside the FP through an optical circulator, so that the reflected light, that is in resonance with the

FP cavity, can be sent to a detector. The detection system communicates with the computer where a dedicated software with an active feedback mechanism controls the position of the mirror mounted on the piezoelectric translator. The working principle of the FP will be described in more detail in the next paragraph. The output of the Fabry-Pérot is then sent to the spectrometer coupled to the cooled CCD camera where the photons are detected.

We want to point out that one of the major difficulties in the experiment consisted of the control of the stability of the set-up. In fact, the duration of the measurement was on the order of one hour, during which the acquisition could not be interrupted, and even small changes in the temperature or vibrations could compromise the result. Thus, we found convenient to exploit the anti-vibrational system of the optical table, based on suspensions with compressed air. Furthermore, to have a better stability of the FP filter, we had to mount the optical elements on supports with a diameter larger than usual (more than 2 cm) and to build a plastic case surrounding the whole filter, since even small fluctuations in the air could lead to changes in the refractive index and thus to changes in the resonance wavelength. Given the high sensitivity of the FP to the environment we used also an IR camera, to which the transmission could be sent via a removable beam splitter, in order to periodically check the alignment condition and the shape of the transmitted beam. The same camera was also essential, during the first alignment operation, to achieve a regular shape of the spot, which allowed to set the two mirrors in parallel condition.

5.3.2 Tunable Fabry-Pérot filter

The FP consists of two parallel UV fused silica broadband beamsplitters (BS), placed inside two mirror mounts that are aligned to be parallel. Each mirror is mounted on a three axis translator, controlled in one direction by piezoelectric actuators to modify the spacing distance between the BSs. The output beam exiting from the sample is collected by a single mode fiber and collimated by an objective at normal incidence on the FP. The output of the filter is then focused on another fiber by a second objective, identical to the other one. The working range of the BSs is 1.2-1.6 μm and their reflectance is about 90% at an angle of incidence of 45°. The length of the FP, i.e. the distance between the mirrors, is set to about 5 mm, leading to a FSR of $\Delta\lambda \approx 240$ pm, as shown in the transmission spectrum of the FP reported in Fig. 5.8. The measured linewidth of the FP resonances is $\delta\lambda \approx 5$ pm, which is sufficient to sample the whole wavelength range of the idler resonance ($\sim$ 140pm) in about 30 points. The finesse of the filter is thus $\mathcal{F} = \Delta\lambda/\delta\lambda \approx 50$, higher than the one expected from the reflectance of the BSs, probably because of the different behaviour of the reflective coating at normal incidence. Considering the measured finesse, the filter rejection is about 30 dB, as confirmed by the transmission spectrum in Fig. 5.8. In order to stabilize the FP length against environmental noise and change the filter wavelength, we implemented a remotely controlled active feedback loop on the piezoelectric actuators, using

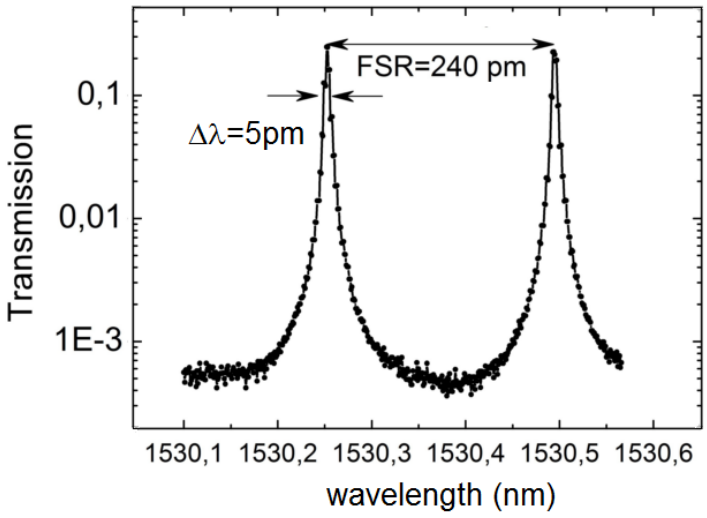

Figure 5.8: Transmission spectrum of the FP filter showing two adjacent resonances in the wavelength range of interest, from which its figures of merit can be deduced. In the configuration used for the experiment the linewidth is of about 5 pm, that will be the resolution on the idler wavelength, FSR is 240 pm and the extinction ratio is 30 dB.

a reference tunable laser. The reference laser and the generated idler beam are merged thanks to a fiber wavelength division multiplexer (WDM) placed right after the sample. The obtained multiplexed signal is sent to the FP, after which the reference beam is filtered out.

Active feedback mechanism

The active feedback acts analogously to the mechanism of stabilization of interferometers reported in [206]. Our feedback, however, gets a stabilization in wavelength instead of in phase. To do it a *dither*, i.e. a voltage with very small amplitude, is sent to the piezoelectric actuator which controls the position of the mirror. The optical modulation amplitude (OAM) will depend on the position of the control laser wavelength with respect to the FP resonance. In practice, given a transmission with a lorentzian lineshape, if the dither is described by $Acos(\omega t)$ the OAM is calculated as

$$OAM \propto \int L(cos(\omega t))cos(\omega t)dt \tag{5.8}$$

where L is the lorentzian function, and all the omitted parameters have to be set in order to get a stable feedback. It can be demonstrated that such a calculated OAM corresponds to the first order derivative of the FP transmission function, and it is linear across the resonance peak, as shown in Fig. 5.9, where the black line is the transmission spectrum of a resonance of the FP,

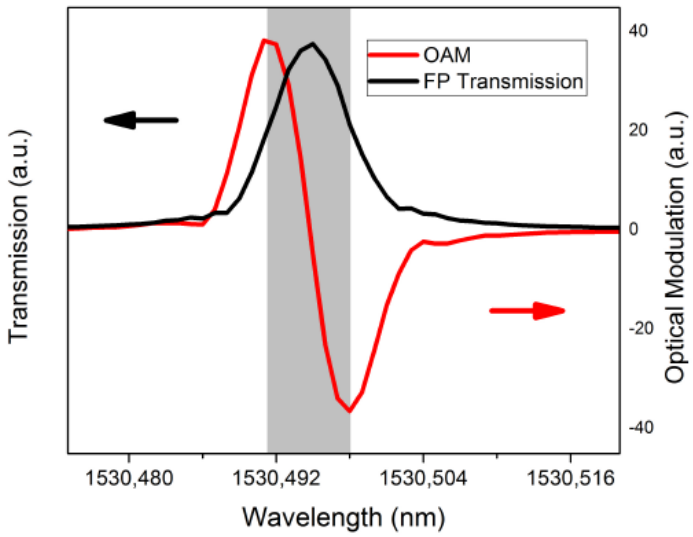

Figure 5.9: Scheme of the working principle for the active feedback of the Fabry-Pérot filter. Black line is the transmission spectrum of a FP resonance, measured with the laser in scanning mode, superimposed to the amplitude of the optical modulation (OAM) given by the dither, represented by the red line. The grey region highlights the linear part of the OAM, used as error function for the active P.I.D. feedback. The parameters of the P.I.D. algorithm can be set from a dedicated software allowing to adjust the speed of the feedback in order to increase the stability of the interferometer.

and the red line is the OAM. Then, considering laser wavelengths inside the FP resonance, highlighted in grey in Fig. 5.9, the farther is the reference laser from the FP peak, the larger would be the value of the OAM. This means that the OAM can be used as the input error function for a P.I.D. algorithm, controlled by the computer, which sends a DC voltage feedback to the piezoelectric actuator. The feedback mechanisms allows to compensate for fluctuations in the position of the mirrors or in the refractive index fluctuations, and stabilize the FP resonance on the reference laser line. The amplitude of the dither is very small and does not perturb the FP output, so that we can stabilize the resonance wavelength with a precision of about one pm. The filter can be easily tuned by changing the wavelength of the reference laser, allowing to control the stabilization point and thus to tune the resonance wavelength of the FP.

5.4 Results of JSD measurements

In this section, the results of the JSD measurements and the calculated Schmidt number will be reported. First we consider the measurement with the pulsed laser, and then we will report the results for cw lasers. The results will be discussed and compared with theoretical predictions obtained by numerical simulations.

In Fig. 5.10 (a) the diagram resulting from the measurement of JSD with pulsed pumping is shown. All the control of the experiment is done by a dedicated Labview software, that was developed *ad hoc* for this experiment. The algorithm of the Labview software can be schematized as follows.

Control of the FP: the position of the BS of the FP interferometer, controlled by piezoelectric translators, is set to a condition such that one resonance of the FP falls within the spectrum of the idler resonance.

Stabilization of the FP, done by the feedback mechanism, exploiting the error function, derived from the reference laser reflected from the FP that comes out from the reflection port of the optical circulator (see Fig. 5.7).

Scan of the stimulating signal laser: this is performed acting on the software for the control of the tunable cw laser, used as seed. The signal is scanned for a fixed position of the FP (i.e. for a fixed wavelength inside the idler resonance) along the wavelength range of the signal resonance.

The software builds the image step by step, slightly increasing the idler wavelength at every iteration, and the diagram is built by finally putting together all the recorded spectra. Thus, an image like the one reported in Fig. 5.10 (a) represents the final output generated by the software, used both for the acquisition of the spectra and for the control of the FP filter.

One can have a more intuitive interpretation of the diagram shown in Fig. 5.10 (a) if imagines to cut the picture in vertical slices: each slice would be the spectrum of the idler photons generated in a narrow (ideally monochromatic) wavelength range, while varying the signal wavelength. The reciprocal holds if we imagine to cut it in horizontal slices: in this case we would obtain a spectrum representing the signal photons that would be generated at a certain wavelength, if the seed laser was scanning along the idler resonance instead of the signal resonance.

The resolution on the axis of the signal wavelength is given by the minimum step of the scanning laser used to stimulate the effect, which in our case is 2 pm. The resolution on the axis of the idler wavelength is given instead by the FWHM of the FP resonances, which is about 5 pm (see Fig. 5.8).

5.4.1 Results with pulsed pumping

In the case of pulsed pumping, the BP filter on the pump laser sets the pump linewidth to a width of 90 pm, corresponding to a pulse duration of 14 ps, with an energy per pulse of 0.8 pJ. We notice however that the pulse linewidth is larger than that of the pump resonance, thus the laser turns out to be filtered by the resonance profile.

The result of the JSD measured with pulsed pumping, represented in Fig. 5.10 (a), can be intuitively interpreted as a case with very low energy correlation, since while keeping the pump and the signal wavelength fixed, idler photons can be generated in a broad wavelength range, that is wide about the linewidth of the resonance, actually given by a convolution of the resonances involved in the process.

We can compare the experimental result with the theoretical result, which is reported in Fig. 5.10 (b). This was obtained from simulations based on the theory in [50], considering the following measured sample parameters:

ring radius	R = 15 μm
effective index	$n_{eff} = 2.54$
group velocity	$v_g = 116$ m/ps
group velocity dispersion	GVD = 1.84 m^2/ps

The simulation does not include the effect of slight broadening of the resonances due to two photon absorption, estimated to be around 10%, which turns out to be more pronounced when dealing with high peak powers, as in the case of pulsed pumping. Assuming a pure state, the determination of the full joint spectral density allows one to calculate the Schmidt number K, as described in section 5.1.1. From the theoretical model we found $K = 1.09$, which indicates nearly uncorrelated photons, as it is expected in this system when the pump pulse duration is equal or shorter than the dwelling time of the photons in the resonator [50], that from the measured linewidth of the

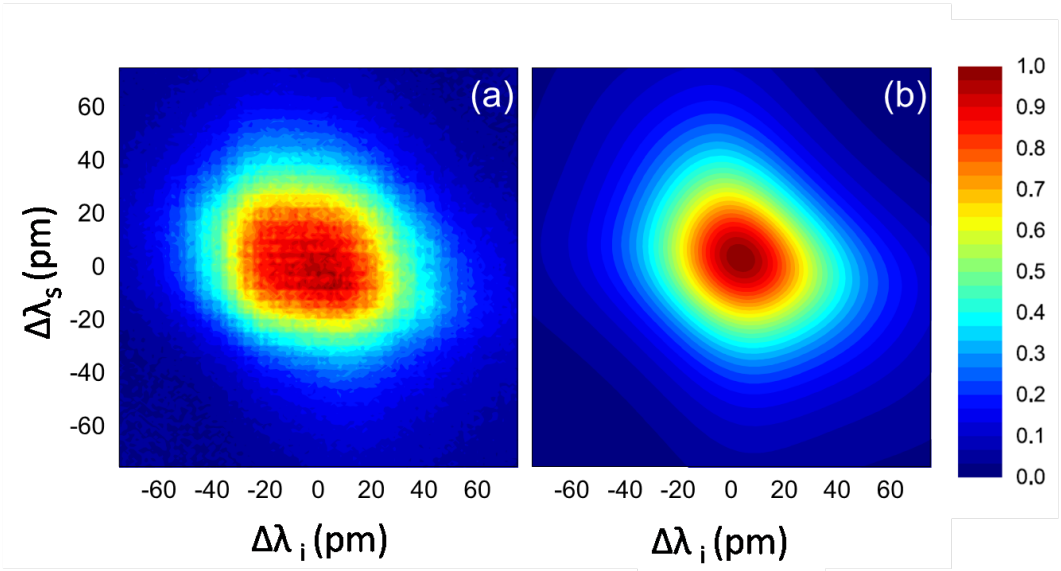

Figure 5.10: JSD measured under pulsed pumping. Figure (a) is the result of a measurement while (b) is the result of a theoretical calculation. The theoretical and experimental result are in very good agreement: one can notice in fact that, besides an overall resemblance, also small deviations from the circular symmetry in horizontal and vertical direction are visible in both results: these can be attributed to group velocity dispersion. Schmidt numbers extracted from the diagrams are $K_{bound} = 1.03 \pm 0.1$ for the experimental measurement (a) and $K = 1.09$ from the simulation (b). The colour scale is representing the normalized SFWM emission intensity, as can be seen from the colour bar.

pump resonance was determined to be of 33 ps. On the other hand, the experimentally obtained JSD allows one to determine a lower bound for the Schmidt number, that will be referred to as K_{bound}. From the data reported in Fig. 5.10 (a) a lower bound to the Schmidt number of $K_{bound} = 1.03 \pm 0.1$ was extracted: this result well compares with the expected theoretical value. The measured value is lower than the theoretical one, although within the uncertainty, due to the finite spectral resolution in the experiment.

5.4.2 JSD with cw pumping

In the second experiment the pulsed laser was replaced with a cw pump laser, for which the generation of entangled photon pairs has already been demonstrated [49]. The pump power inside the ring is estimated to be 80 μW. We report the measured JSD in Fig. 5.11 (a), along with the sketch of the result of the simulation, reported in Fig. 5.11 (b). The elongated shape of the measured JSD indicates high spectral correlations, that can be easily understood also from an intuitive point of view: in fact, once the pump power is fixed, the wavelength of the generated idler photons depend from the

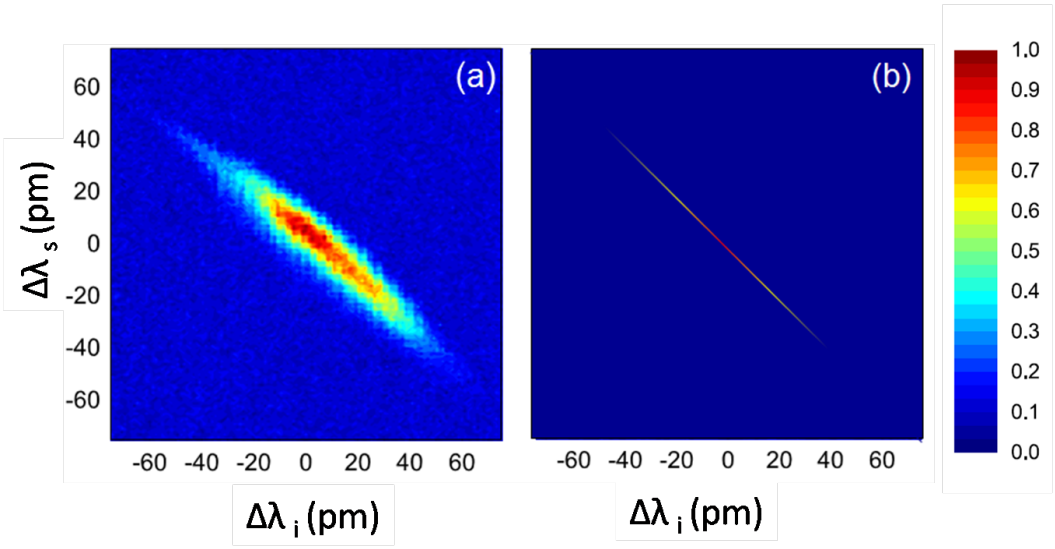

Figure 5.11: JSD measured with cw pumping. (a) is the result of the measurement while (b) is a sketch that represents the result of a simulation: the line would actually be so narrow that would not be visible. Calculated Schmidt numbers are are $K_{bound} = 3.93 \pm 0.1$ from the experimental measurement (a) and $K = 37038$ from the simulation (b). As in Fig. 5.10, the colour scale is representing the normalized SFWM emission intensity.

wavelength of the signal laser that is used to stimulate the effect. In this case the coherence time of the pump is about 1 μs, thus well above 33 ps, which is the dwelling time of the photon inside the resonator. This reflects on a theoretical Schmidt number of $K = 37038$: ideally, this condition should bring to strongly correlated photons. We point out also that the image shown in 5.11 (b) is not the actual result of a simulation, while it is just sketch, that was necessary because the line obtained from simulation was not visible since it was too narrow.

In this case, the discrepancy between the experimental and theoretical result is noticeable. In fact, the lower bound of the Schmidt number calculated from the experimental data is $K_{bound} = 3.93$. This value is limited by the experimental resolution, and in particular by the resolution given by the FP filter. However it should be noticed that, despite the lower bound in the case of cw pumping is much smaller than the expected Schmidt number, we are still able to clearly discriminate between the generation of correlated and nearly uncorrelated photons. In the specific case of a resonator with Q factor of about $4{\times}10^4$ this would not be possible to determine exploiting state-of-the-art techniques based on coincidence measurements, which have a resolution of hundreds of picometers. Indeed, if we consider the results of most recent works [196] a single pixel would be larger than the whole figure reported in Fig. 5.10 (a) or Fig. 5.11 (a).

We finally summarize the result in the table below, where all the Schmidt numbers derived from experimentally measured JSD (K_{bound}) and from simulation results (K) are reported, both for cw and pulsed pumping.

	τ_{pump}	K_{bound}	K
pulsed	$\sim$ 14 ps	1.03 $\pm$ 0.1	1.09
cw	$\sim 1\mu$s	3.93	37038

5.4.3 Experimental error on the Schmidt Number

The evaluation of K_{bound} has been performed as reported in [207], starting from the result of the experimental JSD. The uncertainty, due to signal-to-noise ratio and measurement resolution, depends on several parameters, and it can be different in the case of pulsed or cw pumping regime. Yet, since K is proportional to energy correlations, while the noise is uncorrelated in energy, the global effect of the noise is a reduction of K_{bound}.

Effect of resolution

In the case of SFWM in a ring resonator, one can assume that the biphoton wavefunction can be written as the product of two gaussian curves, having standard deviation σ_+ and σ_-, where $(\sigma_+)_\omega$ and $(\sigma_-)_\omega$ are the standard deviations along the direction $\omega_1 + \omega_2 = 2\omega_{p_0}$ and $\omega_1 - \omega_2 = \omega_{i_0} - \omega_{s_0}$, respectively [208], where ω_{p_0}, ω_{s_0} and ω_{i_0} are the center of the pump, signal, and idler resonance. In this case the Schmidt number is given by

$$K \approx \frac{(\sigma_-)_\omega}{(\sigma_+)_\omega} \tag{5.9}$$

that can be easily shown to be equivalent in the wavelength domain:

$$K \approx \frac{(\sigma_-)_\lambda}{(\sigma_+)_\lambda}. \tag{5.10}$$

where $(\sigma_+)_\lambda$ and $(\sigma_-)_\lambda$ in this case are the standard deviations in wavelength. The error associated to the calculation of the Schmidt number from the experimental results, comes from the uncertainties associated to the measurement of stimulated emission, which we can indicate as Δ_i and Δ_s on the idler and signal wavelength, respectively. Then, the error on $(\sigma_+)_\lambda$ and $(\sigma_-)_\lambda$ can be calculated by standard propagation error, as well as the error on the calculated K.

In the case of pulsed pumping, the experimental uncertainties of $\Delta_i = 2$ pm and $\Delta_s = 4.5$ pm are responsible for an error in the calculated K equal to $\Delta K = 0.1$. In the case of cw pumping, we observe that the value of $(\sigma_-)_\lambda$ is

limited by the setup resolution, in particular the expected standard deviation is

$$(\sigma_-)_\lambda \ll \sqrt{(\Delta_i)^2 + (\Delta_s)^2} \tag{5.11}$$

so that $(\Delta_i)^2 + (\Delta_s)^2$ is an upper bound for the expected $(\sigma_-)_\lambda$ that gives

$$K_{bound} > \frac{(\sigma_-)_\lambda}{(\Delta_i)^2 + (\Delta_s)^2} \approx 10. \tag{5.12}$$

This result is what one would expect for an ideal measurement, without noise, while in the real measurement with cw pumping we effectively found K_{bound} =3.9. The value is lower than expected, but still significantly larger than 1, which indeed indicates correlations. This huge difference can be however attributed to the noise in the measurements, which is uncorrelated and thus tends to strongly reduce the Schmidt number.

5.4.4 Conclusions

We have experimentally demonstrated that a microring resonator integrated on a silicon chip can be driven to emit nearly uncorrelated or time-energy entangled photon pairs depending on the coherence time of the pump laser. This has been done by exploiting FWM to directly and rapidly reconstruct the JSD of the generated photon pairs by the spontaneous process. Thanks to the high signal-to-noise ratio achievable in the stimulated process, we could spectrally filter the generated photons with a band pass filter of only few picometers width and avoid the use of single photon detectors. The resolution we achieved is less than 10 pm^2, which is more than two orders of magnitude better than state-of-the art measurements based on single photon detection, and still better then similar works that were carried out with stimulated PDC instead of FWM [196, 198, 199]. This resolution could be further improved by replacing the Fabry-Pérot filter with an Optical Spectrum Analyzers (OSA) with MHz resolution. We want to stress out that the measurement of the 2D spectra reported in Fig. 5.10 (a) and Fig. 5.11 (a) took about one hour of total integration time. Even though this could seem a long measurement time, it is incredibly shorter with respect to the time that would be needed in a typical experiment based on the spontaneous effects. In fact, in that case each pixel in the JSD diagram should be obtained from coincidence measurements between single photon detections of spectrally filtered spontaneously generated signal and idler photons. The use of very narrow bandpass filters, both for signal and idler photons, would lead to very low coincidence rate: depending on the needed spectral resolution, the measurement of a single coincidence peak, i.e. a pixel in the JSD diagram, can take several minutes. At this rate, performing a measurement constituted by thousands of pixels, as the one that we reported, would require a measurement time on the order of weeks, which indeed would be prohibitive.

We also want to remark that, even if in this experiment the filtering and routing has been performed with external filters, generation of photon pairs with full on-chip filtering of the pump and routing was achieved in the same kind of sample, as in the experiment reported in chapter 4. We believe the work reported in this chapter can represent a clear demonstration that stimulated FWM is a useful tool to implement fast characterization of integrated sources of non-classical states of light.

Chapter 6

Conclusions and perspectives

In this thesis, we reported on the results of experiments based on four-wave mixing (FWM) in silicon integrated microring resonators, with potential applications in disparate fields in the environment of integrated quantum photonics.

In the first work, described in chapter 3, we reported on the measurement of low-power stimulated FWM in porous silicon integrated microring resonators. The fabrication of the samples under study starts with the realization of a slab waveguide constituted by two porous silicon layers with different porosities, from which single-mode channel waveguides and microrings can be obtained with electron beam litography and reactive ion etching [166, 168]. We estimated that the high quality factors of the resonances that have been observed recently [122], could provide the field enhancement necessary to observe the generation of photons by stimulated FWM. In fact, from a first characterization of the samples it was found that, despite huge propagation losses, measured to be on the order of 27.5 dB/cm [122], it was possible to have a Q factor on the order of 5000, which is remarkable for a material with typically high scattering due to roughness.

In the experiment, a microring with radius 25 μm was excited by two lasers tuned in correspondence of the central wavelengths of two adjacent resonances, namely the pump and the signal, with pump power much more intense than signal power. We were able to observe the generation of a peak in correspondence of the position of the idler resonance, on the opposite side of the signal resonance with respect to the pump. A clear emission peak was obtained at the expected wavelength, even with low pump power, i.e. with an estimated power coupled in the resonator below 1 mW.

Since in porous silicon other emission processes, like Raman or photoluminescence [165, 156, 157, 163], could compete with the observed effect, we needed to prove that the observed peak was effectively FWM. To do this, we determined the power dependence of the generated peak with respect both to pump and signal powers. In fact, the quadratic dependence of idler power from pump power, and a linear dependence from signal power, can be consid-

ered as a clear signature of stimulated FWM. We were able to experimentally verify both these trends within the uncertainties, thus confirming that FWM was actually taking place. From each single measurement we were also able to estimate the nonlinear parameter of the porous silicon waveguides, resulting in an average value of $\gamma = 20 \pm 2$ W^{-1}m^{-1}. This is indeed in good agreement with previous results found in literature, and turned out to be an intermediate values between that of crystalline silicon and that of oxides [171, 172, 173]. Through the calculation of the effective area of the waveguide, we were also able to estimate the nonlinear refractive index to be $n_2 = (4.26 \pm 0.4)1 \cdot 10^{-18}$ m^{2}W^2, which is also compatible with results previously reported in literature.

This represents to our knowledge the first observation of enhancement of a nonlinear effect in porous silicon integrated microresonators. The result is indeed remarkable if we consider the high propagation losses of the material and the competing emission processes in porous silicon. We believe that the importance of this result is supported also by the low-cost fabrication process [170, 169] and of the flexibility of the material, together with the multiplicity of applications that could take advantage of its porosity.

In fact, besides further investigation of nonlinear effects in porous silicon microstructures, one can easily think about its potential application in the study of nonlinearities of other materials that could be infiltrated in the pores. Of course, it would require a retroactive optimization of the parameters of the waveguide, since the effective refractive index of the medium would change when infiltrating it, but the flexibility of porous silicon fabrication process could allow to actuate an easy re-optimization. We believe that the novelty of this work could act as a trigger for further studies of porous silicon integrated devices with applications in nonlinear optics.

In the work described in chapter 4 we switched to crystalline silicon samples, based on SOI architecture and obtained with standard industrial processes. Here, we demonstrated that in principle it is possible to use a microring resonator as a source of correlated photon pairs achieving full on-chip filtering and routing of the generated photons. The sample was constituted by the following components: grating couplers, to efficiently couple light into and out of the chip, a microring resonator, to generate the photon pairs by spontaneous four-wave mixing (SFWM), an integrated Distributed Bragg Reflector (DBR), to reject the pump laser after the experiment, and two add-drop filters to further reject the pump and to demultiplex the signal and idler photons that can be sent to two different outputs of the sample. Some elements on the chips, like microrings and add-drops, were also provided with heating elements, that could allow to tune their spectral response individually.

In the first reported experiment, we demonstrated that the pump laser can be completely filtered on a single chip. Indeed, that of pump filtering is a problem of non trivial solution, since one needs to reach a rejection of more than 100 dB in a relatively narrow bandwidth [41]. Our result was achieved as

following described. We first chose as pump resonance the one closest to the DBR, but at shorter wavelength so that it could be redshifted by acting on the heater, in order to bring it inside the stopband of the DBR. Even optimizing the position of the resonance in the region of higher rejection of the DBR, when exciting the pump resonance some residual laser was still clearly visible at the output. Even if the DBR with N=8000 total periods was designed to reject more than 90 dB, from its characterization we found an actual value around 65 dB. The complete rejection of the pump on a single chip was then achieved by tuning the two add-drops in resonance with it, giving up on the possibility to separate signal and idler, but allowing to observe the generated photons from the common output port of the sample, with full on-chip rejection of the pump.

We believe that the performance of this experiment could have been improved by slightly modifying the sample. For instance, one could think about carrying out a more detailed characterization of the DBRs, in order to decide how they can be modified to reach the necessary rejection. Alternatively one could explore the possibility to introduce trenches, or a larger separation between grating couplers, to see if they could help in getting a better performance out of the DBR. Here, we had to face also other problems, like broadening and deterioration of the add-drop resonances during the thermal tuning, due to the injection of carriers, which could have been avoided by simply using the same heaters as the ones used for the generating microrings.

In a second experiment two nominally identical chips were used: photons generated and partially filtered in the first chip A, were transmitted to a second device B, where the pump could be completely rejected by the second DBR, so that signal and idler photons could be separated by the add-drop filters. One of the difficulties in this experiment consisted in the mismatch between the stop band of the two DBRs. In order to tune them, so that they overlapped and could be used to filter the same pump laser, we had to employ the Peltier element to change the temperature of one of the samples, in order to achieve a thermal tuning of the whole chip. In the end, the filtered photons were picked up by the two add-drop filters, tuned one in correspondence of signal resonance, the other one on the idler, so that finally they could be sent to different outputs of the sample. We performed also time-correlation measurements on the output photons and, without the need of off-chip filtering, we were able to measure photons pairs with a generation rate above 1 MHz, and time correlation with a coincidence-to-accidental ratio (CAR) of 50. Since the value of CAR for classical light is 2, this measurement ensured us about the non-classical properties of the generated light. All the reported results were achieved without the need of off-chip filters, with the exception of bandpass filters to clean out the ASE emission of the input lasers. We suggest that in a next realization of this device, one could integrate further filtering elements like ad-hoc integrated DBR, prior to the generating ring, to clean out the pump laser. However, this would require for a higher reproducibility of the device

and the development of much more controllable integrated DBR filters.

This work represents an important step in the field of integrated quantum optics, in particular if we consider the recent demonstration that the same kind of resonators can be used as efficient sources of time-energy entangled photons [191]. After our demonstration that complete on-chip filtering is possible, we can infer to be one step closer to applications like fully integrated QKD emitters and receivers based on time-energy entanglement protocols [192], or to realization of boson sampling with heralded photon pairs [193].

An aspect that we intend to remark is that the device that we used has been fabricated with a CMOS compatible photonic process, and has a total footprint below 1 mm^2, allowing high reproducibility, scalability and possibility of high density of integration. As pointed out also in [34], the integration of filtering and routing is still considered a challenge to be solved for integrated photon sources. Our work, being the first reported case of full on-chip filtering and routing of correlated photons, can be considered as an important and promising improvement in the field.

Finally, in the fifth and last chapter, we demonstrated that a microring resonator emits photon pairs that can be nearly uncorrelated or strongly correlated, depending on the coherence time of the pump laser. This has been performed by exploiting stimulated FWM, to enable for a direct and rapid reconstruction of the joint spectral density (JSD) of the photon pairs generated by the spontaneous process. Previous measurements of JSD used to be performed with the detection of coincidences between spontaneously generated photons with single photon detectors. The intrinsically low efficiency of the method is strongly reduced by the need of narrow bandpass filters to select the idler and signal wavelengths. This method becomes prohibitive when one needs to characterize the quantum state of photon pairs that are generated by structures with high quality factors. In fact, it can be easily estimated that the characterization of photon pairs emitted by microring resonators with typical Q factors of about 4×10^4, having a linewidth of few tens of picometers, would need a measurement time on the order weeks. To find a solution to this time-consuming method, we applied the same principle of stimulated emission tomography, as reported by [50, 197], where the much more intense stimulated process is measured to study its quantum analogous constituted by the spontaneous process. In fact, exploiting the high signal-to-noise ratio that can be achieved in the stimulated process, that for the considered sources can be even four orders of magnitude more intense than the spontaneous one, it was possible to spectrally filter the generated photons down to few pm in order to reach record spectral resolution. In more detail, the resolution on the signal in our experiment was determined by the minimum step of the tunable signal laser used to stimulate the process, which is 2 pm. On the other hand, to have a good resolution on the generated idler, we built a custom Fabry-Pérot filter with remote control, that could be used as a tunable filter, scanning along the

resonance of generated idler photons with a resolution of 5 pm given by the FWHM of the Fabry-Pérot resonances. The resulting achieved resolution is about 10 pm^2, which is more than two orders of magnitude better than state-of-the-art measurements based on single photon detection, and much higher than analogous techniques applied to stimulated parametric down-conversion [196, 198, 199].

Our result allowed to clearly distinguish between time-energy correlated photons and uncorrelated photons. In fact, while time correlation is characteristic of photon pairs generated by parametric processes like FWM, it has been shown that the energy correlation can be controlled by changing the coherence time of the pump [50]. We first measured the JSD of photon pairs obtained with pulsed pump laser, with a coherence time comparable to that of the dwelling time of photons in the microring, estimated to be on the order of 33 ps. With pulsed pumping, we found a JSD with a circular-like shape, clearly representing uncorrelated photons. We then repeated the experiment replacing the pulsed pump with a continuous wave (cw) pump laser, having a coherence time (around 1 μm) which in this case is much longer than the dwelling time of the photons in the resonators. The corresponding JSD diagram has a diagonal and elongated shape that can be clearly attributed to correlation. For a more quantitative analysis we also determined the Schmidt number K, which is a parameter that can be extracted from the JSD diagrams, that is ideally equal to 1 in the case of total absence of correlations, while it tends to infinite in the case of perfect correlation [204, 205]. We compared the measured values with theoretical predictions, finding the following results. In the case of pulsed pumping there is a very good agreement between the theoretically predicted value, equal to $K = 1.09$, and its experimentally measured lower bound, which was found to be $K_{bound} = 1.03 \pm 0.1$. We can attribute the fact that the measured value is lower than the theoretical one, although within the uncertainty, to the finite spectral resolution of the experiment. In the case of cw pumping, while the theoretical Schmidt number was $K = 37038$, we found from experimental lower bound equal to $K_{bound} = 3.93$. In this case, the huge difference between the two values can be attributed to the noise in the measurements, which is uncorrelated and thus tends to strongly reduce the Schmidt number. However, it is possible to clearly distinguish between the correlated and uncorrelated case, which is indeed an extraordinary achievement. In fact, we can estimate that the whole JSD diagram that we obtained, which is composed by a total of more than $2{\times}10^3$ pixels, would have been smaller in size than a single pixel of the best result previously reported in literature! It means that a measurement performed with previous state-of-the-art techniques, would not have been able to detect any substantial difference between the two cases. Furthermore, the measurement time for the diagrams that we reported took about one hour of total integration time, which is incredibly shorter with respect to the time that would be needed by a typical coincidence-based experiment, estimated to be on the order of weeks. We suggest that the resolution that we

achieved could be further improved by replacing the Fabry-Pérot filter with an Optical Spectrum Analyzers (OSA) with MHz resolution. Furthermore, while this measurement was not bringing any information about the relative phase of the generated photons, one can think about the reconstruction of the joint spectral amplitude (JSA), that, including also information about the phase, could lead to more deep knowledge of the quantum state of the generated pairs. We suggest that this could be performed by setting up a measurement with heterodyne detection. We believe that the work reported in the last chapter can be seen as a clear demonstration that stimulated FWM is a useful tool to perform fast characterization of integrated sources of non-classical states of light.

In conclusion, we put another brick on the wall of silicon photonics, demonstrating that it can be considered as a suitable platform for building relatively cheap and compact emitters of quantum states of light. This realization would be necessary for the implementation, among other applications, of quantum cryptography, which would allow for totally secure communication through quantum key distribution. Exploiting the existence of fabs and the compatibility with the already existent telecommunication network, we are approaching to bring this technology to mass production for large scale distribution.

However, a central challenge consists in the standardization of silicon photonics components and characterization methods, which is a necessary step to bring these products to the public market. Thanks to the advent of foundries, complex silicon photonic products can be available at relatively low cost for research purposes and, in the next future, also on the market. We remark that the works that have been reported in this thesis are purposing standard, efficient and fast characterization methods for quantum integrated devices, together with practical realization of lab-on-a-chip generation of quantum states of light. In particular, works reported in chapter 4 and 5, were achieved on samples that have been realized in a foundry with a standard CMOS-compatible fabrication process: this can be seen as a demonstration that fabs are expected to play a crucial role in the future development of integrated quantum photonics.

Bibliography

[1] N. Gisin, G. Ribordy, W. Tittel, and H. Zbinden, "Quantum cryptography," *Rev. Mod. Phys.*, vol. 74, no. January, pp. 145–195, 2002.

[2] P. Kok, W. J. Munro, K. Nemoto, T. C. Ralph, J. P. Dowling, and G. J. Milburn, "Linear optical quantum computing with photonic qubits," *Rev. Mod. Phys.*, vol. 79, no. 1, pp. 135–174, 2007.

[3] J. L. O'Brien, A. Furusawa, and J. Vučković, "Photonic quantum technologies," *Nat. Photonics*, vol. 3, pp. 687–695, dec 2009.

[4] M. Nielsen and I. Chuang., *Quantum Computation and Quantum Information*. Cambridge University Press, 2000.

[5] P. Shor, "Polynomial-Time Algorithms for Prime Factorization and Discrete Logarithms on a Quantum Computer," *SIAM rev.*, vol. 41, no. 2, pp. 303–332, 1994.

[6] L. K. Grover, "A fast quantum mechanical algorithm for database search," *Proc. 28th Annu. ACM Symp. Theory Comput.*, p. 212, 1996.

[7] S. Aaronson and A. Arkhipov, "The computational complexity of linear optics," *Theory Comput.*, vol. 9, no. 1, pp. 143–252, 2013.

[8] W. K. Wootters and W. H. Zurek, "A single quantum cannot be cloned," *Nature*, vol. 299, pp. 802–803, 1982.

[9] C. H. Bennett and G. Brassard, "Quantum Cryptography: Public Key Distribution and Coin Tossing," *Proc. IEEE Int. Conf. Comput. Syst. Signal Process.*, pp. 175–179, 1984.

[10] A. K. Ekert, "Quantum cryptography based on Bell's theorem," *Phys. Rev. Lett.*, vol. 67, no. 6, pp. 661–663, 1991.

[11] R. Loudon, *The quantum theory of light*. Oxford University Press, 3rd ed., 2000.

[12] E. Knill, R. Laflamme, and G. J. Milburn, "A scheme for efficient quantum computation with linear optics.," *Nature*, vol. 409, pp. 46–52, jan 2001.

[13] M. D. Eisaman, J. Fan, A. Migdall, and S. V. Polyakov, "Invited review article: Single photon sources and detectors," *Rev. Sci. Instrum.*, vol. 82, no. 4, 2011.

[14] J. McKeever, A. Boca, A. D. Boozer, R. Miller, J. R. Buck, A. Kuzmich, and H. J. Kimble, "Deterministic Generation of Single Photons from One Atom Trapped in a Cavity," *Science (80-.).*, vol. 303, no. March, p. 1992, 2004.

[15] C. Santori, M. Pelton, G. Solomon, Y. Dale, and Y. Yamamoto, "Triggered single photons from a quantum dot," *Phys. Rev. Lett.*, vol. 86, no. 8, pp. 1502–1505, 2001.

[16] M. Toishi, D. Englund, A. Faraon, and J. Vučković, "High-brightness single photon source from a quantum dot in a directional-emission nanocavity.," *Opt. Express*, vol. 17, no. 17, pp. 14618–14626, 2009.

[17] J. Claudon, J. Bleuse, N. S. Malik, M. Bazin, N. Gregersen, C. Sauvan, P. Lalanne, and J.-m. Gérard, "A highly efficient single-photon source based on a quantum dot in a photonic nanowire," *Nat. Photonics*, vol. 4, no. March, pp. 174–177, 2010.

[18] O. Gazzano, S. Michaelis de Vasconcellos, C. Arnold, a. Nowak, E. Galopin, I. Sagnes, L. Lanco, a. Lemaître, and P. Senellart, "Bright solid-state sources of indistinguishable single photons.," *Nat. Commun.*, vol. 4, p. 1425, 2013.

[19] K. H. Madsen, S. Ates, J. Liu, A. Javadi, S. M. Albrecht, I. Yeo, S. Stobbe, and P. Lodahl, "Efficient out-coupling of high-purity single photons from a coherent quantum dot in a photonic-crystal cavity," *Phys. Rev. B - Condens. Matter Mater. Phys.*, vol. 90, no. 15, pp. 1–11, 2014.

[20] T. M. Babinec, B. J. M. Hausmann, M. Khan, Y. Zhang, J. R. Maze, P. R. Hemmer, and M. Loncar, "A diamond nanowire single-photon source.," *Nat. Nanotechnol.*, vol. 5, pp. 195–9, mar 2010.

[21] A. Sipahigil, M. L. Goldman, E. Togan, Y. Chu, M. Markham, D. J. Twitchen, A. S. Zibrov, A. Kubanek, and M. D. Lukin, "Quantum interference of single photons from remote nitrogen-vacancy centers in diamond," *Phys. Rev. Lett.*, vol. 108, no. 14, pp. 1–5, 2012.

[22] E. Neu, M. Agio, and C. Becher, "Photophysics of single silicon vacancy centers in diamond: implications for single photon emission," *Opt. Express*, vol. 20, no. 18, pp. 19956–19971, 2012.

[23] I. Aharonovich and E. Neu, "Diamond nanophotonics," *Adv. Opt. Mater.*, vol. 2, no. 10, pp. 911–928, 2014.

[24] W. Grice, a. U'Ren, and I. Walmsley, "Eliminating frequency and space-time correlations in multiphoton states," *Phys. Rev. A*, vol. 64, no. 6, pp. 1–7, 2001.

[25] M. Davanco, J. R. Ong, A. B. Shehata, A. Tosi, I. Agha, S. Assefa, F. Xia, W. M. J. Green, S. Mookherjea, and K. Srinivasan, "Telecommunications-band heralded single photons from a silicon nanophotonic chip," *Appl. Phys. Lett.*, vol. 100, no. 26, p. 261104, 2012.

[26] R. Stevenson, R. J. Young, P. Atkinson, K. Cooper, D. A. Ritchie, and A. J. Shields, "A semiconductor source of triggered entangled photon pairs," *Nature*, vol. 439, pp. 179–182, 2006.

[27] Y. Chen, J. Zhang, M. Zopf, K. Jung, Y. Zhang, R. Keil, F. Ding, and O. G. Schmidt, "Wavelength-tunable entangled photons from silicon-integrated III-V quantum dots.," *Nat. Commun.*, vol. 7, p. 10387, 2016.

[28] J. E. Sharping, K. F. Lee, M. a. Foster, A. C. Turner, B. S. Schmidt, M. Lipson, A. L. Gaeta, and P. Kumar, "Generation of correlated photons in nanoscale silicon waveguides.," *Opt. Express*, vol. 14, pp. 12388–93, dec 2006.

[29] H. Takesue, Y. Tokura, H. Fukuda, T. Tsuchizawa, T. Watanabe, K. Yamada, and S.-i. Itabashi, "Entanglement generation using silicon wire waveguide," *Appl. Phys. Lett.*, vol. 91, no. 20, p. 201108, 2007.

[30] K.-i. Harada, H. Takesue, H. Fukuda, T. Tsuchizawa, T. Watanabe, K. Yamada, Y. Tokura, and S.-i. Itabashi, "Generation of high-purity entangled photon pairs using silicon wire waveguide.," *Opt. Express*, vol. 16, pp. 20368–73, dec 2008.

[31] L. Olislager, J. Safioui, S. Clemmen, K. P. Huy, W. Bogaerts, P. Emplit, and S. Massar, "Silicon-on-insulator integrated source of polarization-entangled photons," *Opt. Lett.*, vol. 38, pp. 1960–1962, 2013.

[32] J. W. Silverstone, D. Bonneau, K. Ohira, N. Suzuki, H. Yoshida, N. Iizuka, M. Ezaki, C. M. Natarajan, M. G. Tanner, R. H. Hadfield, V. Zwiller, G. D. Marshall, J. G. Rarity, J. L. O'Brien, and M. G. Thompson, "On-chip quantum interference between silicon photon-pair sources," *Nat. Photonics*, vol. 8, pp. 104–108, dec 2013.

[33] R. Soref, "The Past, Present, and Future of Silicon Photonics," *IEEE J. Sel. Top. Quantum Electron.*, vol. 12, no. 6, pp. 1678–1687, 2006.

[34] C. Xiong, B. Bell, and B. J. Eggleton, "CMOS-compatible photonic devices for single-photon generation," *Nanophotonics*, 2016.

[35] M. Hochberg and T. Baehr-Jones, "Towards fabless silicon photonics," *Nat. Photonics*, vol. 4, no. 8, pp. 492–494, 2010.

[36] M. Streshinsky, R. Ding, Y. Liu, A. Novack, C. Galland, A. E.-J. Lim, P. G.-Q. Lo, T. Baehr-Jones, and M. Hochberg, "The road to affordable large-scale silicon photonics," *Opt. photonics news*, no. September, pp. 32–39, 2013.

[37] A. Yariv and W. Ye, *Photonics*. Oxford University Press, 2007.

[38] M. Lipson, "Guiding, modulating, and emitting light on Silicon - Challenges and opportunities," *J. Light. Technol.*, vol. 23, no. 12, pp. 4222–4238, 2005.

[39] W. Bogaerts, P. De Heyn, T. Van Vaerenbergh, K. De Vos, S. Kumar Selvaraja, T. Claes, P. Dumon, P. Bienstman, D. Van Thourhout, and R. Baets, "Silicon microring resonators," *Laser Photonics Rev.*, vol. 6, no. 1, pp. 47–73, 2012.

[40] Q. Xu, B. Schmidt, S. Pradhan, and M. Lipson, "Micrometre-scale silicon electro-optic modulator.," *Nature*, vol. 435, no. 7040, pp. 325–7, 2005.

[41] S. Azzini, D. Grassani, M. Galli, L. C. Andreani, M. Sorel, M. J. Strain, L. G. Helt, J. E. Sipe, M. Liscidini, and D. Bajoni, "From classical four-wave mixing to parametric fluorescence in silicon microring resonators.," *Opt. Lett.*, vol. 37, pp. 3807–9, sep 2012.

[42] Y. Shen, *The Principles of Nonlinear Optics*. Wiley Intercience, 1984.

[43] R. W. Boyd, *Nonlinear Optics*. Academic press, 2003.

[44] J. Chen, X. Li, and P. Kumar, "Two-photon-state generation via four-wave mixing in optical fibers," *Phys. Rev. A - At. Mol. Opt. Phys.*, vol. 72, no. 3, pp. 1–9, 2005.

[45] Q. Lin, F. Yaman, and G. P. Agrawal, "Photon-pair generation in optical fibers through four-wave mixing: Role of Raman scattering and pump polarization," *Phys. Rev. A - At. Mol. Opt. Phys.*, vol. 75, no. 2, pp. 1–20, 2007.

[46] A. C. Turner, M. A. Foster, A. L. Gaeta, and M. Lipson, "Ultra-low power parametric frequency conversion in a silicon microring resonator," *Opt Express*, vol. 16, no. 7, pp. 4881–4887, 2008.

[47] S. Clemmen, K. Phan Huy, W. Bogaerts, R. G. Baets, P. Emplit, and S. Massar, "Continuous wave photon pair generation in silicon-on-insulator waveguides and ring resonators.," *Opt. Express*, vol. 17, pp. 16558–70, sep 2009.

[48] J. W. Silverstone, R. Santagati, D. Bonneau, M. J. Strain, M. Sorel, J. L. O'Brien, and M. G. Thompson, "Qubit entanglement between ring-resonator photon-pair sources on a silicon chip," *Nat. Commun.*, vol. 6, p. 7948, 2015.

[49] D. Grassani, S. Azzini, M. Liscidini, M. Galli, M. J. Strain, M. Sorel, J. E. Sipe, and D. Bajoni, "Micrometer-scale integrated silicon source of time-energy entangled photons," *Optica*, vol. 2, no. 2, p. 88, 2015.

[50] L. G. Helt, Z. Yang, M. Liscidini, and J. E. Sipe, "Spontaneous four-wave mixing in microring resonators.," *Opt. Lett.*, vol. 35, pp. 3006–8, sep 2010.

[51] D. Grassani, A. Simbula, S. Pirotta, M. Galli, M. Menotti, N. C. Harris, T. Baehr-jones, M. Hochberg, C. Galland, M. Liscidini, and D. Bajoni, "Energy correlations of photon pairs generated by a silicon microring resonator probed by Stimulated Four Wave Mixing," *Nat. Publ. Gr.*, no. October 2015, pp. 8–13, 2016.

[52] A. Simbula, G. A. Rodriguez, M. Menotti, S. De Pace, S. M. Weiss, M. Galli, M. Liscidini, and D. Bajoni, "Low-power four-wave mixing in porous silicon microring resonators," *Appl. Phys. Lett.*, vol. 109, no. 2, p. 021106, 2016.

[53] N. C. Harris, D. Grassani, A. Simbula, M. Pant, M. Galli, T. Baehr-Jones, M. Hochberg, D. Englund, D. Bajoni, and C. Galland, "Integrated source of spectrally filtered correlated photons for large-scale quantum photonic systems," *Phys. Rev. X*, vol. 4, no. 4, pp. 1–10, 2014.

[54] B. T. Gard, K. R. Motes, J. P. Olson, P. P. Rohde, and J. P. Dowling, "An Introduction to Boson-Sampling," *From At. to Mesoscale*, pp. 167–192, 2015.

[55] J. L. O'Brien, G. J. Pryde, a. G. White, T. C. Ralph, and D. Branning, "Demonstration of an all-optical quantum controlled-NOT gate.," *Nature*, vol. 426, pp. 264–7, nov 2003.

[56] A. Politi, M. J. Cryan, J. G. Rarity, S. Yu, and J. L. O'Brien, "Silica-on-silicon waveguide quantum circuits.," *Science (80-.).*, vol. 320, pp. 646–9, may 2008.

[57] A. Crespi, R. Osellame, R. Ramponi, D. J. Brod, E. F. Galv, C. Vitelli, E. Maiorino, P. Mataloni, and F. Sciarrino, "Integrated multimode interferometers with arbitrary designs for photonic boson sampling," *Nat. Photonics*, vol. 7, pp. 545–549, 2013.

[58] J. B. Spring, B. J. Metcalf, P. C. Humphreys, W. S. Kolthammer, X.-M. Jin, M. Barbieri, A. Datta, N. Thomas-Peter, N. K. Langford,

D. Kundys, J. C. Gates, B. J. Smith, P. G. R. Smith, and I. A. Walmsley, "Boson Sampling on a Photonic Chip," *Science (80-.).*, vol. 339, no. 6121, pp. 798–801, 2013.

[59] M. a. Broome, A. Fedrizzi, S. Rahimi-Keshari, J. Dove, S. Aaronson, T. C. Ralph, and A. G. White, "Photonic boson sampling in a tunable circuit.," *Science*, vol. 339, pp. 794–8, feb 2013.

[60] A. Peruzzo, M. Lobino, J. C. F. Matthews, N. Matsuda, A. Politi, K. Poulios, X.-Q. Zhou, Y. Lahini, N. Ismail, K. Wörhoff, Y. Bromberg, Y. Silberberg, M. G. Thompson, and J. L. OBrien, "Quantum walks of correlated photons.," *Science*, vol. 329, pp. 1500–3, sep 2010.

[61] A. Aspuru-Guzik and P. Walther, "Photonic Quantum Orreries: Review of photonic quantum simulations.," *Nat. Phys.*, vol. 8, no. 4, pp. 285–291, 2012.

[62] H.-K. Lo, M. Curty, and K. Tamaki, "Secure quantum key distribution," *Nat. Photonics*, vol. 8, no. 8, pp. 595–604, 2014.

[63] M. Hosseini, G. Campbell, B. Sparkes, P. K. Lam, and B. C. Buchler, "Unconditional Room Temperature Quantum Memory," *Nat. Phys.*, vol. 7, pp. 794–794, 2011.

[64] R. Hanbury Brown and R. Q. Twiss, "Correlation Between Photons in Two Coherent Beams of Light," *Nature*, vol. 177, no. 4497, p. 27, 1956.

[65] C. K. Hong, Z. Y. Ou, and L. Mandel, "Measurement of subpicosecond time intervals between two photons by interference," *Phys. Rev. Lett.*, vol. 59, p. 2044, 1987.

[66] P. Lodahl, S. Mahmoodian, and S. Stobbe, "Interfacing single photons and single quantum dots with photonic nanostructures," *Rev. Mod. Phys.*, vol. 87, no. 2, pp. 347–400, 2015.

[67] C. Santori, D. Fattal, J. Vucković, G. S. Solomon, and Y. Yamamoto, "Indistinguishable photons from a single-photon device.," *Nature*, vol. 419, pp. 594–7, oct 2002.

[68] E. Purcell, H. Torrey, and R. Pound, "Resonance Absorption by Nuclear Magnetic Moments in a Solid," *Phys. Rev.*, vol. 69, no. 1-2, pp. 37–38, 1946.

[69] J. Gérard, B. Sermage, B. Gayral, B. Legrand, E. Costard, and V. Thierry-Mieg, "Enhanced Spontaneous Emission by Quantum Boxes in a Monolithic Optical Microcavity," *Phys. Rev. Lett.*, vol. 81, no. 5, pp. 1110–1113, 1998.

[70] Y.-M. He, Y. He, Y.-J. Wei, D. Wu, M. Atatüre, C. Schneider, S. Höfling, M. Kamp, C.-Y. Lu, and J.-W. Pan, "On-demand semiconductor single-photon source with near-unity indistinguishability.," *Nat. Nanotechnol.*, vol. 8, pp. 213–7, mar 2013.

[71] X. Ding, Y. He, Z. C. Duan, N. Gregersen, M. C. Chen, S. Unsleber, S. Maier, C. Schneider, M. Kamp, S. Hofling, C. Y. Lu, and J. W. Pan, "On-Demand Single Photons with High Extraction Efficiency and Near-Unity Indistinguishability from a Resonantly Driven Quantum Dot in a Micropillar," *Phys. Rev. Lett.*, vol. 116, no. 2, pp. 1–6, 2016.

[72] N. Prtljaga, C. Bentham, J. O'Hara, B. Royall, E. Clarke, L. R. Wilson, M. S. Skolnick, and A. M. Fox, "On-chip interference of single photons from an embedded quantum dot and a laser," *Appl. Phys. Lett.*, vol. 108, p. 255101, 2016.

[73] E. N. Somaschi, V. Giesz, L. D. Santis, J. C. Loredo, M. P. Almeida, G. Hornecker, S. L. Portalupi, T. Grange, C. Antón, J. Demory, C. Gómez, I. Sagnes, N. D. Lanzillotti-Kimura, A. Lemaítre, A. Auffeves, A. G. White, L. Lanco, and P. Senellart, "Near-optimal single-photon sources in the solid state," *Nat. Photonics*, vol. 10, pp. 340–345, 2016.

[74] J. C. Loredo, N. A. Zakaria, N. Somaschi, C. Anton, L. de Santis, V. Giesz, T. Grange, M. A. Broome, O. Gazzano, G. Coppola, I. Sagnes, A. Lemaitre, A. Auffeves, P. Senellart, M. P. Almeida, and A. G. White, "Scalable performance in solid-state single-photon sources," *Optica*, vol. 3, no. 4, p. 433, 2016.

[75] A. Thoma, P. Schnauber, M. Gschrey, M. Seifried, J. Wolters, J. H. Schulze, A. Strittmatter, S. Rodt, A. Carmele, A. Knorr, T. Heindel, and S. Reitzenstein, "Exploring Dephasing of a Solid-State Quantum Emitter via Time- and Temperature-Dependent Hong-Ou-Mandel Experiments," *Phys. Rev. Lett.*, vol. 116, no. 3, pp. 1–5, 2016.

[76] E. Togan, Y. Chu, A. S. Trifonov, L. Jiang, J. Maze, L. Childress, M. V. G. Dutt, A. S. Sørensen, P. R. Hemmer, A. S. Zibrov, and M. D. Lukin, "Quantum entanglement between an optical photon and a solid-state spin qubit," *Nature*, vol. 466, pp. 730–734, 2010.

[77] B. Hensen, H. Bernien, A. E. Dréau, A. Reiserer, N. Kalb, M. S. Blok, J. Ruitenberg, R. F. L. Vermeulen, R. N. Schouten, C. Abellán, W. Amaya, V. Pruneri, M. W. Mitchell, M. Markham, D. J. Twitchen, D. Elkouss, S. Wehner, T. H. Taminiau, and R. Hanson, "Loophole-free Bell inequality violation using electron spins separated by 1.3 kilometres," *Nature*, vol. 526, no. 7575, pp. 682–686, 2015.

[78] H. Bernien, L. Childress, L. Robledo, M. Markham, D. Twitchen, and R. Hanson, "Two-photon quantum interference from separate nitrogen vacancy centers in diamond," *Phys. Rev. Lett.*, vol. 108, no. 4, pp. 1–5, 2012.

[79] P. J. Mosley, J. S. Lundeen, B. J. Smith, P. Wasylczyk, A. B. U'Ren, C. Silberhorn, and I. A. Walmsley, "Heralded generation of ultrafast single photons in pure quantum states," *Phys. Rev. Lett.*, vol. 100, no. 13, pp. 1–5, 2008.

[80] A. R. McMillan, J. Fulconis, M. Halder, C. Xiong, J. G. Rarity, and W. J. Wadsworth, "Narrowband high-fidelity all-fibre source of heralded single photons at 1570 nm.," *Opt. Express*, vol. 17, no. 8, pp. 6156–65, 2009.

[81] J. B. Spring, P. S. Salter, B. J. Metcalf, P. C. Humphreys, M. Moore, N. Thomas-peter, X.-m. Jin, N. K. Langford, W. Steven, M. J. Booth, and I. A. Walmsley, "On-chip low loss heralded source of pure single photons," *Opt. Express*, vol. 21, no. 11, pp. 13522–13532, 2013.

[82] M. J. Collins, C. Xiong, I. H. Rey, T. D. Vo, J. He, S. Shahnia, C. Reardon, T. F. Krauss, M. J. Steel, a. S. Clark, and B. J. Eggleton, "Integrated spatial multiplexing of heralded single-photon sources.," *Nat. Commun.*, vol. 4, p. 2582, jan 2013.

[83] P. Grangier, G. Roger, and A. Aspect, "Experimental Evidence for a Photon Anticorrelation Effect on a Beam Splitter: A New Light on Single-Photon Interferences," *Eur. Lett.*, vol. 1, pp. 173–179, 1986.

[84] P. G. Kwiat, K. Mattle, H. Weinfurter, A. Zeilinger, A. V. Sergienko, and Y. Shih, "New high-intensity source of polarization-entangled photon pairs," *Phys. Rev. Lett.*, vol. 75, no. 24, pp. 4337–4341, 1995.

[85] B. J. Smith, D. Kundys, N. Thomas-peter, and I. A. Walmsley, "Phase-controlled integrated photonic quantum circuits," *Opt. Express*, vol. 17, no. 16, pp. 13516–13525, 2009.

[86] S. Tanzilli, H. de Riedmatten, W. Tittel, H. Zbinden, P. Baldi, M. de Micheli, D. B. Ostrowsky, and N. Gisin, "PPLN Waveguide for Quantum Communication," *Eur. Phys. J. D*, vol. 18, pp. 155–160, 2002.

[87] H. Takesue and K. Shimizu, "Effects of multiple pairs on visibility measurements of entangled photons generated by spontaneous parametric processes," *Opt. Commun.*, vol. 283, no. 2, pp. 276–287, 2010.

[88] T. Meany, L. A. Ngah, M. J. Collins, A. S. Clark, R. J. Williams, B. J. Eggleton, M. J. Steel, M. J. Withford, O. Alibart, and S. Tanzilli, "Hybrid photonic circuit for multiplexed heralded single photons," *Laser Photonics Rev.*, vol. 8, no. 3, pp. 42–46, 2014.

[89] A. Einstein, B. Podolski, and N. Rosen, "Can quantum-mechanical description of physical reality be considered complete?," *Phys. Rev.*, vol. 47, pp. 777–780, 1935.

[90] J. S. Bell, "On the Einstein Podolski Rosen Paradox," *Physics (College. Park. Md).*, vol. 1, no. 3, pp. 195–200, 1964.

[91] J. F. Clauser, M. A. Horne, A. Shimony, and R. A. Holt, "Proposed experiment to test local hidden-variable theories," *Phys. Rev. Lett.*, vol. 23, no. 15, pp. 880–884, 1969.

[92] A. Aspect, P. Grangier, and G. Roger, "Experimental tests of realistic local theories via Bell's Theorem," *Phys. Rev. Lett.*, vol. 47, no. 7, pp. 460–463, 1981.

[93] L. K. Shalm, E. Meyer-Scott, B. G. Christensen, P. Bierhorst, M. A. Wayne, M. J. Stevens, T. Gerrits, S. Glancy, D. R. Hamel, M. S. Allman, K. J. Coakley, S. D. Dyer, C. Hodge, A. E. Lita, V. B. Verma, C. Lambrocco, E. Tortorici, A. L. Migdall, Y. Zhang, D. R. Kumor, W. H. Farr, F. Marsili, M. D. Shaw, J. A. Stern, C. Abellàn, W. Amaya, V. Pruneri, T. Jennewein, M. W. Mitchell, P. G. Kwiat, J. C. Bienfang, R. P. Mirin, E. Knill, and S. W. Nam, "Strong Loophole-Free Test of Local Realism," *Phys. Rev. Lett.*, vol. 115, no. 25, pp. 1–10, 2015.

[94] J. A. Larsson, "Loopholes in Bell inequality tests of local realism," *J. Phys. A Math. Theor.*, vol. 47, no. 42, p. 424003, 2014.

[95] J. D. Franson, "Bell Inequality for Position and Time," *Phys. Rev. Lett.*, vol. 62, p. 2205, 1989.

[96] I. Marcikic, H. de Riedmatten, W. Tittel, V. Scarani, H. Zbinden, and N. Gisin, "Time-bin entangled qubits for quantum communication created by femtosecond pulses," *Phys. Rev. A*, vol. 66, p. 062308, dec 2002.

[97] R. F. Werner, "Quantum states with Einstein-Podolsky-Rosen correlations admitting a hidden-variable model," *Phys. Rev. A*, vol. 40, p. 4277, 1989.

[98] J. C. F. Matthews, A. Politi, A. Stefanov, and J. L. O'Brien, "Manipulation of multiphoton entanglement in waveguide quantum circuits," *Nat. Photonics*, vol. 3, no. June, pp. 346–350, 2009.

[99] M. Thompson, a. Politi, J. Matthews, and J. O'Brien, "Integrated waveguide circuits for optical quantum computing," *IET Circuits, Devices Syst.*, vol. 5, no. 2, p. 94, 2011.

[100] H. W. Li, S. Przeslak, a. O. Niskanen, J. C. F. Matthews, a. Politi, P. Shadbolt, a. Laing, M. Lobino, M. G. Thompson, and J. L. O'Brien,

"Reconfigurable controlled two-qubit operation on a quantum photonic chip," *New J. Phys.*, vol. 13, p. 115009, nov 2011.

[101] A. Crespi, R. Ramponi, R. Osellame, L. Sansoni, I. Bongioanni, F. Sciarrino, G. Vallone, and P. Mataloni, "Integrated photonic quantum gates for polarization qubits.," *Nat. Commun.*, vol. 2, p. 566, jan 2011.

[102] N. Matsuda, H. Takesue, K. Shimizu, Y. Tokura, and M. Notomi, "Slow light enhanced correlated photon pair generation in photonic-crystal coupled-resonator optical waveguides," *Opt. Express*, vol. 21, no. 7, pp. 8596–8604, 2013.

[103] H. Takesue, N. Matsuda, E. Kuramochi, and M. Notomi, "Entangled photons from on-chip slow light.," *Sci. Rep.*, vol. 4, p. 3913, jan 2014.

[104] G. Fujii, N. Namekata, M. Motoya, S. Kurimura, and S. Inoue, "Bright narrowband source of photon pairs at optical telecommunication wavelengths using a type-II periodically poled lithium niobate waveguide," *Opt. Express*, vol. 15, pp. 12769–12776, 2007.

[105] A. Orieux, A. Eckstein, A. Lemaître, P. Filloux, I. Favero, G. Leo, T. Coudreau, A. Keller, P. Milman, and S. Ducci, "Direct bell states generation on a III-V semiconductor chip at room temperature," *Phys. Rev. Lett.*, vol. 110, no. 16, pp. 1–5, 2013.

[106] K. Yamada, "Silicon Photonics Wire Waveguides: Fundamentals and applications," *Top. Appl. Phys.*, vol. 119, pp. 1–29, 2011.

[107] R. A. Soref, J. Schmidtchen, and K. Peterman, "Large single-mode rib waveguides in GeSi-Si and Si-on-SiO," *IEEE J. Quantum Electron.*, vol. 27, no. 8, pp. 1971–1973, 1991.

[108] U. Fischer, T. Zinke, J.-R.Kropp, F. Arndt, and K. Peterman, "0.1 dB/cm waveguide losses in single-mode SOI rib waveguides," *IEEE Photon. Technol. Lett.*, vol. 8, no. 5, pp. 647–648, 1996.

[109] S. Somekh, E. Garmire, A. Yariv, H. L. Garvin, and R. G. Hunsperger, "Channel optical waveguide directional couplers," *Appl. Phys. Lett.*, vol. 22, no. 1, pp. 46–47, 1973.

[110] C. Kopp, B. B. Bakir, J.-m. Fedeli, R. Orobtchouk, F. Schrank, H. Porte, L. Zimmermann, and T. Tekin, "Silicon Photonic Circuits : On-CMOS Integration , Fiber Optical Coupling , and Packaging," *IEEE J. Sel. Top. quantum Electron.*, vol. 17, no. 3, pp. 498–509, 2011.

[111] D. Taillaert, P. Bienstman, and R. Baets, "Compact efficient broadband grating coupler for silicon-on-insulator waveguides.," *Opt. Lett.*, vol. 29, no. 23, pp. 2749–2751, 2004.

[112] W. Bogaerts, D. Taillaert, B. Luyssaert, P. Dumon, J. V. Campenhout, P. Bienstman, D. V. Thourhout, and R. Baets, "Basic structures for photonic integrated circuits in Silicon-on-insulator," *Opt. Express*, vol. 12, no. 8, pp. 1583–1591, 2004.

[113] X. Wang, W. Shi, H. Yun, S. Grist, N. A. F. Jaeger, and L. Chrostowski, "Narrow-band waveguide Bragg gratings on SOI wafers with CMOS-compatible fabrication process," *Opt. Express*, vol. 20, no. 14, p. 15547, 2012.

[114] B. Little, S. Chu, H. Haus, J. Foresi, and J. Laine, "Microring resonator channel dropping filters," *J. Light. Technol.*, vol. 15, pp. 998–1005, 1997.

[115] W. R. Mckinnon, D. Xu, C. Storey, E. Post, A. Densmore, A. Delage, P. Waldron, J. H. Schimid, and S. Banz, "Extracting coupling and loss coefficients from a ring resonator," *Opt Express*, vol. 17, no. 21, pp. 18971–18982, 2009.

[116] J. Niehusmann, A. Vörckel, P. H. Bolivar, T. Wahlbrink, and W. Henschel, "Ultrahigh-quality-factor silicon-on-insulator Microring Resonator," *Opt. Lett.*, vol. 29, no. 24, pp. 2861–2863, 2004.

[117] A. Vörckel, M. Mönster, W. Henschel, P. Haring Bolivar, and H. Kurz, "Asymmetrically coupled silicon-on-insulator microring resonators for compact add-drop multiplexers," *IEEE Photonics Technol. Lett.*, vol. 15, no. 7, pp. 921–923, 2003.

[118] M. S. Nawrocka, T. Liu, X. Wang, and R. R. Panepucci, "Tunable silicon microring resonator with wide free spectral range," *Appl. Phys. Lett.*, vol. 89, no. 7, pp. 7–10, 2006.

[119] K. De Vos, I. Bartolozzi, E. Schacht, P. Bienstman, and R. Baets, "Silicon-on-Insulator microring resonator for sensitive and label-free biosensing," *Opt. Express*, vol. 15, no. 12, pp. 7610–7615, 2007.

[120] Y. Sun and X. Fan, "Optical ring resonators for biochemical and chemical sensing.," *Anal. Bioanal. Chem.*, vol. 399, pp. 205–11, jan 2011.

[121] M. S. Luchansky and R. C. Bailey, "High- Q Optical Sensors for Chemical and Biological Analysis," *Anal. Chem.*, vol. 84, no. 2, pp. 793–821, 2012.

[122] G. A. Rodriguez, S. Hu, and S. M. Weiss, "Porous silicon ring resonator for compact, high sensitivity biosensing applications," *Opt. Express*, vol. 23, no. 6, p. 7111, 2015.

[123] Y. Lu, Y. Tian, and L. Yang, "Integrated reconfigurable optical add-drop multiplexers based on cascaded microring resonators," *J. Semicond.*, vol. 34, no. 9, p. 094012, 2013.

[124] J. K. S. Poon, J. Scheuer, Y. Xu, and A. Yariv, "Designing coupled-resonator optical waveguide delay lines," *J. Opt. Soc. Am. B*, vol. 21, no. 9, p. 1665, 2004.

[125] A. Melloni, A. Canciamilla, C. Ferrari, F. Morichetti, L. O'Faolain, T. F. Krauss, R. De La Rue, A. Samarelli, and M. Sorel, "Tunable delay lines in silicon photonics: Coupled resonators and photonic crystals, a comparison," *IEEE Photonics J.*, vol. 2, no. 2, pp. 181–194, 2010.

[126] F. Xia, L. Sekaric, and Y. Vlasov, "Resonantly enhanced all optical buffers on a silicon chip," *Nat. Photonics*, vol. 1, no. January, pp. 65–71, 2007.

[127] F. Morichetti, C. Ferrari, A. Canciamilla, and A. Melloni, "The first decade of coupled resonator optical waveguides: Bringing slow light to applications," *Laser Photonics Rev.*, vol. 6, no. 1, pp. 74–96, 2012.

[128] G. Reed, G. Mashanovich, F. Gardes, and D. J. Thomson, "Silicon optical modulators," *Nat. Photonics*, vol. 4, no. 8, pp. 518–526, 2010.

[129] S. Manipatruni, Q. Xu, and M. Lipson, "PINIP based high-speed high-extinction ratio micron-size silicon electrooptic modulator.," *Opt. Express*, vol. 15, no. 20, pp. 13035–42, 2007.

[130] B. Guha, K. Preston, and M. Lipson, "Athermal silicon microring electro-optic modulator," *Opt. Lett.*, vol. 37, no. 12, pp. 2253–2255, 2012.

[131] R. W. Boyd and G. L. Fischer, "Nonlinear Optical Materials," 2001.

[132] M. Dinu, F. Quochi, and H. Garcia, "Third-order nonlinearities in silicon at telecom wavelengths," *Appl. Phys. Lett.*, vol. 82, no. 2003, pp. 2954–2956, 2003.

[133] G. P. Agrawal, C. Cojan, and C. Flytzanis, "Nonlinear optical properties of one-dimensional semiconductors and conjucated polymers," *Phys. Rev. B*, vol. 17, no. 2, p. 776, 1978.

[134] Y. Guo, W. Zhang, S. Dong, Y. Huang, and J. Peng, "Telecom-band degenerate-frequency photon pair generation in silicon microring cavities," *Opt. Lett.*, vol. 39, p. 2526, apr 2014.

[135] Q. Lin, O. J. Painter, and G. P. Agrawal, "Nonlinear optical phenomena in silicon waveguides: Modeling and applications," *Opt. Express*, vol. 15, no. 25, pp. 16604–16644, 2007.

[136] S. Azzini, *Classical and quantum nonlinear emission of light from photonic micro- and nano-cavities*. PhD thesis, 2013.

[137] L. Pavesi and R. Turan, *Silicon Nanocrystals: Fundamentals, Synthesis and Applications*. Wiley-VCH Verlag GmbH & Co. KGaA, 2010.

[138] S. A. Akhmanov, V. I. Emel'yanov, N. I. Koroteev, and V. N. Seminogov, "Interaction of powerful laser radiation with the surfaces of semiconductors and metals: nonlinear optical effects and nonlinear optical diagnostics," *Sov. Phys. Uspekhi*, vol. 28, pp. 1084–1124, dec 1985.

[139] M. Hatano, S. Moon, M. Lee, K. Suzuki, and C. P. Grigoropoulos, "Excimer laser-induced temperature field in melting and resolidification of silicon thin films," *J. Appl. Phys.*, vol. 87, no. 2000, p. 36, 2000.

[140] P. P. Absil, J. V. Hryniewicz, B. E. Little, P. S. Cho, R. A. Wilson, L. G. Joneckis, and P.-T. Ho, "Wavelength conversion in GaAs micro-ring resonators,," *Opt. Lett.*, vol. 25, no. 8, p. 554, 2000.

[141] L. G. Helt, M. Liscidini, and J. E. Sipe, "How does it scale? Comparing quantum and classical nonlinear optical processes in integrated devices," *J. Opt. Soc. Am. B*, vol. 29, no. 8, p. 2199, 2012.

[142] S. Azzini, D. Grassani, M. J. Strain, M. Sorel, L. G. Helt, J. E. Sipe, M. Liscidini, M. Galli, and D. Bajoni, "Ultra-low power generation of twin photons in a compact silicon ring resonator.," *Opt. Express*, vol. 20, pp. 23100–7, oct 2012.

[143] N. Gisin, R. Passy, P. Blasco, M. O. V. Deventer, R. Distl, H. Gilgen, B. Perny, R. Keys, E. Krause, C. C. Larsen, K. Mori, J. Pelayo, and J. Vobian, "Definition of polarization mode dispersion and first results of the COST 241 round-robin measurements," *Pure Appl. Opt. J. Eur. Opt. Soc. Part A*, vol. 4, pp. 511–522, sep 1995.

[144] I. P. Kaminow, "Polarization in optical fibers," *IEEE J. Quant. Electr*, vol. 17, pp. 15–22, 1981.

[145] C. R. Menyuk, "Nonlinear pulse propagation in birefringent optical fibers," *IEEE J. Quantum Electron.*, vol. 23, no. 2, pp. 174–176, 1987.

[146] R. Ursin, F. Tiefenbacher, T. Schmitt-Manderbach, H. Weier, T. Scheidl, M. Lindenthal, B. Blauensteiner, T. Jennewein, J. Perdigues, P. Trojek, B. Omer, M. Furst, M. Meyenburg, J. Rarity, Z. Sodnik, C. Barbieri, H. Weinfurter, and A. Zeilinger, "Entanglement-based quantum communication over 144 km," *Nat. Phys.*, vol. 3, no. 7, pp. 481–486, 2007.

[147] F. Priolo, T. Gregorkiewicz, M. Galli, and T. F. Krauss, "Silicon nanostructures for photonics and photovoltaics.," *Nat. Nanotechnol.*, vol. 9, pp. 19–32, jan 2014.

[148] P. Menna, G. Di Francia, and V. La Ferrara, "Porous silicon in solar cells : A review and a description of its application as an A R coating," *Sol. Energy Mater. Sol. Cells*, vol. 37, no. 1, pp. 13–24, 1995.

[149] F. A. Harraz, "Porous silicon chemical sensors and biosensors: A review," *Sensors Actuators, B Chem.*, vol. 202, pp. 897–912, 2014.

[150] F. P. Mathew and E. C. Alocilja, "Porous silicon-based biosensor for pathogen detection," in *Biosens. Bioelectron.*, vol. 20, pp. 1656–1661, feb 2005.

[151] G. Rong, A. Najmaie, J. E. Sipe, and S. M. Weiss, "Nanoscale porous silicon waveguide for label-free DNA sensing," *Biosens. Bioelectron.*, vol. 23, no. 10, pp. 1572–1576, 2008.

[152] P. Fauchet, "Porous Silicon Optical Label-Free Biosensors," in *Device Appl. Silicon Nanocrystals Nanostructures,*, ch. 10, pp. 293 –322, 2009.

[153] P. A. Snow, E. K. Squire, P. S. J. Russell, and L. T. Canham, "Vapor sensing using the optical properties of porous silicon Bragg mirrors," *J. Appl. Phys.*, vol. 86, no. 4, pp. 1781–1784, 1999.

[154] R. Liu, T. A. Schmedake, Y. Y. Li, M. J. Sailor, and Y. Fainman, "Novel porous silicon vapor sensor based on polarization interferometry," *Sensors Actuators, B Chem.*, vol. 87, pp. 58–62, nov 2002.

[155] H. J. Kim, Y. Y. Kim, K. W. Lee, and S. H. Park, "A distributed Bragg reflector porous silicon layer for optical interferometric sensing of organic vapor," *Sensors Actuators, B Chem.*, vol. 155, pp. 673–678, jul 2011.

[156] S. S. Iyer and Y. H. Xie, "Light emission from silicon," *Science (80-.).*, vol. 260, no. 5104, pp. 40–6, 1993.

[157] A. G. Cullis, L. Canham, and P. D. J. Calcott, "The structural and luminescence properties of porous silicon," *J. Appl. Phys.*, vol. 82, no. 3, pp. 909–965, 1997.

[158] O. Bisi, S. Ossicini, and L. Pavesi, "Porous silicon: A quantum sponge structure for silicon based optoelectronics," *Surf. Sci. Rep.*, vol. 38, pp. 1–126, apr 2000.

[159] C. Delerue, G. Allan, and M. Lannoo, "Theoretical aspects of the luminescence of porous silicon," *Phys. Rev. B*, vol. 48, no. 15, pp. 11024–11036, 1993.

[160] L. Pavesi, C. Mazzoleni, A. Tredicucci, and V. Pellegrini, "Controlled photon emission in porous silicon microcavities," *Appl. Phys. Lett.*, vol. 67, p. 3280, 1995.

[161] P. M. Fauchet, "Monolithic silicon light sources," *Silicon Photonics*, vol. 94, pp. 177–198, 2004.

[162] A. Richter, P. Steiner, F. Kozlowski, and W. Lang, "Current-induced Light-emission From A Porous Silicon Device," *Ieee Electron Device Lett.*, vol. 12, no. 12, pp. 691–692, 1991.

[163] L. Sirleto, V. Raghunatan, A. Rossi, and B. Jalali, "Raman emission in porous silicon at 1.54 microns," *Electron. Lett.*, vol. 40, no. 19, 2004.

[164] Z. Sui, P. P. Leong, and I. P. Herman, "Raman analysis of light-emitting porous silicon," *Appl. Phys. Lett.*, vol. 60, no. 17, pp. 2086–2088, 1992.

[165] R. Tsu, H. Shen, and M. Dutta, "Correlation of Raman and photoluminescence spectra of porous silicon," *Appl. Phys. Lett.*, vol. 60, no. 1, pp. 112–114, 1992.

[166] P. M. Fauchet, L. Tsybeskov, C. Peng, S. P. Duttagupta, J. von Behren, Y. Kostoulas, J. M. V. Vandyshev, and K. D. Hirschman, "Light-Emitting Porous Silicon : Materials Science, properties and Device Applications," *IEEE J. Sel.Top. Quant. Electron.*, vol. 1, no. 4, pp. 1126–1139, 1995.

[167] G. Jia, W. Seifert, T. Arguirov, and M. Kittler, "Infrared light emission from porous silicon," *J Mater Sci Mater Electron*, no. 19, pp. 9–13, 2008.

[168] M. J. Sailor, *Porous Silicon in Practice: Preparation, Characterization and Applications*. Wiley-VCH Verlag GmbH & Co. KGaA, 2012.

[169] B. P. Azeredo, Y.-W. Lin, A. Avagyan, M. Sivaguru, K. Hsu, and P. Ferreira, "Direct Imprinting of Porous Silicon via Metal-Assisted Chemical Etching," *Adv. Funct. Mater.*, 2016.

[170] J. D. Ryckman, M. Liscidini, J. E. Sipe, and S. M. Weiss, "Direct imprinting of porous substrates: A rapid and low-cost approach for patterning porous nanomaterials," *Nano Lett.*, vol. 11, no. 5, pp. 1857–1862, 2011.

[171] T. V. Dolgova, A. I. Maidykovski, M. G. Martemyanov, A. A. Fedyanin, and O. A. Aktsipetrov, "Giant third-harmonic in porous silicon photonic crystals and microcavities," *JETP Lett.*, vol. 75, no. 1, pp. 15–19, 2002.

[172] S. Lettieri and P. Maddalena, "Nonresonant Kerr effect in microporous silicon: Nonbulk dispersive behavior of below band gap X(3)," *J. Appl. Phys.*, vol. 91, no. 9, pp. 5564–5570, 2002.

[173] P. Apiratikul, A. M. Rossi, and T. E. Murphy, "Nonlinearities in porous silicon optical waveguides at 1550 nm.," *Opt. Express*, vol. 17, no. 5, pp. 3396–3406, 2009.

[174] R. L. Smith and S. D. Collins, "Porous silicon formation mechanisms," *J. Appl. Phys.*, vol. 71, no. 8, 1992.

[175] V. Lehmann and U. Gösele, "Porous silicon formation: A quantum wire effect," *Appl. Phys. Lett.*, vol. 58, no. 8, pp. 856–858, 1991.

[176] S. M. Weiss, *Tunable Porous Silicon Photonic Bandgap Structures*. PhD thesis, 2005.

[177] D. Bruggeman, "Berechnung verschiedener physikalischer Konstanten von heterogenen Substanzen.," *Ann. Phys.*, vol. 24, pp. 636–679, 1935.

[178] M. Khardani, M. Bouaïcha, and B. Bessaïs, "Bruggeman effective medium approach for modelling optical properties of porous silicon: comparison with experiment," *Phys. Status Solidi*, vol. 4, no. 6, pp. 1986–1990, 2007.

[179] M. Ferrera, L. Razzari, D. Duchesne, R. Morandotti, Z. Yang, M. Liscidini, J. E. Sipe, S. Chu, B. E. Little, and D. J. Moss, "Low-power continuous-wave nonlinear optics in doped silica glass integrated waveguide structures," *Nat. Photonics*, vol. 2, no. 12, pp. 737–740, 2008.

[180] D.-I. Yeom, E. C. Mägi, M. R. E. Lamont, M. A. F. Roelens, L. Fu, and B. J. Eggleton, "Low-threshold supercontinuum generation in highly nonlinear chalcogenide nanowires.," *Opt. Lett.*, vol. 33, no. 7, pp. 660–662, 2008.

[181] I. D. Rukhlenko, M. Premaratne, and G. P. Agrawal, "Effective mode area and its optimization in silicon-nanocrystal waveguides," *Opt. Lett.*, vol. 37, no. 12, p. 2295, 2012.

[182] T. Baehr-Jones, R. Ding, A. Ayazi, T. Pinguet, M. Streshinsky, N. Harris, J. Li, L. He, M. Gould, Y. Zhang, A. E.-J. Lim, T.-Y. Liow, S. H.-G. Teo, G.-Q. Lo, and M. Hochberg, "A 25 Gb/s Silicon Photonics Platform," *Opt. Express*, vol. 21, no. 3, pp. 3693–3704, 2012.

[183] C. Galland, A. Novack, Y. Liu, R. Ding, M. Gould, T. Baehr-Jones, Q. Li, Y. Yang, Y. Ma, Y. Zhang, K. Padmaraju, K. Bergmen, A. E.-J. Lim, G.-Q. Lo, and M. Hochberg, "A CMOS-compatible silicon photonic platform for high-speed integrated opto-electronics," *Integr. photonics Mater. devices Appl. II*, vol. 8767, p. 87670G, may 2013.

[184] L. He, Y. Liu, C. Galland, A. E.-J. Lim, G.-Q. Lo, T. Baehr-Jones, and M. Hochberg, "A High-Efficiency Nonuniform Grating Coupler Realized With 248-nm Optical Lithography," *IEEE Photonics Technol. Lett.*, vol. 25, pp. 1358–1361, jul 2013.

[185] Y. Liu, R. Ding, M. Gould, T. Baehr-Jones, Y. Yang, Y. Ma, Y. Zhang, A. E. J. Lim, T. Y. Liow, S. H. G. Teo, G. Q. Lo, and M. Hochberg, "30GHz silicon platform for photonics system," *2013 Opt. Interconnects Conf. OI 2013*, vol. 1, pp. 27–28, 2013.

[186] L. Pavesi and P. Dubos, "Random porous silicon multilayers: application to distributed Bragg reflectors and interferential Fabry - Pérot filters," *Semicond. Sci. Technol.*, vol. 12, no. 5, pp. 570–575, 1997.

[187] Q. Xu and M. Lipson, "Carrier-induced optical bistability in silicon ring resonators.," *Opt. Lett.*, vol. 31, no. 3, pp. 341–343, 2006.

[188] Y. Zhang, S. Yang, A. E.-J. Lim, G.-Q. Lo, C. Galland, T. Baehr-Jones, and M. Hochberg, "A compact and low loss Y-junction for submicron silicon waveguide.," *Opt. Express*, vol. 21, no. 1, pp. 1310–6, 2013.

[189] N. C. Harris, Y. Ma, J. Mower, T. Baehr-Jones, D. Englund, M. Hochberg, and C. Galland, "Efficient , compact and low loss thermo-optic phase shifter in silicon," *Opt. Express*, vol. 22, no. 9, pp. 83–85, 2014.

[190] C. A. Husko, A. S. Clark, M. J. Collins, A. De Rossi, S. Combrié, G. Lehoucq, I. H. Rey, T. F. Krauss, C. Xiong, and B. J. Eggleton, "Multi-photon absorption limits to heralded single photon sources.," *Sci. Rep.*, vol. 3, p. 3087, 2013.

[191] D. Grassani, S. Azzini, M. Liscidini, M. Galli, M. J. Strain, M. Sorel, J. E. Sipe, and D. Bajoni, "A micrometer-scale integrated silicon source of time-energy entangled photons," vol. 041047, p. 13, sep 2014.

[192] Z. Zhang, J. Mower, D. Englund, F. N. C. Wong, and J. H. Shapiro, "Unconditional security of time-energy entanglement quantum key distribution using dual-basis interferometry," *Phys. Rev. Lett.*, vol. 112, no. 12, pp. 1–5, 2013.

[193] A. P. Lund, A. Laing, S. Rahimi-Keshari, T. Rudolph, J. L. O'Brien, and T. C. Ralph, "Boson sampling from a Gaussian state," *Phys. Rev. Lett.*, vol. 113, no. 10, pp. 1–5, 2014.

[194] N. Matsuda, P. Karkus, H. Nishi, T. Tsuchizawa, W. J. Munro, H. Takesue, and K. Yamada, "On-chip generation and demultiplexing of quantum correlated photons using silicon-silica monolithic waveguide platform," *Opt. Express*, vol. 22, no. 19, pp. 22831–22840, 2014.

[195] M. Minkov and V. Savona, "A compact, integrated silicon device for the generation of spectrally-filtered, pair-correlated photons," *arXiv:1602.00870*, vol. 18, no. 5, p. 0, 2016.

[196] A. Eckstein, G. Boucher, A. Lemaître, P. Filloux, I. Favero, G. Leo, J. E. Sipe, M. Liscidini, and S. Ducci, "High-resolution spectral characterization of two photon states via classical measurements," *Laser Photon. Rev.*, vol. 8, pp. L76–L80, sep 2014.

[197] M. Liscidini and J. E. Sipe, "Stimulated Emission Tomography," *Phys. Rev. Lett.*, vol. 111, p. 193602, nov 2013.

[198] B. Fang, O. Cohen, M. Liscidini, J. E. Sipe, and V. O. Lorenz, "Fast and highly resolved capture of the joint spectral density of photon pairs," *Optica*, vol. 1, no. 5, p. 281, 2014.

[199] L. A. Rozema, C. Wang, D. H. Mahler, A. Hayat, A. M. Steinberg, J. E. Sipe, and M. Liscidini, "Characterizing an entangled-photon source with classical detectors and measurements," *Optica*, vol. 2, no. 5, pp. 430–433, 2015.

[200] L. Mandel and E. Wolf, *Optical Coherence and Quantum Optics*. Cambridge University Press, 1995.

[201] K. Garay-Palmett, H. J. McGuinness, O. Cohen, J. S. Lundeen, R. Rangel-Rojo, A. B. U'Ren, M. G. Raymer, C. J. McKinstrie, S. Radic, and I. A. Walmsley, "Photon pair-state preparation with tailored spectral properties by spontaneous four-wave mixing in photonic-crystal fiber," *Opt. Express*, vol. 15, no. 22, pp. 14870–14886, 2007.

[202] B. Smith, P. Mahou, O. Cohen, J. S. Lundeen, and I. Walmsley, "Photon pair generation in birefringent optical fibers," *Opt. Express*, vol. 17, no. 26, p. 23589, 2009.

[203] M. Avenhaus, A. Eckstein, P. J. Mosley, and C. Silberhorn, "Fiber-assisted single-photon spectrograph.," *Opt. Lett.*, vol. 34, pp. 2873–5, sep 2009.

[204] A. Peres, *Quantum Theory: Concepts and Methods*. Kluwer Academic, Boston, 1995.

[205] C. K. Law and J. H. Eberly, "Analysis and Interpretation of High Transverse Entanglement in Optical Parametric Down Conversion," *Phys. Rev. Lett.*, vol. 92, no. 12, p. 127903, 2004.

[206] A. A. Freschi and J. Frejlich, "Adjustable phase control in stabilized interferometry," *Opt. Lett.*, vol. 20, no. 6, pp. 635–637, 1995.

[207] G. Harder, V. Ansari, B. Brecht, T. Dirmeier, C. Marquardt, and C. Silberhorn, "An optimized photon pair source for quantum circuits," *Opt. Express*, vol. 21, no. 12, pp. 13975–13985, 2013.

[208] J. Mower, Z. Zhang, P. Desjardins, C. Lee, J. H. Shapiro, and D. Englund, "High-dimensional quantum key distribution using dispersive optics," *Phys. Rev. A - At. Mol. Opt. Phys.*, vol. 87, no. 6, pp. 1–8, 2013.

List of publications

Articles

- **Simbula A.**, Rodriguez G.A, Menotti M., De Pace S., Weiss S.M., Galli M., Liscidini M. and Bajoni D., Low-power four-wave mixing in porous silicon microring resonators. *Appl. Phys. Lett*, 109:021106, 2016.

- Grassani D., **Simbula A.**, Pirotta S., Galli M., Menotti M., Harris N.C., Baehr-Jones T., Hochber M., Galland, C., Liscidini M. and Bajoni D., Energy correlations of photon pairs generated by a silicon microring resonator probed by Stimulated Four Wave Mixing. *Scientific Reports* 6:62564, 2016.

- Harris N.C., Grassani D., **Simbula A.**, Pant M., Galli M., Baehr-Jones T., Hochberg M., Englund D., Bajoni B. and Galland C., Integrated source of spectrally filtered correlated photons for large-scale quantum photonic systems. *Physical Review X*,4(4):041047, 2014.

Contributions to conference proceedings

- **Simbula A.**, Rodriguez G., Menotti M., Galli M., Bajoni D., Weiss S., and Liscidini M., Four-Wave Mixing in Porous Silicon Microring Resonators. *CLEO: Science and Innovations, CLEO-SI 2016*, SW4E-7, 2016.

- Grassani D., **Simbula A.**, Galli M., Pirotta S., Baehr-Jones T., Hochberg M., Harris N.C., Galland C., Sipe J.E., Bajoni D. and Liscidini M., Measurement of energy correlations of photon pairs generated in silicon ring resonators, *CLEO Europe - Technical Digest, CLEO-AT 2015*, 7183629, 2015.

- Grassani D., **Simbula A.** , Galli M., Pirotta S., Baehr-Jones T., Hochberg M., Harris N.C., Galland C., Sipe J.E., Bajoni D. and Liscidini M., "Measurement of energy correlations of photon pairs generated in silicon ring

resonators", *CLEO: Science and Innovations, CLEO-SI 2015* pp. 2267, 2015.

- Grassani D., **Simbula A.**, Galli M., Pirotta S., Baehr-Jones T., Hochberg M., Harris N.C., Galland C., Sipe J.E., Bajoni D. and Liscidini M., Measurement of energy correlations of photon pairs generated in silicon ring resonators. *CLEO: QELS - Fundamental Science, CLEO-QELS 2015*, pp. 1551, 2015.

- Grassani D., **Simbula A.**, Galli M., Pirotta S., Baher-Jones T., Hochberg M., Harris N.C., Galland C., Sipe J.E., Bajoni D. and Liscidini, M., Measurement of energy correlations of photon pairs generated in silicon ring resonators. *CLEO: Applications and Technology, CLEO-AT 2015*, JW2A.4, 2015.

- Liscidini M., Grassani D., **Simbula A.**, Galli M., Pirotta S., Baehr-Jones T., Hochberg M., Harris N.C., Galland C., Sipe J.E. and Bajoni D., High-resolution measurement of energy correlations of photon pairs generated in silicon ring resonators *ICTON conference paper* 719363, 2015.

Acknowledgements

During the PhD I have been helped and supported by so many people that is hard to include all of them in few pages of acknowledgements, but I do my best.

First of all, I wish to thank my supervisors, Prof. Matteo Galli, which has always be a great inspiration to me, for all his fantasy, suggestions, patience and kindness, and Prof. Daniele Bajoni for always having new ideas, for his availability and dedication to our work. Another special thanks is due to Dr. Davide Grassani: we spent long time working together in the lab to achieve the hardest but also more satisfying results. I also wish to thank other professors in my research group: Prof. Lucio Claudio Andreani, Prof. Dario Gerace, and Dr. Marco Liscidini, that needs a special acknowledgement for always being stimulating and helpful, and in particular for giving me the possibility to spend a period as a visiting student at Vanderbilt University. I take the chance to thank also Prof. Sharon Weiss and all the people in her research group in Nashville, in particular Gilbert, Jeremy and Kevin.

I wish to sincerely thank Dr. Mher Ghulinyan from FBK in Trento and Dr. Giuseppe Vallone from University of Padova for carefully reading the manuscript and for giving me useful advices that helped me to improve it.

I shared the last three years with other PhD students that shared the lab with me: Step, Giulia, Rita, Stefanino, Totó, because we will never forget that *l'ottimo é nemico del buono*. Thanks also to the more theoretical PhDs, Filippo, Matteo, Daniele, and all the people in the group: Saeid, Francesco, Lucia, Piotr, Lee, Angelo, and also the former thesis students, in particular Cesare, Alberto and Luca. I wish they remember, as well as me, the moments spent together, from aligning U-benches, to playing with Geoguesser during coffee-breaks, from counting photons, to unexpectedly meeting at parties, from helping each other in the lab, to pulling vans out of the ponds in Switzerland. This experience was unique also because all of you.

There are also some colleagues and friends that I wish to thank, in particular Mario, Seta, Barbara, Ian and Linda for all the epic moments spent

together surrounded by mysterious posters and blackboards.

Even if I found my second home in the University, my third home is the rugby field: the first to thank is Agnese, of course, together with Divá, Zainet, Ceci, Bart, Cri, Eli, Ele, Giuli, Lisa, Mix ... I can't mention all of them, so I thank my teams, Fenici and Rocce, for making these years unforgettable.

A special thanks goes to Samuel, for always being so careful and close to me, hoping that we can build our future together.

I dedicate this Thesis to all of my teachers, meaning all the people that during my life helped me to learn and to grow up: not only professors, but also family and friends. I want thus to thank all my family, for always believing in me, and in particular my sister Franci, for I believe in her. My final thanks go to my very first teachers, my parents, that are always my greatest inspiration and motivation.